University of Alberta

A relative frames model for fluid flow in microgravity

by

Martin Mervin Stanley Metro Lastiwka

A thesis submitted to the Faculty of Graduate Studies and Research in partial fulfillment of the requirements for the degree of Master of Science.

Department of Mechanical Engineering

Edmonton, Alberta
Spring 2003

National Library of Canada
Acquisitions and Bibliographic Services
395 Wellington Street
Ottawa ON K1A 0N4
Canada

Bibliothèque nationale du Canada
Acquisitions et services bibliographiques
395, rue Wellington
Ottawa ON K1A 0N4
Canada

Your file Votre référence

Our file Notre référence

The author has granted a non-exclusive licence allowing the National Library of Canada to reproduce, loan, distribute or sell copies of this thesis in microform, paper or electronic formats.

L'auteur a accordé une licence non exclusive permettant à la Bibliothèque nationale du Canada de reproduire, prêter, distribuer ou vendre des copies de cette thèse sous la forme de microfiche/film, de reproduction sur papier ou sur format électronique.

The author retains ownership of the copyright in this thesis. Neither the thesis nor substantial extracts from it may be printed or otherwise reproduced without the author's permission.

L'auteur conserve la propriété du droit d'auteur qui protège cette thèse. Ni la thèse ni des extraits substantiels de celle-ci ne doivent être imprimés ou autrement reproduits sans son autorisation.

0-612-82299-0

Canada

University of Alberta

Library Release Form

Name of Author: Martin Mervin Stanley Metro Lastiwka

Title of Thesis: A relative frames model for fluid flow in microgravity

Degree: Master of Science

Year this Degree Granted: 2003

Permission is hereby granted to the University of Alberta to reproduce single copies of this thesis and to lend or sell such copies for private, scholarly, or scientific research purposes only.

The author reserves all other publication and other rights in association with the copyright in the thesis, and except as hereinbefore provided, neither the thesis nor any substantial portion thereof may be printed or otherwise reproduced in any material form whatever without the author's prior written permission.

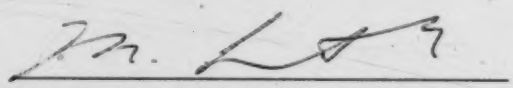

Martin Mervin Stanley Metro Lastiwka
70 Glamorgan Drive
Sherwood Park, Alberta
Canada, T8A 2Y6

Jan 2, 2003

University of Alberta

Faculty of Graduate Studies and Research

The undersigned certify that they have read, and recommend to the Faculty of Graduate Studies and Research for acceptance, a thesis entitled A relative frames model for fluid flow in microgravity submitted by Martin Mervin Stanley Metro Lastiwka in partial fulfillment of the requirements for the degree of Master of Science.

Dr. J.W. Yokota (Supervisor)

Dr. Y.S. Wong

Dr. C.R. Koch

Date 12/22/2002

ABSTRACT

Many experiments in fluid science make use of the microgravity environment found on orbiting spacecraft. To predict the microgravity flow, the acceleration environment is often modeled for numerical analysis using time varying functions of applied acceleration fields. It has been found that these models do not predict all aspects of the flow observed in experiments.

This work proposes a system to describe the microgravity environment that uses a relative frames analysis and a model of spacecraft motion. The relative frames analysis predicts conservative as well as non-conservative sources of fluid motion. The model of spacecraft motion is based on parameters used to describe a sinusoidally varying acceleration field, but it yields values for the rotational terms predicted by the relative frames analysis. Further, this system is shown to reproduce the identical terms of the sinusoidal microgravity field model.

The relative frames analysis combined with the spacecraft motion

model predicts non-conservative source terms that create motion even in a fluid of uniform density. This type of motion cannot be reproduced by any function of a time varying field. The proposed model of the microgravity environment can be used as a design tool to define experimental parameters that minimize the deleterious effects of microgravity accelerations on an orbiting fluids experiment.

Acknowledgements

I thank my wife Kelcey and my parents for their support as I made my way through this endeavor.

I also thank my lab partners Mike Wojcichowsky and Chris Sideroff. Their help and camaraderie have made this degree a first class experience.

Finally, I express my appreciation to Jeff Yokota for his guidance and friendship. Through his teaching, I have gained the ability and confidence to approach any problem.

To my family and friends, especially my newborn son McKinley.

CONTENTS

1 Fluid Science in Microgravity **1**
- 1.1 Microgravity models for fluid motion analysis . . . 3
- 1.2 Proposed system of microgravity characterization . . . 8

2 Theoretical Model **11**
- 2.1 Relative coordinate frames . . . 13
- 2.2 Equations of Motion . . . 18
- 2.3 Modified Equations of Motion . . . 19
  - 2.3.1 Breakdown to sum of partial derivatives . . . 24
  - 2.3.2 Rotation tensor components . . . 28
  - 2.3.3 Reduction of terms . . . 31
  - 2.3.4 Summary of relative frames analysis . . . 32
- 2.4 Fluid flow assumptions . . . 33
  - 2.4.1 Incompressible flow . . . 33
  - 2.4.2 Inviscid approximation . . . 34
- 2.5 Model parameters . . . 34
  - 2.5.1 Spacecraft motion model . . . 35
  - 2.5.2 Magnitudes of resulting source terms . . . 42
  - 2.5.3 Summary of model characteristics . . . 43
- 2.6 Simplification to known models . . . 46
  - 2.6.1 Sinusoidal g-jitter . . . 46
  - 2.6.2 One relative frame . . . 47

3 Numerical Method **48**
- 3.1 The Modified Clebsch/Weber Transformation . . . 48
  - 3.1.1 Set-up . . . 49
  - 3.1.2 Transformation . . . 51
- 3.2 Solution outline . . . 52

3.3 Directional components and equations to be solved 53
3.4 Dimensional analysis 58
3.5 Hyperbolic equations 60
3.6 Elliptic equation 62
3.6.1 Stability analysis 66
3.7 Transformation to generalized coordinates 67
3.8 Grids and timestep sizes 70
3.9 Differencing techniques 74
3.10 Initial conditions 77
3.11 Boundary conditions 78
3.11.1 Rectangular domain 79
3.11.2 Circular domain 80
3.12 Code validation 82

4 Results from Numerical Analysis **85**
4.1 Results from flows with a density gradient 86
4.1.1 Sinusoidal g-jitter 89
4.1.2 Complete relative frames model 96
4.2 Results from uniform density flows 105
4.2.1 Sinusoidal g-jitter 107
4.2.2 Complete relative frames model 110
4.2.3 Uniform density flows in a circular cavity 115
4.3 Summary 120

5 Conclusions **132**

A Rotation Tensor Properties **136**

B Tensor to Vector Transformation **139**

C Simplification of terms **141**

List of Tables

2.1 Orders of magnitude of the source terms 43

3.1 Effect of timestep size 75
3.2 Maximum velocity comparison 84

List of Figures

2.1 Moving Coordinates 'z_i' and 'y_i' and Fixed Coordinates 'Z_i' 14
2.2 Summary of spacecraft motion model 41

3.1 Growth factor for LU scheme 68
3.2 Rectangual grid with uniform cell sizes 71
3.3 Rectangual grid with uniform cell sizes 72
3.4 Circular grid 73
3.5 Unwrapping of circular domain to form the computational domain 74
3.6 Square grid used for code validation 83

4.1 Rectangular mesh with uniform cell sizes 88
4.2 Material variable X, initial condition 89
4.3 Material variable Y, initial condition 90
4.4 Density interface, initial condition 91
4.5 Enstrophy with sinusoidal g-jitter only 92
4.6 Kinetic Energy with sinusoidal g-jitter only 93
4.7 Density interface with sinusoidal g-jitter at 4 1/4 cycle . . . 94
4.8 X material coordinate with sinusoidal g-jitter at 4 1/4 cycle 95
4.9 Y material coordinate with sinusoidal g-jitter at 4 1/4 cycle 96
4.10 Fluid speed with sinusoidal g-jitter at 4 1/4 cycle 97
4.11 Fluid speed with sinusoidal g-jitter at 4 3/4 cycle 98
4.12 Velocity with sinusoidal g-jitter, 4 1/4 cycles (max velocity is 19.7 $\mu m/s$) 99
4.13 Velocity with sinusoidal g-jitter, 4 3/4 cycles (max velocity is 19.7 $\mu m/s$) 100
4.14 Vorticity with sinusoidal g-jitter at 4 1/4 cycle 100
4.15 Enstrophy with complete relative reference frame model . . 101
4.16 Kinetic Energy with complete relative reference frame model 102

4.17 Density interface with complete relative reference frame model at 4 1/4 cycle 103
4.18 X material coordinate with complete relative reference frame model at 4 1/4 cycle 104
4.19 Y material coordinate with complete relative reference frame model at 1/4 cycle 105
4.20 Y material coordinate with complete relative reference frame model at 1 1/4 cycle 106
4.21 Y material coordinate with complete relative reference frame model at 2 1/4 cycle 107
4.22 Y material coordinate with complete relative reference frame model at 3 1/4 cycle 108
4.23 Y material coordinate with complete relative reference frame model at 4 1/4 cycle 109
4.24 Fluid speed with complete relative reference frame model, 4 1/4 cycle (contours at 200, maximum value $O(10^3)$) . . . 110
4.25 Velocity with relative frames model, 4 1/4 cycles (max velocity is 949 $\mu m/s$) 111
4.26 Vorticity with complete relative reference frame model at 4 1/4 cycle (contours at 5000, maximum value $O(10^4)$) 112
4.27 Enstrophy with sinusoidal g-jitter model in a fluid of uniform density 113
4.28 Kinetic energy with sinusoidal g-jitter model in a fluid of uniform density 114
4.29 X material coordinate with sinusoidal g-jitter model in a fluid of uniform density 115
4.30 Y material coordinate with sinusoidal g-jitter model in a fluid of uniform density 116
4.31 Enstrophy with relative frames model in a fluid of uniform density 117
4.32 Kinetic Energy with relative frames model in a fluid of uniform density 118
4.33 X material coordinate with relative frames model in a fluid of uniform density 119
4.34 Y material coordinate with relative frames model in a fluid of uniform density 120
4.35 Fluid speed with relative frames model in a fluid of uniform density 121

4.36 Velocity with relative frames model in a fluid of uniform density (max velocity is 0.023 $\mu m/s$) 122
4.37 Circular grid 123
4.38 X material coordinates at initial condition 124
4.39 Y material coordinates at initial condition 125
4.40 Enstrophy time history 126
4.41 Kinetic energy time history 127
4.42 X material coordinates at 4 1/2 cycles 128
4.43 Y material coordinates at 4 1/2 cycles 129
4.44 Fluid speed at 4 1/2 cycles 130
4.45 Velocity vectors at 4 1/2 cycles (maximum value is 0.0128 $\mu m/s$) 131

NOMENCLATURE

LATIN SYMBOLS

A_{ij}	Rotation tensor for earth-centered coordinates
A_i	Rotational source term component in velocity decomposition
a_{ij}	Rotation tensor for experiment-centered coordinates
c_i	Position vector in eulerian coordinates
c_i'	Constant part of position vector in eulerian coordinates
Z_i	Inertial eulerian coordinates
z_i	1st non-inertial frame in eulerian coordinates
y_i	2nd non-inertial frame in eulerian coordinates
x_i	3rd non-inertial frame in eulerian coordinates
X_i	3rd non-inertial frame Lagrangian coordinates
x, y	Non-inertial cartensian coordinates for fluid experiment
X, Y	Non-inertial Lagrangian coordinates for fluid experiment
V_i	Inertial velocity

u_i ..... Non-inertial velocity

u, v ..... Non-inertial cartensian velocity components

g_0 ..... Gravitational acceleration at the surface of the earth

G ..... Gravitational constant

M_E ..... Mass of the earth

t ..... Time

GREEK SYMBOLS

α_{ij} ..... Rotation tensor for 2nd non-inertial frame

β ..... Bernoulli potential representing source terms

Δt ..... Time step

δ ..... Difference operator; δ^+ forward, δ^- backward, δ central

δ_{ij} ..... Kronecker delta

ϵ_{ijk} ..... Permutation tensor

θ ..... Angle descibing spacecraft pitch

λ_i ..... Fixed distance from spacecraft centroid to experimental frame's origin

μ ..... Micro prefix (10^{-6})

ρ ..... Density

τ ..... Viscous stress tensor

ϕ ..... Bernoulli potential

ψ ..... Stream function

Ω ..... Rotation rate tensor

Ω' ..... Rotation rate tensor

ω ..... Rotation rate tensor

(ξ, η) ..... Computational coordinates

v ..... An arbitrary volume

CHAPTER 1

Fluid Science in Microgravity

With the development of the International Space Station, there is an increased opportunity to take advantage of the microgravity environment for scientific research. In such an environment, experimentalists can investigate and isolate a variety of processes that would otherwise be obscured by the effects of the large gravity force incurred by earthbound research. This opens the door to a number of excellent opportunities for investigation and new knowledge.

The advantages of science in space are, of course, tempered by some complexities. On board any orbiting platform, the effects of gravity are greatly reduced but not eliminated altogether. For example, when a spacecraft orbits the earth, the earth's gravitational acceleration is balanced by the orbital motion at its center of mass [4], but there is an imbalance at locations away from the center of mass, resulting in small accelerations. Other sources of accelerations occur with thruster firings and spacecraft maneuvering [11], atmospheric drag [1], machinery vibrations and crew motions [3].

There are a number of areas of study where effects of microgravity flow must be considered. These include sloshing dynamics [13], two-phase flow for heat management and waste movement [8], and studies on diffusion coefficient measurements [36]. In the life sciences area, it has been discovered that bacteria show increased growth in orbiting cultures. This phenomenon is well documented by Kacena et al. [14] and Thevenet et al.[30], although when mechanisms are proposed, the fluid motion due to microgravity is rarely considered, as in the investigation by Klaus et al. [17]. At any rate, the possibilities of discovery offered by the unique environment are endless and stand to contribute significantly to the furthering of the knowledge base in many areas of study.

One of the main practical purposes expected of the microgravity environment is its use in materials processing. Larger, more pure crystals can be grown in the reduced gravity environment[24]. Such crystal growth has applications in such areas as semi-conductors and organic proteins [31]. With this practical purpose in mind, a number of investigators have studied the effects of the microgravity environment when considering the building of these crystals. These effects include considering microaccelerations on a fluid with a thermal gradient [38], liquid bridge stability [20] and interfacial dynamics of different liquids[6].

In general, these microgravity fluid flow investigations use numerical simulations to better understand the effects of microgravity. With a better

understanding of the flow, it is hoped that the detrimental effects on the experiments and processes can be reduced or eliminated. Quite often, such effects are reduced through the use of vibration isolation systems, such as those explained by Hampton and Whorton[9], and Tryggvason et al.[33].

Another means of reducing the effects of the microgravity environment on fluid experiments is offered by Savino and Monti[26]. By considering the orientation of the experiment with respect to background as well as transient acceleration directions, it is suggested that fluid convection can be significantly reduced.

1.1 Microgravity models for fluid motion analysis

To be able to predict the effects of microgravity on space-based experiments, a number of models have been proposed. These models can usually be put into one of four categories. The first is the most simple, which uses a constant acceleration field in one direction acting on the fluid. This is useful for determining the sensitivity of the experiment to constant background accelerations such as atmospheric drag or steady spacecraft rotation. These accelerations can be quite significant, as suggested by Kassemi and Ostrach[16]. It is suggested that the lowest residual acceleration levels currently achievable in orbiting platforms are of the order of $10^{-4}g_0$ to $10^{-3}g_0$, where g_0 is the acceleration due to gravity at the surface of the earth. In their investigation, a rectangular enclosure with rigid boundaries is used to represent a standard configuration for basic research purposes.

The second category of microgravity model makes use of a unidirectional acceleration that varies periodically with time. Diffusion coefficients are studied numerically by Matsumoto and Yoda [36], who found that coefficient measurements became riddled with error when the frequency of the periodic oscillations fell below 0.1Hz. Thermally-induced convection is studied by Kondos and Subramanian [19]. A square cavity is heated differentially at opposite walls, and a sinusoidally varying acceleration field is applied to simulate the source of convection. A third investigation given by Duval and Jacqmin [6] describes another cavity flow problem with a sinusoidally varying acceleration field. In this problem, the acceleration is aligned normal to the density gradient and is shown to eventually lead to the breakdown of the density interface.

The work of Naumann[23] describes the case when the first and second categories of microgravity models are used in concert, thus accounting for residual as well as transient sources of acceleration. Another variation on these models is given by Schneider and Straub[27], who apply the constant acceleration as a step pulse and then repeat the trial with the application of a sinusoidally varying body force for one period of oscillation.

The third category of microgravity models uses a stochastic method to describe the acceleration field on board spacecraft. A similar analysis to the work of Kondos is done here by Thomson et al[31]. Once again, a two-dimensional cavity is heated differentially and the convection induced by the

acceleration field is studied. In this case, however, instead of a sinusoidal acceleration, a sequence of random acceleration field values is used. A narrow band noise model is used to replicate the spectrum of measured values for the microgravity environment. Some of the specific differences in the flow characteristics resulting from the second and third category models are compared directly by Drolet and Vinals[5].

The stochastic approach to describing microgravity is a much more realistic model in terms of reproducing acceleration levels and frequencies, but the sources of motion share a similarity to the previous two category of microgravity models. Any acceleration field that is used to model fluid motion produces a conservative source if the applied term is purely time dependent; with no spatial dependencies, there is no vortex generation.

The last category of microgravity model involves the use of non-inertial frames of reference to describe the equations of fluid motion. In these models, non-conservative sources of motion arise by way of Coriolis and angular accelerations. There are only a handful of researchers that employ such an approach to describe the microgravity environment. Moving reference frames are used by Alexander and Lundquist[1], who model the relative motion of a particle moving through a fluid in an orbiting spacecraft. An inertial frame is assumed to be fixed to the center of the earth, while a non-inertial frame moves with the spacecraft, and the experiment is said to be fixed to the rigid spacecraft. The sources of motion considered are atmospheric drag, the gravity gradient, and the spacecraft attitude. To obtain values for this last term,

the orientation of the spacecraft's frame of reference is said to match the trajectory of its motion. In this way, the angular velocity of the spacecraft is related to the orbital period.

There are other topics that have been considered with a relative frames analysis to model microgravity. Rotational motion described with a moving frame is used by Hung and Pan and also by Hung et al. to study sloshing dynamics for a partially filled dewar tank[13] [12]. Zebib and Le Cunff study the effects of Coriolis forces on liquid bridge instabilities [39] [20]. In a more standard problem, Yuferev et al. make the point that rotational terms produced by moving reference frames can be very significant in predicting thermal convection flows in a microgravity [38]. Their numerical studies make use of the familiar rectangular cavity with differentially heated walls.

A very complete model of the microgravity environment is offered by Fichtl and Holland [7]. They present a relative frames model of motion and use a stochastic analysis to predict values for the source terms. Once again, two categories are represented in a single model in an effort to obtain a more realistic depiction of the microgravity environment.

One of the investigators involved in microgravity sciences, Bjarni Tryggvason, noticed that the microgravity models used in numerical studies failed to capture aspects of fluid motion that he observed through experimentation [32]. The models being used in this case involved a time-varying acceleration fields. From his experience as an astronaut running experiments on both

land-based and orbiting platforms, he believed that there was a key characteristic of the microgravity environment that was not being captured by acceleration field models of microgravity.

In support of Tryggvason's observations, there is another indication that the microgravity fluids are experiencing some unexpected phenomenon. This is given by bacterial growth experiments. In a number of experiments, including the works of Klaus et al.[17], Kacena et al.[14], and Thevenet et al.[30], it was found that bacteria actually grow to higher concentrations in microgravity when compared to equivalent earth-based experiments. Both Klaus and Kacena propose that the mechanism for this accelerated bacterial growth lies in the fact that the orbiting bacterial cultures do not settle to the bottom of the container, thereby avoiding over-crowding. Without being over-crowded, the bacterium is not starved of nutrients or choked by the waste of other nearby bacteria. A question left for debate remains: if the space-based bacteria do not settle through the growth medium, why is it that they do not starve themselves out of nutrients or choke on their own waste? Klaus proposes that the diffusion rates alone are adequate to transport nutrients and waste at a rate sufficient to maintain a growth advantage over settling bacteria.

The explanation given by Klaus for the mechanism behind the increased growth does not take into account the possibility of microaccelerations causing fluid flow in space-based experiments. However, models based on potential body forces predict that no flow results in a fluid medium of uniform

density. Again, there is the suggestion that current fluid models are not adequate to describe some important aspects of fluid flow in microgravity.

1.2 Proposed system of microgravity characterization

In the following chapter, a representation of the microgravity environment is proposed that employs a relative frames analysis and a model of spacecraft motion. This work is performed in response to the deficiencies in current microgravity models described by Tryggvason, with specific attention paid to uniform density flows [32]. It is anticipated that the unique characteristics of fluid flow described by non-inertial frames might also be able to offer another mechanism for increased bacterial growth in microgravity.

The equations of conservation of mass and momentum are derived from 1^{st} principles using multiple frames of reference. The frames describe the motion of a space-based experimental platform, and the resulting equations of motion yield non-conservative source terms that are especially relevant to uniform density flows.

The relative frames derivation results in potential *and* non-potential sources of motion. The model thus predicts flow in even a fluid of uniform density. This and other characteristics of the flow produced by the model are investigated in chapter 4.

As explained in section 1.1, the use of non-inertial frames of reference to

describe microgravity flow is not entirely new. A few investigators, such as Yuferev et al., Alexander and Lundquist, Kamotani et al., consider relative frames of reference as necessary in describing phenomena affecting fluid flow in microgravity. It is explained that, although often overlooked, spacecraft rotation creates important sources of fluid motion in the microgravity environment [38].

In order to quantify the motion of the frames, a model of spacecraft motion is also proposed. This model, described in section 2.5.1, uses the standard sinusoidally varying body forces to describe the translation, then extrapolates rotations based on these translations. In this way, a complete microgravity model is obtained with the simpler models contained therein.

The source terms generated by the relative frames analysis and model of spacecraft motion will be investigated numerically. The differences between this model and a unidirectional sinusoidal acceleration model will be highlighted, and the unique characteristics of the non-conservative source terms will be investigated.

The proposed microgravity model presents a strong possibility in terms of solving the inadequacies of current microgravity models. The flexibility of the model also makes it useful as a tool to aid in the design of microgravity experiments. The multiple frames of reference allow for a number of sources of motion to be considered, and the spacecraft motion model allows acceptable values for the sources to be easily determined. Various parame-

ters can then be investigated in order to determine what configuration would best minimize the deleterious effects of the microgravity environment on a particular experiment.

Chapter 2

Theoretical Model

It is proposed that when describing microgravity flow, the use of a body force function does not adequately describe all aspects of the sources of motion as found in experiments. This leaves a somewhat vague problem for a theoretical modeler to address. Since the motion being studied is given in terms of μ-metres, and subtle phenomena such as Brownian motion is even considered, any model must be extremely sensitive to even the most obscure sources of motion. Could the boundaries of the container be flexing and somehow be causing motion in the fluid? Is the continuum model accurate for this kind of study? Is there simply a flaw in the experiments? These are all doubts that further confound the problem.

In order to approach such a complex and undefined problem, a simple and ordered ideology is employed. A model is derived from the first principles of motion and fluid mechanics, all the while being highly sensitive to any and every assumption. The first and most defining assumption is that the motion of the fluid experiment is limited to regular mathematical functions. Beyond

this, however, no aspect of the resulting model is neglected. With this strict approach, a simple model results in complex equations with abstruse implications.

To describe the microgravity environment, a relative reference frames analysis is employed. All sources of accelerations are then only due to the earth's gravity and the motion of the space-based platform for the experiment. The motion is defined by considering a circular orbit with sinuisoidal fluctuations in altitude. These fluctutions correspond to microgravity models that use a sinoidally varying body force. The model turns a new corner, however, when the pitch of the orbiting platform is made to follow its path, resulting in rotational motion. Once the model is defined, no new assumptions are made – all sources are kept and standard values for the sinusoidal fluctuations are used, resulting in appropriate values for rotational terms.

The development of the model will begin with the derivation of displacement, velocity, and acceleration in non-inertial frames of reference that are useful to describe spacecraft motion. This is followed by the implementation of these reference frames in the equations of motion for fluids. The model describing the motion of the space-based experimental platform is then precisely defined. The result is a model for fluid motion in microgravity that captures the non-conservative motion in a micrograviyt environment. These motions, which can be related to the shape of the experiment's boundaries, are believed to be necessary whenever a complete model of all of the subtle motions of a fluid in microgravity is desired.

2.1 Relative coordinate frames

To begin the relative frames analysis, the multiple coordinate systems are defined relative to each other. These frames describe the position of the fluid within an orbiting experiment. The velocity and acceleration of the fluid can then be determined by taking the total time derivative of position.

A fixed coordinate frame, a rotating frame, and a rotating and translating frame are shown in two dimensions in figure 2.1. This diagram can be related to an actual physical situation by the following definitions:

$Z_i(Z)$ = fixed coordinate frame at the centre of the earth

$z_i(z)$ = frame that rotates with a spacecraft's orbit

$y_i(y)$ = coordinate frame fixed to the mass centre of the spacecraft

A_{ij} = rotation of earth's rotating frame with respect to earth's fixed frame

α_{ij} = rotation of spacecraft with respect to the earth's rotating frame

$c_i(z)$ = position of the origin of the spacecraft's frame with respect to the earth's frame.

Movement of a particular experiment with respect to the spacecraft's frame are not considered in this model – the spacecraft is assumed to be rigid, similar to the analysis by [7]. By this assumption, the spacecraft translations and rotations alone are used to demonstrate the effects of motion on the experiment. In reality, these motions would also include vibrations and deflections within the spacecraft structure [34]. It is important to note, however, that structural vibrations and deflections would also result in some rotational motion of the experimental frame.

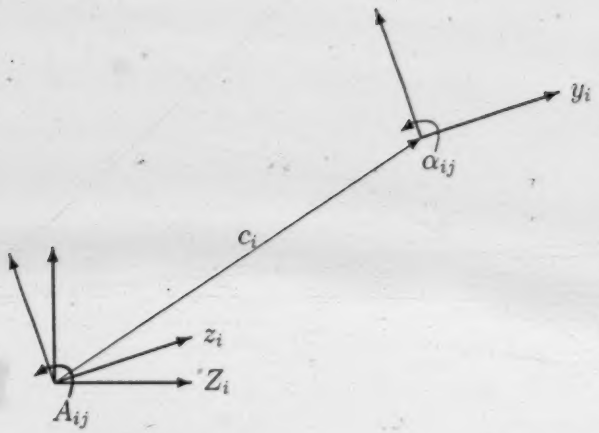

Figure 2.1: Moving Coordinates 'z_i' and 'y_i' and Fixed Coordinates 'Z_i'

The relations between the position vectors are described with the following transformations [21]:

$$Z_i(Z) = z_i(Z) \tag{2.1}$$

$$Z_i(Z) = A_{ji} z_j(z) \tag{2.2}$$

$$z_j(z) = \alpha_{kj} y_k(y) + c_j(z) \tag{2.3}$$

Combining equations (2.2) and (2.3) gives a complete equation for position:

$$Z_i = A_{ji}(\alpha_{kj} y_k + c_j) \tag{2.4}$$

With the relationship for position now established, the velocity and acceleration in the fluid field can now be derived. Differentiating the complete

position equation (2.4) with respect to time gives velocity V_i in a absolute, inertial sense:

$$V_i = \frac{DZ_i}{Dt} = \frac{DA_{ji}}{Dt}(\alpha_{kj}y_k + c_j) + A_{ji}\left(\frac{D\alpha_{kj}}{Dt}y_k + \alpha_{kj}\frac{Dy_k}{Dt} + \frac{Dc_j}{Dt}\right) \quad (2.5)$$

Taking the total time derivative again gives absolute acceleration:

$$\begin{aligned}\frac{D^2Z_i}{Dt^2} &= \frac{D^2A_{ji}}{Dt^2}(\alpha_{kj}y_k + c_j) + 2\frac{DA_{ji}}{Dt}\left(\frac{D\alpha_{kj}}{Dt}y_k + \alpha_{kj}\frac{Dy_k}{Dt} + \frac{Dc_j}{Dt}\right) \\ &\quad + A_{ji}\left(\frac{D^2\alpha_{kj}}{Dt^2}y_k + 2\frac{D\alpha_{kj}}{Dt}\frac{Dy_k}{Dt} + \alpha_{kj}\frac{D^2y_k}{Dt^2} + \frac{D^2c_j}{Dt^2}\right) \quad (2.6)\end{aligned}$$

These equations of position, velocity, and acceleration will be used in the derivation of the equations of fluid motion. As such, it is useful to express the relative motion in terms of rotation rate tensors in addition to the rotation tensors. To this end, the relationship between the rotation tensors A_{ij} and α_{ij} and their corresponding rotation rate tensors Ω_{ij} and Ω'_{ij} are now stated as given by Wrede[35], and are explained in detail in appendix A.

$$A_{ri}\frac{DA_{ji}}{Dt} = \Omega_{rj} \quad ; \quad \alpha_{ri}\frac{D\alpha_{ji}}{Dt} = \Omega'_{rj} \quad (2.7)$$

To help in the reduction of the resulting equation, some more properties of rotation and rotation rate tensors are stated, but are again explained in more detail in appendix A:

$$A_{ij}A_{kj} = \delta_{ik} \quad ; \quad \alpha_{ij}\alpha_{kj} = \delta_{ik} \quad (2.8)$$

$$\Omega_{ii} = \Omega'_{jj} = 0 \quad (2.9)$$

$$\frac{DA_{kj}}{Dt} = A_{sj}\Omega_{sk} \quad ; \quad \frac{D\alpha_{kj}}{Dt} = \alpha_{sj}\Omega'_{sk} \quad (2.10)$$

The second derivatives of the rotation tensors can be expressed as:

$$\frac{D^2 A_{kj}}{Dt^2} = A_{gj}\left(\frac{D\Omega_{gk}}{Dt} - \Omega_{hg}\Omega_{hk}\right) \tag{2.11}$$

$$\frac{D^2 \alpha_{kj}}{Dt^2} = \alpha_{gj}\left(\frac{D\Omega'_{gk}}{Dt} - \Omega'_{hg}\Omega'_{hk}\right) \tag{2.12}$$

By these properties, the velocity and acceleration expressions (equations 2.5 and 2.6) are rewritten as:

$$\frac{DZ_i}{Dt} = A_{si}\Omega_{sj}(\alpha_{kj}y_k + c_j) + A_{ji}\left(\alpha_{sj}\Omega'_{sk}y_k + \alpha_{kj}\frac{Dy_k}{Dt} + \frac{Dc_j}{Dt}\right) \tag{2.13}$$

and

$$\begin{aligned}\frac{D^2 Z_i}{Dt^2} = {} & A_{gi}\left(\frac{D\Omega_{gj}}{Dt} - \Omega_{hg}\Omega_{hj}\right)(\alpha_{kj}y_k + c_j) \\ & + 2A_{mi}\Omega_{mj}\left(\alpha_{sj}\Omega'_{sk}y_k + \alpha_{kj}\frac{Dy_k}{Dt} + \frac{Dc_j}{Dt}\right) \\ & + A_{ji}\left[\alpha_{gj}\left(\frac{D\Omega'_{gk}}{Dt} - \Omega'_{hg}\Omega'_{hk}\right)y_k\right. \\ & \left. + 2\alpha_{sj}\Omega'_{sk}\frac{Dy_k}{Dt} + \alpha_{kj}\frac{D^2 y_k}{Dt^2} + \frac{D^2 c_j}{Dt^2}\right]\end{aligned} \tag{2.14}$$

These equations for velocity and acceleration assume that the experiment is located at the centroid of the spacecraft. In order to allow for different locations and orientations of the experiment on board the spacecraft, another reference frame is defined by

$$y_i = y'_i + a_{ji}x_j \tag{2.15}$$

where $x_i = 0$ is located at the origin of the experiment, a_{ji} is a fixed-angle transformation of the experiment's frame with respect to the spacecraft's frame, and y'_i is the fixed distance between the center of mass of the spacecraft and the experiment's origin. Note that the x_j coordinate frame does not

move with respect to the spacecraft, but it does allow the angular orientation of the experiment within the spacecraft to be specified. In other words, the location and orientation of the experiment within the orbiting spacecraft can now be specified, but the rigid spacecraft assumption is maintained.

To implement this extra frame into equations (2.13) and (2.14) the velocity and acceleration of the 'y'-frame in terms of the experimental frame 'x' are established by once again taking total time derivatives:

$$\begin{aligned} \frac{Dy_i}{Dt} &= \frac{Dy_i'}{Dt} + \frac{Da_{ji}}{Dt} z_j + a_{ji} \frac{Dx_j}{Dt} \\ &= a_{ji} \frac{Dx_j}{Dt} = a_{ji} u_j \end{aligned} \tag{2.16}$$

and

$$\begin{aligned} \frac{D^2 y_i}{Dt^2} &= \frac{Da_{ji}}{dt} u_j + a_{ji} \frac{Du_j}{Dt} \\ &= a_{ji} \frac{Du_j}{Dt} \end{aligned} \tag{2.17}$$

where $\frac{Dx_j}{Dt} = u_j$ is the velocity in the experiment's frame.

Finally, the velocity and acceleration can be described in terms of the relative variables of the experimental 'x'-frame:

$$\begin{aligned} \frac{DZ_i}{Dt} &= V_i = A_{si}\Omega_{sj}(\alpha_{kj}(y_k' + a_{nk}x_n) + c_j) \\ &\quad + A_{ji}\left(\alpha_{sj}\Omega_{sk}'(y_k' + a_{nk}x_n) + \alpha_{kj}a_{nk}u_n + \frac{Dc_j}{Dt}\right) \end{aligned} \tag{2.18}$$

and

$$\frac{D^2 Z_i}{Dt^2} = \frac{DV_i}{Dt} = A_{gi}\left(\frac{D\Omega_{gj}}{Dt} - \Omega_{hg}\Omega_{hj}\right)(\alpha_{kj}(y_k' + a_{nk}x_n) + c_j)$$

$$+2A_{mi}\Omega_{mj}\left(\alpha_{sj}\Omega'_{sk}(y'_k + a_{nk}x_n) + \alpha_{kj}a_{nk}u_n + \frac{Dc_j}{Dt}\right)$$
$$+A_{ji}\left[\alpha_{gj}\left(\frac{D\Omega'_{gk}}{Dt} - \Omega'_{hg}\Omega'_{hk}\right)(y'_k + a_{nk}x_n)\right.$$
$$\left.+2\alpha_{sj}\Omega'_{sk}a_{nk}u_n + \alpha_{kj}a_{nk}\frac{Du_n}{Dt} + \frac{D^2c_j}{Dt^2}\right] \qquad (2.19)$$

where V_i represents the inertial velocity.

These expressions for velocity and accleration in the specified non-inertial frame of reference are ready for implementation into the equations of môtion for a fluid.

2.2 Equations of Motion

The motion of the fluid within the experiment itself is now described. The momentum equation in the standard inertial frame is first derived as a starting point for the ensuing description of fluid motion in terms of non-inertial variables.

The equation for the momentum principle can be expressed as [22]:

$$\frac{D}{Dt}\int_v \rho V_i dv = \int_v \rho f_i dv + \int_\sigma p_{ij}n_j d\sigma \qquad (2.20)$$

where the pressure term, p_{ij}, is expanded as $p_{ij} = -P\delta_{ij} + \tau_{ij}$ and $\tau_{ii} = 0$ for a Newtonian, incompressible fluid. P is the thermodynamic pressure and τ_{ij} is the viscous stress tensor. Also, ρ is the fluid density, f_i represent the body forces, V_i is velocity in the inertial frame, v is an arbitrary volume, and n_j is the normal vector to surface σ.

For the eventual numerical analysis, it is desirable to express the momentum equation in conservation form. First, the transport theorem gives:

$$\int_v (\frac{D\rho V_i}{Dt} + \rho V_i \frac{\partial V_j}{\partial Z_j}) dv = \int_v \rho f_i dv + \int_\sigma p_{ij} n_j d\sigma$$

To express the integrals only in terms of the arbitrary volume v, the divergence theorem is applied:

$$\int_v (\frac{D\rho V_i}{Dt} + \rho V_i \frac{\partial V_j}{\partial Z_j}) dv = \int_v \rho f_i dv + \int_v \frac{\partial p_{ij}}{\partial Z_j} dv$$

Since the volume v is arbitrary,

$$\frac{D\rho V_i}{Dt} + \rho V_i \frac{\partial V_j}{\partial Z_j} = \rho f_i + \frac{\partial p_{ij}}{\partial Z_j} \tag{2.21}$$

This is the final form of the inertial momentum equation that will now be transformed to be in terms of non-inertial coordinates.

2.3 Modified Equations of Motion

The relative frames analysis now puts the equation of motion for the fluid, equation (2.21), in terms of non-inertial variables. The absolute spatial variables Z_i must be converted to the relative variables x_i, and the absolute velocity and acceleration, V_i and $\frac{DV_i}{Dt}$, must be expressed in terms of relative velocity u_i and relative acceleration $\frac{Du_i}{Dt}$.

The first difficulty comes when trying to define the partial spatial derivatives $\frac{\partial}{\partial Z_i}$ in terms of the relative variables as $\frac{\partial}{\partial x_i}$. To begin, the relative descriptions of position, given by equations (2.2), (2.3), and (2.15) are inverted. Making use of the rotation tensor property from equation (2.8), the

inversion goes as:

$$\begin{aligned} Z_j &= A_{hj} z_h \\ A_{rj} Z_j &= A_{rj} A_{hj} z_h = \delta_{rh} z_h = z_r \end{aligned} \tag{2.22}$$

similarly,

$$\alpha_{qr}(z_r - c_r) = y_q \tag{2.23}$$

and

$$a_{sq}(y_q - y'_q) = x_s \tag{2.24}$$

With these inversions in mind, the transformation of the partial derivatives from an inertial to a non-inertial frame can now be derived:

$$\frac{\partial}{\partial Z_j} = \frac{\partial z_r}{\partial Z_j}\frac{\partial y_q}{\partial z_r}\frac{\partial x_s}{\partial y_q}\frac{\partial}{\partial x_s} = A_{rj}\alpha_{qr}a_{sq}\frac{\partial}{\partial z_s} \tag{2.25}$$

A number of substitutions can now be made to express the the inertial momentum equation, equation (2.21), in terms of the non-inertial variables x_i and u_i (representing relative position and relative velocity). For the sake of simplicity, these substitutions are performed in two steps. First, equation (2.25) is implemented in order to transform the partial derivatives to relative variables:

$$\frac{D\rho V_i}{Dt} + \rho V_i A_{rj}\alpha_{qr}a_{sq}\frac{\partial V_j}{\partial x_s} = \rho f_i + A_{rj}\alpha_{qr}a_{sq}\frac{\partial p_{ij}}{\partial x_s} \tag{2.26}$$

or

$$\frac{D\rho}{Dt}V_i + \rho\frac{DV_i}{Dt} + \rho A_{rj}\alpha_{qr}a_{sq}V_i\frac{\partial V_j}{\partial x_s} = \rho f_i + A_{rj}\alpha_{qr}a_{sq}\frac{\partial p_{ij}}{\partial x_s} \tag{2.27}$$

The second step is to substitute equations (2.18) and (2.19) for velocity and acceleration to complete the re-expression of the momentum equation in terms of relative variables.

$$\begin{aligned}
&\frac{D\rho}{Dt}\left[A_{si}\Omega_{sj}(\alpha_{kj}(y'_k+a_{nk}x_n)+c_j)\right.\\
&\qquad\left.+A_{ji}\left(\alpha_{sj}\Omega'_{sk}(y'_k+a_{nk}x_n)+\alpha_{kj}a_{nk}u_n+\frac{Dc_j}{Dt}\right)\right]\\
&+\rho A_{gi}\left(\frac{D\Omega_{gj}}{Dt}-\Omega_{hg}\Omega_{hj}\right)(\alpha_{kj}(y'_k+a_{nk}x_n)+c_j)\\
&+2\rho A_{mi}\Omega_{mj}\left(\alpha_{sj}\Omega'_{sk}(y'_k+a_{nk}x_n)+\alpha_{kj}a_{nk}u_n+\frac{Dc_j}{Dt}\right)\\
&+\rho A_{ji}\left[\alpha_{gj}\left(\frac{D\Omega'_{gk}}{Dt}-\Omega'_{hg}\Omega'_{hk}\right)(y'_k+a_{nk}x_n)\right.\\
&\qquad\left.+2\alpha_{sj}\Omega'_{sk}a_{nk}u_n+\alpha_{kj}a_{nk}\frac{Du_n}{Dt}+\frac{D^2c_j}{Dt^2}\right]\\
&+\left[A_{si}\Omega_{sj}(\alpha_{kj}(y'_k+a_{nk}x_n)+c_j)\right.\\
&\qquad\left.+A_{ji}\left(\alpha_{sj}\Omega'_{sk}(y'_k+a_{nk}z_n)+\alpha_{kj}a_{nk}u_n+\frac{Dc_j}{Dt}\right)\right]\\
&\left\{\rho A_{rj}\alpha_{qr}a_{sq}\frac{\partial}{\partial x_s}\left[A_{tj}\Omega_{to}(\alpha_{po}(y'_p+a_{ap}x_a)+c_o)\right.\right.\\
&\qquad\left.\left.+A_{oj}\left(\alpha_{to}\Omega'_{tp}(y'_p+a_{ap}x_a)+\alpha_{po}a_{ap}u_a+\frac{Dc_o}{Dt}\right)\right]\right\}\\
&\qquad=\rho f_i+A_{rj}\alpha_{qr}a_{sq}\frac{\partial p_{ij}}{\partial x_s}
\end{aligned}\tag{2.28}$$

This equation is quite long and cumbersome, and does not lend itself easily to interpretation. Fortunately, this equation simplifies significantly with the use of the rotation tensor properties and the equation for the conservation of mass. First, the rotation tensor properties given by (2.8) and (2.9) are used to reduce the term in curly brackets { }, which is extracted here:

$$\left\{\rho A_{rj}\alpha_{qr}a_{sq}\frac{\partial}{\partial x_s}\left[A_{tj}\Omega_{to}(\alpha_{po}(y'_p+a_{ap}x_a)+c_o)\right.\right.$$

$$
\begin{aligned}
&\quad + A_{oj}\left(\alpha_{to}\Omega'_{tp}(y'_p + a_{ap}x_a) + \alpha_{po}a_{ap}u_a + \frac{Dc_o}{Dt}\right)\Big]\Big\} \\
&= \rho A_{rj}A_{tj}\alpha_{qr}\alpha_{po}\Omega_{to}a_{sq}a_{ap}\frac{\partial x_a}{\partial x_s} + \rho A_{rj}A_{oj}\alpha_{qr}\alpha_{to}\Omega'_{tp}a_{sq}a_{ap}\frac{\partial x_a}{\partial x_s} \\
&\quad + \rho A_{rj}A_{oj}\alpha_{qr}\alpha_{po}a_{sq}a_{ap}\frac{\partial u_a}{\partial x_s} \\
&= \rho\delta_{rt}\alpha_{qr}\alpha_{po}\Omega_{to}a_{sq}a_{ap}\delta_{as} + \rho\delta_{ro}\alpha_{qr}\alpha_{to}\Omega'_{tp}a_{sq}a_{ap}\delta_{as} \\
&\quad + \rho\delta_{ro}\alpha_{qr}\alpha_{po}a_{sq}a_{ap}\frac{\partial u_a}{\partial x_s} \\
&= \rho\delta_{rt}\alpha_{qr}\alpha_{po}\Omega_{to}a_{aq}a_{ap} + \rho\delta_{ro}\alpha_{qr}\alpha_{to}\Omega'_{tp}a_{aq}a_{ap} + \rho\alpha_{qo}\alpha_{po}a_{sq}a_{ap}\frac{\partial u_a}{\partial x_s} \\
&= \rho\alpha_{qt}\alpha_{po}\Omega_{to}\delta_{qp} + \rho\alpha_{qo}\alpha_{to}\Omega'_{tp}\delta_{qp} + \rho\delta_{qp}a_{sq}a_{ap}\frac{\partial u_a}{\partial x_s} \\
&= \rho\alpha_{pt}\alpha_{po}\Omega_{to} + \rho\alpha_{po}\alpha_{to}\Omega'_{tp} + \rho a_{sp}a_{ap}\frac{\partial u_a}{\partial x_s} \\
&= \rho\delta_{to}\Omega_{to} + \rho\delta_{tp}\Omega'_{tp} + \rho\delta_{sa}\frac{\partial u_a}{\partial x_s} \\
&= 0 + 0 + \rho\frac{\partial u_s}{\partial x_s} \qquad (2.29)
\end{aligned}
$$

Using this simplification and rearranging some terms, equation (2.28) can now be restated as:

$$
\begin{aligned}
&\left(\frac{D\rho}{Dt} + \rho\frac{\partial u_s}{\partial x_s}\right)\left[A_{si}\Omega_{sj}(\alpha_{kj}(a_{nk}x_n + y'_k) + c_j)\right. \\
&\qquad \left. + A_{ji}\left(\alpha_{sj}\Omega'_{sk}(a_{nk}x_n + y'_k) + \alpha_{kj}a_{nk}u_n + \frac{Dc_j}{Dt}\right)\right] \\
&+ \rho A_{gi}\left(\frac{D\Omega_{gj}}{Dt} - \Omega_{hg}\Omega_{hj}\right)(\alpha_{kj}(a_{nk}x_n + y'_k) + c_j) \\
&+ 2\rho A_{mi}\Omega_{mj}\left(\alpha_{sj}\Omega'_{sk}(a_{nk}x_n + y'_k) + \alpha_{kj}a_{nk}u_n + \frac{Dc_j}{Dt}\right) \\
&+ \rho A_{ji}\left[\alpha_{gj}\left(\frac{D\Omega'_{gk}}{Dt} - \Omega'_{hg}\Omega'_{hk}\right)(a_{nk}x_n + y'_k)\right. \\
&\qquad \left. + 2\alpha_{sj}\Omega'_{sk}a_{nk}u_n + \alpha_{kj}a_{nk}\frac{Du_n}{Dt} + \frac{D^2c_j}{Dt^2}\right] \\
&\qquad = \rho f_i + A_{rj}\alpha_{qr}a_{sq}\frac{\partial p_{ij}}{\partial x_s} \qquad (2.30)
\end{aligned}
$$

The conservation of mass holds true independent of the reference frame being employed and is shown here in terms of non-inertial variables:

$$\left(\frac{D\rho}{Dt} + \rho\frac{\partial u_q}{\partial x_q}\right) = 0 \tag{2.31}$$

The conservation of mass is now applied to eliminate some terms:

$$\begin{aligned}
&\left(\frac{D\rho}{Dt} + \rho\frac{\partial u_s}{\partial x_s}\right) A_{ji}\alpha_{kj}a_{nk}u_n \\
&\quad +\rho A_{gi}\left(\frac{D\Omega_{gj}}{Dt} - \Omega_{hg}\Omega_{hj}\right)(\alpha_{kj}(a_{nk}x_n + y'_k) + c_j) \\
&\quad +2\rho A_{mi}\Omega_{mj}\left(\alpha_{sj}\Omega'_{sk}(a_{nk}x_n + y'_k) + \alpha_{kj}a_{nk}u_n + \frac{Dc_j}{Dt}\right) \\
&\quad +\rho A_{ji}\left[\alpha_{gj}\left(\frac{D\Omega'_{gk}}{Dt} - \Omega'_{hg}\Omega'_{hk}\right)(a_{nk}x_n + y'_k)\right. \\
&\qquad\qquad \left. +2\alpha_{sj}\Omega'_{sk}a_{nk}u_n + \alpha_{kj}a_{nk}\frac{Du_n}{Dt} + \frac{D^2c_j}{Dt^2}\right] \\
&\qquad\qquad = \rho f_i + A_{rj}\alpha_{qr}a_{sq}\frac{\partial p_{ij}}{\partial x_s}
\end{aligned} \tag{2.32}$$

Note that the conservation of mass is not applied to eliminate all possible terms since some terms are required to arrange the equation in a way that is conducive to numerical analysis. This rearrangement is given in section 2.3.1.

In an effort to match the terms of equation (2.32) to the terms of the inertial momentum equation (2.21), all terms involving derivatives of velocity (both total and partial) are moved to the left hand side, while all others are moved to the right:

$$\begin{aligned}
&\left(\frac{D\rho}{Dt} + \rho\frac{\partial u_s}{\partial x_s}\right) A_{ji}\alpha_{kj}a_{nk}u_n + \rho A_{ji}\alpha_{kj}a_{nk}\frac{Du_n}{Dt} = \rho f_i + A_{rj}\alpha_{qr}a_{sq}\frac{\partial p_{ij}}{\partial x_s} \\
&\quad -\rho A_{gi}\Omega_{gh}\Omega_{hj}(\alpha_{kj}(a_{nk}x_n + y'_k) + c_j) - \rho A_{ji}\alpha_{gj}\Omega'_{gh}\Omega'_{hk}(a_{nk}x_n + y'_k) \\
&\qquad -2\rho A_{mi}\alpha_{sj}\Omega_{mj}\Omega'_{sk}(a_{nk}x_n + y'_k)
\end{aligned}$$

$$
\begin{aligned}
&-2\rho A_{mi}\Omega_{mj}\left(\alpha_{kj}a_{nk}u_n + \frac{Dc_j}{Dt}\right) - 2\rho A_{ji}\alpha_{sj}\Omega'_{sk}a_{nk}u_n \\
&-\rho A_{gi}\frac{D\Omega_{gj}}{Dt}(\alpha_{kj}(a_{nk}x_n + y'_k) + c_j) - \rho A_{ji}\alpha_{gj}\frac{D\Omega'_{gk}}{Dt}(a_{nk}x_n + y'_k) \\
&-\rho A_{ji}\frac{D^2c_j}{Dt^2}
\end{aligned} \tag{2.33}
$$

This equation represents a very general form of the momentum equation in terms of non-inertial variables.

2.3.1 Breakdown to sum of partial derivatives

In its general form, the relative momentum equation given by equation (2.33) is difficult to interpret and even more difficult to model numerically. At this point, some assumptions are made enabling more simplification of the terms. The equation can then be re-expressed in a more familiar sense, where the non-inertial momentum equation compares directly to the inertial equation except for the addition of several source terms.

The first assumption made is that the fluid is inviscid. The importance of this assumption will be discussed further in section 2.4, but the immediate implication is that the viscous stress tensor, τ, is eliminated such that the pressure term is:

$$
\begin{aligned}
A_{rj}\alpha_{qr}a_{sq}\frac{\partial}{\partial x_s}(-P\delta_{ij} + \tau_{ij}) &= -A_{rj}\alpha_{qr}a_{sq}\frac{\partial P\delta_{ij}}{\partial x_s} \\
&= -A_{rj}\alpha_{qr}a_{sq}\delta_{ij}\frac{\partial P}{\partial x_s} \\
&= -A_{rj}\alpha_{qr}a_{sq}\frac{\partial P}{\partial x_s}
\end{aligned} \tag{2.34}
$$

which once again makes use of equation (2.8).

The second assumption made is that the only body force f_i experienced by the fluid is due to the pull of the earth's gravity. This means that the gravity that results from the mass of the spacecraft and its contents as well as other celestial bodies is not taken into account. Further, it is assumed that the earth's gravity is a function of altitude only. The result is that the body force is most easily expressed in the z_i coordinate frame, acting as a function of z_i as:

$$\rho f_i = \rho A_{ji} g_j(z_i) \tag{2.35}$$

where $g_j(z_i)$ represents the gravitational acceleration from the earth at a distance z_i from the center of the earth. In this way, the gravitational acceleration acting at each point in the fluid is defined. The exact definition of g_j will be shown in section (2.5.1).

There remains one final step in expressing equation (2.33) as an equaivalent to the inertial form. By multiplying each term by a rotation from each frame and making use once again of equation (2.8), only the source terms are left with rotation tensors. To that end, equation (2.33) is multiplied by

$$A_{ti}\alpha_{rt}a_{er}$$

to give:

$$\begin{aligned}
&\left(\frac{D\rho}{Dt} + \rho\frac{\partial u_s}{\partial x_s}\right) A_{ti}\alpha_{rt}a_{er}A_{ji}\alpha_{kj}a_{nk}u_n + \rho A_{ti}\alpha_{rt}a_{er}A_{ji}\alpha_{kj}a_{nk}\frac{Du_n}{Dt} \\
= \;& \rho A_{ti}\alpha_{rt}a_{er}A_{ji}g_j - A_{ti}\alpha_{rt}a_{er}A_{rj}\alpha_{qr}a_{sq}\frac{\partial P}{\partial x_s} \\
& -\rho A_{ti}\alpha_{rt}a_{er}A_{gi}\Omega_{gh}\Omega_{hj}(\alpha_{kj}(a_{nk}x_n + y'_k) + c_j) \\
& -\rho A_{ti}\alpha_{rt}a_{er}A_{ji}\alpha_{gj}\Omega'_{gh}\Omega'_{hk}(a_{nk}x_n + y'_k)
\end{aligned}$$

$$
\begin{aligned}
&-2\rho A_{ti}\alpha_{rt}a_{er}A_{mi}\alpha_{sj}\Omega_{mj}\Omega'_{sk}(a_{nk}x_n + y'_k) \\
&-2\rho A_{ti}\alpha_{rt}a_{er}A_{mi}\Omega_{mj}\left(\alpha_{kj}a_{nk}u_n + \frac{Dc_j}{Dt}\right) \\
&-2\rho A_{ti}\alpha_{rt}a_{er}A_{ji}\alpha_{sj}\Omega'_{sk}a_{nk}u_n \\
&-\rho A_{ti}\alpha_{rt}a_{er}A_{gi}\frac{D\Omega_{gj}}{Dt}(\alpha_{kj}(a_{nk}x_n + y'_k) + c_j) \\
&-\rho A_{ti}\alpha_{rt}a_{er}A_{ji}\alpha_{gj}\frac{D\Omega'_{gk}}{Dt}(a_{nk}x_n + y'_k) - \rho A_{ti}\alpha_{rt}a_{er}A_{ji}\frac{D^2c_j}{Dt^2} \quad (2.36)
\end{aligned}
$$

noting that this equation involves the assumptions from equations (2.34) and (2.35).

Now, by simply applying the rotation tensor properties

$$A_{ti}A_{ji} = \delta_{tj}$$

$$\alpha_{rt}\alpha_{kt} = \delta_{kr}$$

and

$$a_{er}a_{nr} = \delta_{en}$$

the momentum equation is simply:

$$
\begin{aligned}
&\left(\frac{D\rho}{Dt} + \rho\frac{\partial u_s}{\partial x_s}\right)u_e + \rho\frac{Du_e}{Dt} = \rho a_{er}\alpha_{rt}g_t - \frac{\partial P}{\partial x_e} \\
&\quad -\rho a_{er}\alpha_{rt}\Omega_{th}\Omega_{hj}(\alpha_{kj}(a_{nk}x_n + y'_k) + c_j) - \rho a_{er}\Omega'_{rh}\Omega'_{hk}(a_{nk}x_n + y'_k) \\
&\qquad -2\rho a_{er}\alpha_{rt}\alpha_{sj}\Omega_{tj}\Omega'_{sk}(a_{nk}x_n + y'_k) \\
&\quad -2\rho a_{er}\alpha_{rt}\Omega_{tj}\left(\alpha_{kj}a_{nk}u_n + \frac{Dc_j}{Dt}\right) - 2\rho a_{er}\Omega'_{rk}a_{nk}u_n \\
&\quad -\rho a_{er}\alpha_{rt}\frac{D\Omega_{tj}}{Dt}(\alpha_{kj}(a_{nk}x_n + y'_k) + c_j) - \rho a_{er}\frac{D\Omega'_{rk}}{Dt}(a_{nk}x_n + y'_k) \\
&\quad -\rho a_{er}\alpha_{rt}\frac{D^2c_t}{Dt^2} \qquad (2.37)
\end{aligned}
$$

This equation is now easily compared to equation (2.21). Each of the first 4 terms in equation (2.37) corresponds to a term in (2.21), and all subsequent terms are the source terms resulting from the relative motion of the coordinate frames.

As a final step to presenting the equations in a way that is conducive to numerical analysis, the material derivatives of velocity and density are expanded and written in terms of partial derivatives. The material derivative can be expanded by:

$$\frac{D}{Dt} = \frac{\partial}{\partial t} + u_j \frac{\partial}{\partial x_j} \tag{2.38}$$

So the left hand side of equation (2.37) can be expressed as:

$$\begin{aligned}
&\left(\frac{D\rho}{Dt} + \rho\frac{\partial u_s}{\partial x_s}\right) u_e + \rho\frac{Du_e}{Dt} \\
&\quad = \frac{\partial \rho}{\partial t}u_e + u_s\frac{\partial \rho}{\partial x_s}u_e + \rho\frac{\partial u_s}{\partial x_s}u_e + \rho\frac{\partial u_e}{\partial t} + \rho u_s\frac{\partial u_e}{\partial x_s} \\
&\quad = \frac{\partial \rho u_e}{\partial t} + \frac{\partial \rho u_e u_s}{\partial x_s}
\end{aligned} \tag{2.39}$$

The momentum equation expressed in non-inertial coordinates can now be expressed in a form suitable for interpretation as well as numerical analysis. Making use of the expanded material derivative for velocity and density, and switching the unsummed 'e' index for the more familiar 'i', the result is:

$$\begin{aligned}
&\frac{\partial \rho u_i}{\partial t} + \frac{\partial \rho u_i u_s}{\partial x_s} + \frac{\partial P}{\partial x_i} = \rho a_{ir}\alpha_{rt} g_t \\
&\quad -\rho a_{ir}\alpha_{rt}\Omega_{th}\Omega_{hj}(\alpha_{kj}(a_{nk}x_n + y'_k) + c_j) - \rho a_{ir}\Omega'_{rh}\Omega'_{hk}(a_{nk}x_n + y'_k) \\
&\qquad -2\rho a_{ir}\alpha_{rt}\alpha_{sj}\Omega_{tj}\Omega'_{sk}(a_{nk}x_n + y'_k) \\
&\quad -2\rho a_{ir}\alpha_{rt}\Omega_{tj}\left(\alpha_{kj}a_{nk}u_n + \frac{Dc_j}{Dt}\right) - 2\rho a_{ir}\Omega'_{rk}a_{nk}u_n
\end{aligned}$$

$$-\rho a_{ir}\alpha_{rt}\frac{D\Omega_{tj}}{Dt}(\alpha_{kj}(a_{nk}x_n + y'_k) + c_j) - \rho a_{ir}\frac{D\Omega'_{rk}}{Dt}(a_{nk}x_n + y'_k)$$
$$-\rho a_{ir}\alpha_{rt}\frac{D^2 c_t}{Dt^2} \tag{2.40}$$

2.3.2 Rotation tensor components

With the momentum equation derivation complete for a relative frames analysis, the first steps are now taken to establish values for the source terms. The equation (2.40) involves a number of parameters that will need specific values. These will be addressed with the model of spacecraft motion as described in section 2.5.1, where translational and rotational motion values are prescribed based on a uni-axial, sinusoidally-varying body force model. The rotational motion given by the model is expressed as time varying angles Θ and θ, but at this point, the rotational motion in the momentum equation is given in terms of rotation and rotation rate tensors. The components of these tensors are now therefore reduced to functions of angles Θ and θ.

To adhere to the spacecraft motion model, the coordinate frames are constrained to two-dimensional motion. This does not necessarily mean that the frames themselves must be two-dimensional, only that their motion is purely planar. To begin, the components of the rotation tensors in two dimensions are specified:

$$\begin{aligned} \alpha_{ji} \Rightarrow \alpha_{11} &= \cos\theta \\ \alpha_{12} &= \sin\theta \\ \alpha_{21} &= -\sin\theta \\ \alpha_{22} &= \cos\theta \end{aligned} \tag{2.41}$$

$$
\begin{aligned}
A_{ji} \Rightarrow A_{11} &= \cos\Theta \\
A_{12} &= \sin\Theta \\
A_{21} &= -\sin\Theta \\
A_{22} &= \cos\Theta
\end{aligned} \tag{2.42}
$$

where θ is the angle of rotation of the spacecraft's frame and Θ represents the orientation of the earth-based rotating coordinate frame with respect to the inertial frame. Since we are only considering two dimensions, these angles are rotated about the 3rd axis of their respective frames. In other words, $\theta = \theta_3$, with $\theta_1 = \theta_2 = 0$ and $\Theta = \Theta_3$, with $\Theta_1 = \Theta_2 = 0$.

It is now possible to express the rotation rate tensors in terms of a function of the angles. First consider the time derivatives of the components of α_{ji} from (2.41):

$$
\begin{aligned}
\frac{D\alpha_{11}}{Dt} &= -\frac{d\theta}{dt}\sin\theta \\
\frac{D\alpha_{12}}{Dt} &= \frac{d\theta}{dt}\cos\theta \\
\frac{D\alpha_{21}}{Dt} &= -\frac{d\theta}{dt}\cos\theta \\
\frac{D\alpha_{22}}{Dt} &= -\frac{d\theta}{dt}\sin\theta
\end{aligned} \tag{2.43}
$$

As explained, θ is a function of time only, reflected in the lower case 'd' used in the total derivative. Note that the rotation rate tensor components are not simply the time derivatives of the rotation tensor components, but, as shown previously in equation (2.7), the rotation rate Ω'_{rj} was defined as:

$$
\Omega'_{rj} = \alpha_{ri}\frac{D\alpha_{ji}}{Dt} \tag{2.44}
$$

Expanding the terms allows the use of the derivatives from equation (2.41) to be used to express the rotation rate tensors in terms of derivatives of the angles:

$$\begin{aligned}
\Omega'_{rj} &= \alpha_{r1}\frac{D\alpha_{j1}}{Dt} + \alpha_{r2}\frac{D\alpha_{j2}}{Dt} \\
\Omega'_{11} &= \alpha_{11}\frac{D\alpha_{11}}{Dt} + \alpha_{12}\frac{D\alpha_{12}}{Dt} = -\cos\theta\frac{d\theta}{dt}\sin\theta + \sin\theta\frac{d\theta}{dt}\cos\theta = 0 \\
\Omega'_{12} &= \alpha_{11}\frac{D\alpha_{21}}{Dt} + \alpha_{12}\frac{D\alpha_{22}}{Dt} = -\cos^2\theta\frac{d\theta}{dt} - \sin^2\theta\frac{d\theta}{dt} = -\frac{d\theta}{dt} \\
\Omega'_{21} &= \alpha_{21}\frac{D\alpha_{11}}{Dt} + \alpha_{22}\frac{D\alpha_{12}}{Dt} = \sin^2\theta\frac{d\theta}{dt} + \cos^2\theta\frac{d\theta}{dt} = \frac{d\theta}{dt} \\
\Omega'_{22} &= \alpha_{21}\frac{D\alpha_{21}}{Dt} + \alpha_{22}\frac{D\alpha_{22}}{Dt} = \sin\theta\frac{d\theta}{dt}\cos\theta - \cos\theta\frac{d\theta}{dt}\sin\theta = 0
\end{aligned} \tag{2.45}$$

Since the model of spacecraft motion will predict actual values for $\frac{d\theta_i}{dt}$, a vector q_i is defined to simplify the representation of these values:

$$q_i = \frac{d\theta_{\hat{i}}}{dt} \tag{2.46}$$

but since θ_i only rotates about axis 3 when considering two dimensions, $q_1 = q_2 = 0$ and $q_3 = \frac{d\theta_3}{dt}$.

Following the identical process for A_{ij} leads to:

$$Q_3 = \frac{d\Theta_3}{dt} \tag{2.47}$$

where $Q_1 = Q_2 = 0$.

Finally, the rotation rate tensors in the momentum equation (2.37) are replaced with the equivalent q_i or Q_i vector. Equations (2.45) and (2.46)

show that $\Omega'_{11} = 0$, $\Omega'_{12} = -q_3$, $\Omega'_{21} = q_3$, and $\Omega'_{22} = 0$. This means that

$$\Omega'_{jk} = -\epsilon_{ijk} q_i \tag{2.48}$$

and

$$\Omega_{jk} = -\epsilon_{ijk} Q_i \tag{2.49}$$

where ϵ_{ijk} is the permutation tensor and when $i = 1$ or 2, $q_i = Q_i = 0$. These relations can be substituted directly into the momentum equation (2.40).

2.3.3 Reduction of terms

With the terms of the rotation tensors defined, many of the terms in equation (2.40) can be simplified. These simplifications are shown in detail in appendix C, but they primarily involve the identity

$$\epsilon_{pqi}\epsilon_{ijk} f_q g_j h_k - f_j g_j h_p \tag{2.50}$$

where f_i, g_i and h_i are arbitrary vectors. This identity is made useful by the subsitutions of (2.48) and (2.49) into the momentum equation. The other devices used for the simplification are the tensor properties from (2.8) and the planar motion assumption such that $q_i = q_3$ and $Q_i = Q_3$ only.

With the simplifications performed, the momentum equation (2.40) reduces to:

$$\begin{aligned}\frac{\partial \rho u_i}{\partial t} + \frac{\partial \rho u_i u_s}{\partial x_s} + \frac{\partial P}{\partial x_i} &= \rho a_{ir}\alpha_{rt} g_t \\ &+ \rho Q_3^2 (x_i + a_{ir} y'_r + a_{ir}\alpha_{rt} c_t) + \rho q_3^2 (x_i + a_{ir} y'_r) + 2\rho Q_3 q_3 (x_i + a_{ir} y'_r) \\ &- 2\rho Q_p [\epsilon_{ipk} u_k + a_{ir}\alpha_{rt}\epsilon_{tpj} \frac{Dc_j}{Dt}] - 2\rho \epsilon_{ijk} q_j u_k\end{aligned}$$

$$-\rho\frac{dQ_p}{dt}[\epsilon_{ipk}x_k + \epsilon_{jpk}a_{ij}y'_k + a_{ir}\alpha_{rt}\epsilon_{tpj}c_j] - \rho\frac{dq_p}{dt}[\epsilon_{ipk}x_k + a_{ir}\epsilon_{rpk}y'_k]$$
$$-\rho a_{ir}\alpha_{rt}\frac{D^2c_t}{Dt^2} \tag{2.51}$$

2.3.4 Summary of relative frames analysis

The momentum equation for fluid motion is derived using a relative frames analysis. With the use of multiple frames of reference, the resulting equation gives a great deal of flexibility in describing sources of motion. Moreover, some of the sources predicted by this analysis are unique in that they are non-conservative in a fluid of uniform density. By taking the curl of each of the terms, it was found that part of the sources dealing with angular acceleration:

$$-\rho\frac{dQ_p}{dt}\epsilon_{ipk}x_k$$

and

$$-\rho\frac{dq_p}{dt}\epsilon_{ipk}x_k$$

as well as the Coriolis source terms:

$$-2\rho Q_p[\epsilon_{ipk}u_k + a_{ir}\alpha_{rt}\epsilon_{tpj}\frac{Dc_j}{Dt}]$$

and

$$-2\rho\epsilon_{ijk}q_ju_k$$

could generate vorticity in the absence of a density gradient. Where a density gradient exists, however, all sources generate vorticity.

One of these non-conservative sources is especially critical. If only 2 dimensions are considered, the Coriolis terms become conservative. If the orbital angular velocity is constant, the only remaining non-consevative term

is associated with the angular acceleration of the spacecraft's frame, that is $\rho\dot{q}_p\epsilon_{ijpk}x_k$, or in vector form, $\rho\dot{\vec{q}} \times \vec{x}$. The unique aspect of this angular acceleration term is that it predicts rigid body motion of the fluid in the absence of physical boundaries. Note that in this term, there is no dependency on experiment location or orientation within the spacecraft. This results in an interesting realization – the shape of the cavity is critical in detemining non-conservative flow. This phenomenon will be investigated in chapter 4.

2.4 Fluid flow assumptions

Two main assumptions regarding the fluid itself are used in the derivation of the equations of motion. The first is that the flow is incompressible, which is believed to be a very accurate assumption based on the extremely low velocities being considered. The second assumption, that the flow is inviscid, is an approximation that requires justification.

2.4.1 Incompressible flow

Since it is expected that the fluid velocities resulting from the source terms will be much less than 1 m/s, incompressible flow is believed to be an accurate approximation. This approximation gives:

$$\frac{D\rho}{Dt} = 0 \tag{2.52}$$

This equation, combined with the conservation of mass (equation 2.31) also gives:

$$\frac{\partial u_i}{\partial x_i} = 0 \tag{2.53}$$

This last equation will play an important role in the numerical analysis.

2.4.2 Inviscid approximation

In this study, the effects of a standard and a relative frames model of microgravity are compared. It is found that the relative frames model predicts non-conservative sources of motion that are not predicted by microgravity models that simply use accelerations that vary sinusoidally with time. Although adding a model of viscosity to the fluid motion may help to increase the realism of the simulated flow, it would not add any significant insight or information to the comparison of the effects of the g-jitter models.

2.5 Model parameters

The motion of a fluid is represented by the momentum equation (2.51), which uses moving frames of reference to describe the source terms. In other words, these source terms arise from describing any arbitrary planar motion of an experiment using a non-inertial frame. The particular choice of reference frames lends itself easily to describe the motion of an orbiting spacecraft. The motion of such a spacecraft is now modeled so that actual values can be assigned to the parameters of the source terms. In particular, this is done such that the motion reproduces current models of microgravity sources as well as appropriate values for rotational motion.

As explained in section (1.1), many models of the microgravity environment assume a unidirectional acceleration that is sinusoidally varying with time. This acceleration can be reproduced by accelerating the spacecraft with an identical time varying function. The translational motion in the relative

frames analysis is thus specified, but one more critical assumption must be made to obtain rotational motion values. If the translational accelerations are aligned so as to create changes in altitude, then rotations can be created if the spacecraft pitch is aligned with its path. This rudimentary idea allows all values for the entire relative frames analysis to be specified using the same parameters values used for the simpler translational model.

It will be shown that this idealized model for spacecraft motion yields translational and rotational motion values expected aboard orbiting experimental platforms and, when applied to the relative frames derivation of the momentum equation, predicts source terms used by other microgravity models.

2.5.1 Spacecraft motion model

The model of the motion begins by assuming that the acceleration due to gravity is balanced by the centrifugal acceleration incurred by the spacecraft. As previously stated in section (2.3.1), the only gravity force being considered is generated by the earth's mass and is considered only to be a function of the distance of the point in question to the center of the earth.

As the equations of motion are prepared for numerical analysis, it will be important to express conservative source terms of gradients of potentials. With this in mind, the acceleration due to gravity in the z_i frame is described as a potential field:

$$a_{ir}\alpha_{rt}g_t = a_{ir}\alpha_{rt}\frac{-M_E G z_t}{|z_j|^3}$$

$$
\begin{aligned}
&= a_{ir}\alpha_{rt}\frac{\partial}{\partial z_t}\left(\frac{M_E G}{|z_j|}\right) \\
&= a_{ir}\alpha_{rt}\frac{\partial}{\partial z_t}\left(\frac{M_E G}{[z_j z_j]^{\frac{1}{2}}}\right) \qquad (2.54)
\end{aligned}
$$

where $M_E = 5.98 \times 10^{24} kg$ is the mass of the earth and $G = 6.673 \times 10^{-11} \frac{Nm^2}{kg^2}$ is the gravitational constant [29].

With the gravity term defined, it can now be transformed into the experimental coordinate frame:

$$
\begin{aligned}
&a_{ir}\alpha_{rt}g_t \\
&= a_{ir}\alpha_{rt}\frac{\partial}{\partial z_t}\left(\frac{M_E G}{[z_j z_j]^{\frac{1}{2}}}\right) \\
&= a_{ir}\alpha_{rt}\frac{\partial}{\partial z_t}\left(\frac{M_E G}{[(\alpha_{kj}y_k + c_j)(\alpha_{kj}y_k + c_j)]^{\frac{1}{2}}}\right) \\
&= a_{ir}\alpha_{rt}\frac{\partial}{\partial z_t}\left(\frac{M_E G}{[(\alpha_{kj}(y'_k + a_{nk}x_n) + c_j)(\alpha_{kj}(y'_k + a_{nk}x_n) + c_j)]^{\frac{1}{2}}}\right) \\
&= a_{ir}\alpha_{rt}\frac{\partial y_q}{\partial z_t}\frac{\partial x_s}{\partial y_q}\frac{\partial}{\partial x_s}\left(\frac{M_E G}{[(\alpha_{kj}(y'_k + a_{nk}x_n) + c_j)(\alpha_{kj}(y'_k + a_{nk}x_n) + c_j)]^{\frac{1}{2}}}\right) \\
&= a_{ir}\alpha_{rt}\alpha_{qt}a_{sq}\frac{\partial}{\partial x_s}\left(\frac{M_E G}{[(\alpha_{kj}(y'_k + a_{nk}x_n) + c_j)(\alpha_{kj}(y'_k + a_{nk}x_n) + c_j)]^{\frac{1}{2}}}\right) \\
&= a_{ir}\delta_{qr}a_{sq}\frac{\partial}{\partial x_s}\left(\frac{M_E G}{[(\alpha_{kj}(y'_k + a_{nk}x_n) + c_j)(\alpha_{kj}(y'_k + a_{nk}x_n) + c_j)]^{\frac{1}{2}}}\right) \\
&= a_{ir}a_{sr}\frac{\partial}{\partial x_s}\left(\frac{M_E G}{[(\alpha_{kj}(y'_k + a_{nk}x_n) + c_j)(\alpha_{kj}(y'_k + a_{nk}x_n) + c_j)]^{\frac{1}{2}}}\right) \\
&= \frac{\partial}{\partial x_i}\left(\frac{M_E G}{[(\alpha_{kj}(y'_k + a_{nk}x_n) + c_j)(\alpha_{kj}(y'_k + a_{nk}x_n) + c_j)]^{\frac{1}{2}}}\right) \\
&= \frac{\partial \gamma}{\partial x_i} \qquad (2.55)
\end{aligned}
$$

using γ to represent the scalar potential. The complexity of expressing the acceleration due to gravity in terms of the x_i reference frame reflects the

complexity of the motion. The gravity actually only acts in one direction, but describing that direction from the point of view of the experiment is quite convoluted.

In an ideal orbit, the centrifugal acceleration balances the gravitational acceleration. The value for the orbit rate, Q, is derived to satisfy this concept. First, a constant rate is assumed, so

$$\frac{dQ}{dt} = 0 \tag{2.56}$$

In a circular orbit with an altitude of 410 km [34], the gravity term at the centre of mass of the spacecraft balances the constant part of the centrifugal acceleration as follows:

$$\begin{aligned} \frac{\partial \gamma'}{\partial x_i} = \frac{M_E G}{(c')^2} &= Q^2 c' \\ \frac{(6.673 \times 10^{-11} \frac{Nm^2}{kg^2})(5.98 \times 10^{24} kg)}{(6.79 \times 10^6 m)^2} &= Q^2 (6.79 \times 10^6 m) \\ \Rightarrow Q &= 1.129 \times 10^{-3} rad/s \end{aligned} \tag{2.57}$$

where c' is the average orbit altitude plus the earth's radius $(4.1 \times 10^5 + 6.38 \times 10^6)$. $c_2 = 0$ because the z-frame rotates at the same rate as the spacecraft orbit. This angular velocity means that a single orbit of the earth takes 93 minutes.

By specifying the orbital rotation rate in this way, the balance of the centrifugal and gravitational terms from the relative frames analysis is assured. For example, the gravitational acceleration at a 410 km orbit is found to be approximately $8.7 m/s^2$. If gravity is applied independent of the rotation

rate, an error of 0.1% in the balance of gravitational and centrifugal accelerations would result in an erroneous acceleration in the order of $10^4 \mu g_0$ – an enormous value in the microgravity environment.

There is risk and benefit to using two such relatively large terms to balance each other. The risk comes into play when performing a numerical analysis. The truncation error has to be small enough to be able to accurately calculate the difference between the two large numbers, otherwise a large error may be introduced into the source term calculations. The benefit of expressing both the gravity and orbital centrifugal terms is that the small accelerations that occur as a result of moving away from the spacecraft's centroid are captured without any special treatment.

The translational motion of the spacecraft is now modeled. This motion is based on other microgravity models that use a sinusoidal acceleration oriented in a single direction. Fluctuations in altitude of the spacecraft are correspondingly modeled to generate these accelerations with the equation:

$$c_j(z) = c_1 = c' + \frac{ng_0}{\omega^2}\cos(\omega t) \tag{2.58}$$

where g_0 is the gravitational acceleration at sea level, or $9.81 m/s^2$; n is the maximum magnitude of the accelerations in the z_1 direction due to spacecraft motion expressed as a proportion of g_o; and ω is the frequency at which the altitude fluctuations occur. Once again, c' is the earth's average radius plus the average orbital altitude, giving a constant value for the distance of the spacecraft frame's origin to the center of the earth. Note that by this definition, c_i is only a function of time since all other parameters are set to

constant values.

The velocity of these vertical fluctuations is found by taking the time derivative of equation (2.58):

$$\frac{dc_j}{dt} = \dot{c}_j = \dot{c}_1 = -\frac{ng_o}{\omega}\sin\omega t \tag{2.59}$$

where c_j, is a function of time only as defined by equation (2.58).

With the vertical velocity defined, translational accelerations are simply the second derivative of (2.58):

$$\frac{d\dot{c}_1}{dt} = \ddot{c}_1 = -ng_0\cos(\omega t) \tag{2.60}$$

At this point, translational motion has been defined based on the sinusoidal microgravity model. In order to extend the model to predict values for rotation, the pitch of the spacecraft is assumed to follow the tangent line of its direction of travel. Here it is assumed that, over a short distance, the horizontal distance travelled is given by integrating the velocity due to the circular orbit:

$$z_2 = \text{horizontal distance} = Qc't \tag{2.61}$$

The tangent line to the direction of travel is then simply the slope of the vertical fluctuations compared against the horizontal distance. This slope is thus defined by:

$$\begin{aligned}\frac{dz_1}{dz_2} &= \frac{dz_1}{dt}\frac{dt}{dz_2} \\ &= \frac{-ng_0}{\omega}\sin(\omega t)\frac{1}{Qc'}\end{aligned}$$

The angle of this tangent line to the direction of travel is then found from simple trigonometry to be:

$$\theta = \arctan\left(\frac{-ng_0}{\omega Qc'}\sin(\omega t)\right) \tag{2.62}$$

Values for angular velocity can now be ascertained by taking the first time derivative of equation (2.62):

$$q_3 = \frac{d\theta}{dt} = -\frac{ng_0\cos^2(\theta)\cos(\omega t)}{Qc'} \tag{2.63}$$

Similarly, the value for angular acceleration is the second derivative:

$$\frac{dq_3}{dt} = \dot{q} = \frac{d^2\theta}{dt^2} = \frac{-ng_0[q\sin(2\theta)\cos(\omega t) - \omega\cos^2(\theta)\sin(\omega t)]}{Qc'} \tag{2.64}$$

The model of spacecraft motion is summarized in figure 2.2. In this figure, deviations from the ideal circular orbit are defined by the function for altitude, equation (2.58). Rotations of the spacecraft frame are generated when the spacecraft pitch is set to match the path.

One final variable is set to complete the parameter specifications. Although the capability exists to orient the experiment at any angle, the momentum equation can be simplified if it is assumed that the experiment's frame and the spacecraft's frame are aligned so that $a_{ij} = \delta_{ij}$. Since the orientation of the experiment is not considered to be of interest in this particular work, the simplification is applied leaving the momentum equation (2.51) as

$$\frac{\partial \rho u_i}{\partial t} + \frac{\partial \rho u_i u_s}{\partial x_s} + \frac{\partial P}{\partial x_i} = \rho\frac{\partial \gamma}{\partial x_i}$$
$$+\rho Q_3^2(x_i + y_i' + \alpha_{it}c_t) + \rho q_3^2(x_i + y_i') + 2\rho Q_3 q_3(x_i + y_i')$$

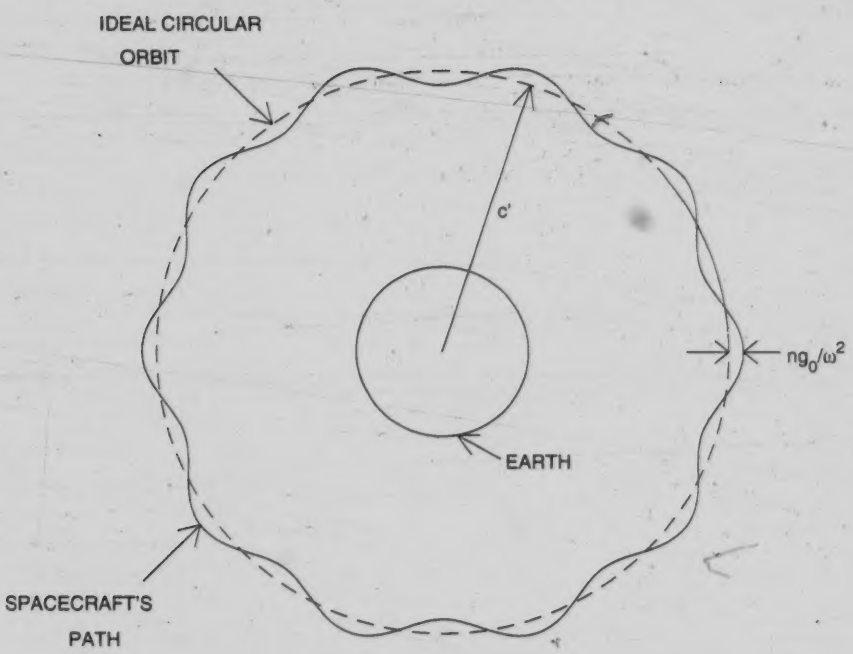

Figure 2.2: Summary of spacecraft motion model

$$-2\rho Q_p[\epsilon_{ipk}u_k + \alpha_{it}\epsilon_{tpj}\dot{c}_j] - 2\rho\epsilon_{ijk}q_j u_k$$
$$-\rho\dot{q}_p[\epsilon_{ipk}x_k + \epsilon_{ipk}y'_k] - \rho\alpha_{it}\ddot{c}_t \tag{2.65}$$

The model for spacecraft motion is now completely defined. With the input parameters of amplitude n and frequency ω taken from the simpler sinusoidal microacceleration model, all other parameters required for the relative frames analysis are determined.

2.5.2 Magnitudes of resulting source terms

A verification of the validity of the parameter values predicted by the model of motion is now performed. There are 8 source terms on the right hand side of the momentum equation, (2.65), as derived from the relative frames analysis. The magnitudes of these terms are compared to magnitudes of acceleration that are expected on an orbiting spacecraft.

One special case to note is the given by the gravity and centrifugal terms, the first and second source terms on the right hand side. Though these sources will be quite large compared to the other source terms, they are set to nearly balance each other by design, and as such, only the magnitude of their combination will be considered important.

A summary of the dimensional orders of magnitude of the source terms is given in table 3.12, where the experiment is assumed to be located at a distance of $10m$ from the centroid of the spacecraft. Intermediate values as defined by Duval and Jacqmin for source term amplitude and frequency [6] ($ng_0 = 9.81 \times 10^{-4}$ and $\omega = 1.0Hz$ respectively) will be used in these calculations. The velocity used to calculate the Coriolis accelerations (S5 and S6) is estimated at $100\mu m/sec.$

As expected, S1 and S2 are large but (S1+S2) is quite small. In fact, if the magnitudes of all the sources are summed, the resulting value is still of the same order of magnitude as the amplitude of the sinusoidally varying g-jitter model, which is $ng_0 = 9.81 \times 10^{-4}$. The use of the model for spacecraft

Source Label	Term	Maximum Order of Magnitude
S1	$\frac{\partial \gamma}{\partial x_i}$	10^1
S2	$Q^2(x_i + y_i' + \alpha_{it} c_t)$	10^1
S1+S2	—	10^{-5}
S3	$q^2(x_i + y_i')$	10^{-6}
S4	$2Qq(x_i + y_i')$	10^{-9}
S5	$-2Q_p[\epsilon_{ipk} u_k + \alpha_{it}\epsilon_{tpm}\dot{c}_m]$	10^{-6}
S6	$-2\epsilon_{ipk} q_p u_k$	10^{-11}
S7	$-\dot{q}_p \epsilon_{ipk}(x_k + y_k')$	10^{-6}
S8	$-\alpha_{it}\ddot{c}_t$	10^{-4}

Table 2.1: Orders of magnitude of the source terms

motion given in section 2.5.1 therefore does not raise the order of magnitude of the accelerations themselves.

2.5.3 Summary of model characteristics

The momentum equation (2.65) describes the fluid motion in a microgravity environment. The extra source terms from these equations have arisen by considering a relative frames analysis of the motion of a spacecraft. The spacecraft motion is modeled by assuming a circular orbit with fluctuations in altitude. These fluctuations correspond to the motion or accelerations predicted by g-jitter models that apply a sinusiodally varying acceleration in one direction. By simply allowing the pitch of the spacecraft follow its path,

angular motion is created. The model of motion is thus made complete with only three variable parameters: orbital altitude, and the magnitude and frequency of the sinusiodal g-jitter model.

As explained in section (1.1), the use of moving frames of reference to describe the microgravity environment is not new. Though these models may not be common, the nature of the source terms produced by such descriptions have been shown to be potentially significant in predicting fluid flow. Even in a fluid of uniform density, the motion associated with angular accelerations as well as the Coriolis accelerations are non-conservative and as such can generate vorticity (though in 2-dimensional flow, the Coriolis accelerations reduce to potential source terms).

The model presented in section (2.5.1) allows the simple sinusoidally varying g-jitter model to be easily extended to predict rotational motion. Without the use of any extra parameters, all sources generated by the relative frames analysis (including the the non-conservative sources) can be completely defined. In this way, the model presents a bridge between the g-jitter models to the relative frames models.

To demonstrate the effectiveness of this model, consider the space station at an orbit altitude of 410 km. Maximum allowable microgravity levels for various frequencies are given by Wetzel, ranging linearly from $1\mu g$ at $0.1Hz$ to $1000\mu g$ at $100Hz$[34]. Using these parameters in the proposed model, the resulting angular velocities range from 10^{-9} to 10^{-6}, while angular acceler-

ations range from 10^{-10} to $10^{-4}\frac{rad}{sec^2}$. From equation (2.65), the maximum acceleration due to rotations is then due to the angular acceleration term, the magnitude of which is approximated as:

$$|\dot{q}y'|$$

Even if the experiment is located at an altitude $|y'| = 10m$ higher than the center of mass of the station, the maximum acceleration generated due to rotation is only $10^{-3}m/sec^2$ or about $100\mu g$. This maximum acceleration generated by the rotational model is thus shown to be always less than the maximum allowable microgravity level.

This result shows that if the translational acceleration, or g-jitter, is modeled for certain values of amplitude and frequency, then the resulting accelerations predicted by the model of spacecraft motion are within acceptable levels. This idea is also confirmed by the analysis in the previous section, where the extra accelerations from the model are shown not to raise the order of magnitude of the summed sources.

Though the predicted angular accelerations do not exceed allowable levels, they are still in the range of what might be expected aboard a spacecraft. Knabe and Eilers suggest that angular accelerations due to vernier thruster firings reach levels of $10^{-4}\frac{rad}{sec^2}$[18], while Yuferev et al. consider maximum angular accelerations of $10^{-6}\frac{rad}{sec^2}$[38]. The model is thus expected to yield useful approximations for the values of the rotational as well as translational terms, especially when higher frequencies ranges are considered.

2.6 Simplification to known models

The momentum equation for fluid flow has been derived for multiple relative frames, with a model for spacecraft motion used to define the parameters of the resulting source terms. In an effort to demonstrate the validity of this analysis-and-model system describing microgravity flow, a comparison is made between this system and other microgravity models.

2.6.1 Sinusoidal g-jitter

The first comparison involves the simple model of a unidirectional acceleration that varies sinusoidally with time. Here, the momentum equation from (2.65) is shown to reduce to the simpler model when rotational motion parameters are set to zero.

It is assumed that the angle θ, representing spacecraft pitch, is fixed at 0 degrees. The equations for the components of the rotation tensor, 2.41, then shows that this tensor reduces as:

$$\alpha_{ij} = \delta_{ij} \tag{2.66}$$

where δ_{ij} is the Kroenecker delta.

If the angle representing spacecraft pitch is fixed, then

$$\frac{d\theta}{dt} = q = 0$$

and

$$\frac{d^2\theta}{dt^2} = \dot{q} = 0$$

The final reduction stops the spacecraft in its orbit by setting $Q = 0$ and $\frac{\partial \gamma}{\partial x_i} = 0$. This leaves the spacecraft floating in space with only a periodic translational motion.

When these reductions are applied to equation (2.65), the result is:

$$\begin{aligned} \frac{\partial \rho u_i}{\partial t} + \frac{\partial \rho u_i u_s}{\partial x_s} + \frac{\partial P}{\partial x_i} &= -\rho \delta_{it} \ddot{c}_t \\ &= \rho n g_0 \cos(\omega t) \end{aligned} \tag{2.67}$$

This reduced equation of motion describes the g-jitter models used by a number of researchers, such as Duval and Jacqmin[6], Kondos and Subramanian [19], and Matsumoto and Yoda[36].

2.6.2 One relative frame

As explained in section (1.1), other researchers do use relative coordinate frames to describe the microgravity environment. In most such cases, however, only one moving coordinate frame is used. For example, Yuferev et al. only consider the relative rotations of the orbiting spacecraft[38]. If only the spacecraft rotation is considered in equation (2.65), $Q = 0$, there is no gravity, $\dot{c}_i$ and $\ddot{c}_i = 0$ and $A_{ij} = \delta_{ij}$, leaving:

$$\rho \frac{Du_i}{Dt} + \frac{\partial P}{\partial x_i} = \rho q_3^2 (x_i + y_i') - 2\rho \epsilon_{ijk} q_j u_k - \rho \dot{q}_3 [\epsilon_{ipk} x_k + \epsilon_{ipk} y_k']$$

Again, the model with multiple moving frames is shown to reduce to the simpler model.

CHAPTER 3

Numerical Method

The theoretical microgravity model from chapter 2 predicts non-conservative motion. A numerical analysis is now initiated in order to both confirm this prediction and to study its characteristics. But before actual simulations can be run, a numerical approach must be determined and the equations must be written in a way that is conducive to this approach. The numerical code can then be used to investigate the characteristics of the fluid flow as described by a relative frames analysis combined with a model for spacecraft motion.

3.1 The Modified Clebsch/Weber Transformation

The first step to preparing the way for a numerical analysis is to decompose the momentum equation into its velocity components. This will be accomplished with a modified Clebsch/Weber transformation allowing the flow to be broken down into its rotational and irrotational parts. This will facilitate the numerical analysis, and will also give insight into the nature of the various source terms.

3.1.1 Set-up

To set up the momentum equation for the Clebsch/Weber transformation, the terms of equation (2.65) are expressed in terms of partial derivatives whenever possible. The Coriolis terms, $-2\epsilon_{ipk}(Q_p + q_p)u_k$, are conservative in two dimensional flow, and as such they can be expressed in terms of a scalar potential. This potential involves the stream function and works as follows:

$$-2\epsilon_{ipk}(Q_p + q_p)u_k = -2(Q+q)\left(\frac{\partial \psi}{\partial x_i}\right) \tag{3.1}$$

where $Q_p = Q_3 = Q$ and $q_p = q_3 = q$, and the stream function is defined by $\frac{\partial \psi}{\partial x_1} = -u_2$ and $\frac{\partial \psi}{\partial x_2} = u_1$.

Also, the angular acceleration term, $-\dot{q}_p\epsilon_{ipk}x_k$, is split into a potential term and a non-potential term:

$$-\dot{q}_p\epsilon_{ipk}(x_k + y'_k) = -\frac{\partial \dot{q}(x_1x_2 - x_1y'_2 + x_2y'_1)}{\partial x_i} + 2\dot{q}x_2\frac{\partial x_1}{\partial x_i} \tag{3.2}$$

where $\dot{q}_p = \dot{q}_3 = \dot{q}$. The second term on the right hand side represents the rotational part of the angular acceleration terms, and is the only non-conservative source generated by the 2 dimensional relative frames model.

Now, if we write

$$\begin{aligned} K \;=\; & \gamma + \left(\frac{Q^2}{2} + \frac{q^2}{2} + Qq\right)[(x_1 + y'_1)^2 + (x_2 + y'_2)^2] \\ & + x_jQ^2(\alpha_{jt}c_t) - 2(Q+q)\psi - 2x_jQ_p\alpha_{jt}\epsilon_{tpm}\dot{c}_m \\ & - x_j\alpha_{jt}\ddot{c}_t - \dot{q}(x_1x_2 - x_1y'_2 + x_2y'_1) \end{aligned} \tag{3.3}$$

then

$$\frac{\partial K}{\partial x_i} = \frac{\partial \gamma}{\partial x_i} + (Q^2 + q^2 + 2Qq)(x_i + y_i') + Q^2 \alpha_{it} c_t - 2(Q+q)\frac{\partial \psi}{\partial x_i}$$
$$-2Q_p \alpha_{it} \epsilon_{tpm} \dot{c}_m - \alpha_{it} \ddot{c}_t - \frac{\partial \dot{q}(x_1 x_2 - x_1 y_2' + x_2 y_1')}{\partial x_i} \tag{3.4}$$

Here, all potential sources are written using a gradient operator.

The momentum equation, (2.65), can now be written in a moving Cartesian coordinate system, x_i, as

$$\frac{Du_i}{Dt} = \frac{-1}{\rho}\frac{\partial P}{\partial x_i} + \frac{\partial K}{\partial x_i} + 2\dot{q}x_2\frac{\partial x_1}{\partial x_i} \tag{3.5}$$

Some assumptions and definitions are given now in preparation for the transformation to a velocity decomposition. First, from the conservation of mass (2.31) and the incompressible flow assumption described in section 2.4,

$$\frac{D\rho}{Dt} = 0 \tag{3.6}$$

and

$$\frac{\partial u_i}{\partial x_i} = 0 \tag{3.7}$$

Next, the material derivative is expanded as:

$$\frac{D}{Dt} = \frac{\partial}{\partial t} + u_i\frac{\partial}{\partial x_i} \tag{3.8}$$

Finally, the Lagrangian coordinates, X_i, are said to satisfy

$$\frac{DX_i}{Dt} = 0 \tag{3.9}$$

where the Cartesian/Lagrangian transformation matrix is defined as:

$$J = \frac{\partial x_i}{\partial X_j} \tag{3.10}$$

3.1.2 Transformation

Now the momentum equation is transformed into a velocity decomposition with separate rotational and irrotational parts. This Clebsch/Weber transformation is constructed in the following manner. When equation (3.5), is multiplied by the tranformation matrix J, the following equations result:

$$\frac{D}{Dt}\left(u_i\frac{\partial x_i}{\partial X_j}\right) = -\frac{1}{\rho}\frac{\partial P}{\partial X_j} + \frac{\partial}{\partial X_j}\left(K + \frac{u_i u_i}{2}\right) + 2\dot{q}x_2\frac{\partial x_1}{\partial X_j} \tag{3.11}$$

These equations can be integrated as follows

$$\begin{aligned}\int \frac{D}{Dt}\left(u_i\frac{\partial x_i}{\partial X_j}\right)dt &= -\int \frac{1}{\rho}\frac{\partial P}{\partial X_j}dt + \frac{\partial}{\partial X_j}\int\left(K + \frac{u_i u_i}{2}\right)dt \\ &\quad + \int 2\dot{q}x_2\frac{\partial x_1}{\partial X_j}dt \end{aligned} \tag{3.12}$$

where the Lagrangian description of the density field, equation (3.6), allows us to write

$$u_i\frac{\partial x_i}{\partial X_j} = -\frac{1}{\rho}\frac{\partial}{\partial X_j}\int P dt + \frac{\partial}{\partial X_j}\int\left(K + \frac{u_i u_i}{2}\right)dt + \int 2\dot{q}x_2\frac{\partial x_1}{\partial X_j}dt \tag{3.13}$$

We can define the transformations

$$\frac{D\phi}{Dt} = -P \tag{3.14}$$

$$\frac{D\beta}{Dt} = K + \frac{u_i u_i}{2} \tag{3.15}$$

$$\frac{DA_j}{Dt} = 2\dot{q}x_2\frac{\partial x_1}{\partial X_j} \tag{3.16}$$

such that equation (3.13) can be written

$$u_i\frac{\partial x_i}{\partial X_j} = \frac{1}{\rho}\frac{\partial \phi}{\partial X_j} + \frac{\partial \beta}{\partial X_j} + A_j \tag{3.17}$$

Equation (3.17) can now be multiplied by the inverse of matrix J to produce the velocity decomposition:

$$u_i = \frac{1}{\rho}\frac{\partial \phi}{\partial x_i} + \frac{\partial \beta}{\partial x_i} + \frac{\partial X_j}{\partial x_i} A_j \tag{3.18}$$

The inverse of the matrix J (i.e.$\frac{\partial X_j}{\partial x_i}$) can be found from equation (3.9). Furthermore, equation (3.16) can be expressed in terms of the components of $\frac{\partial X_j}{\partial x_i}$ by the following:

$$\frac{\partial x_i}{\partial X_j} = \begin{bmatrix} \frac{\partial x_1}{\partial X_1} & \frac{\partial x_1}{\partial X_2} \\ \frac{\partial x_2}{\partial X_1} & \frac{\partial x_2}{\partial X_2} \end{bmatrix} \tag{3.19}$$

$$= \left[\frac{\partial X_j}{\partial x_i}\right]^{-1} = \frac{1}{M}\begin{bmatrix} \frac{\partial X_2}{\partial x_2} & -\frac{\partial X_1}{\partial x_2} \\ -\frac{\partial X_2}{\partial x_1} & \frac{\partial X_1}{\partial x_1} \end{bmatrix} \tag{3.20}$$

where

$$M = \frac{\partial X_2}{\partial x_2}\frac{\partial X_1}{\partial x_1} - \frac{\partial X_2}{\partial x_1}\frac{\partial X_1}{\partial x_2} \tag{3.21}$$

Equation (3.16) can now be expressed as

$$\frac{DA_1}{Dt} = \frac{2\dot{q}x_2}{M}\left(\frac{\partial X_2}{\partial x_2}\right) \tag{3.22}$$

and

$$\frac{DA_2}{Dt} = \frac{2\dot{q}x_2}{M}\left(-\frac{\partial X_1}{\partial x_2}\right) \tag{3.23}$$

3.2 Solution outline

The steps required to solve the flow given by the velocity decomposition are now described. The ensuing numerical simulations will then compare the

effects of the various source terms in the velocity decomposition.

The solution steps are explained in the following:

· equations are written out in terms of their directional components

· relations required to solve for each term in the equations are specified

· equations are non-dimensionalized

· transformations into generalized coordinates are effectuated

· an UNO2 convecting scheme is used to solve hyperbolic equations

· elliptic equations are solved with LU factorization and a multigrid scheme

· initial and boundary conditions are determined.

These mark the steps required to solve for the variables in the velocity decomposition, thus defining the flow. The details and difficulties of each of these steps are explanationed in the remainder of this chapter.

3.3 Directional components and equations to be solved

In terms of writing a code to solve for the flow, the tensor notation used in previous sections can be at times difficult to interpret. In order to prepare for the coding, the equations are now restated in terms of cartesian directional components. The relations necessary to solve each of the terms given by the directional component equations are then explained.

Now that the momentum equation (2.65) and the velocity decomposition (3.18) have been expressed entirely in terms of the experiment's moving

coordinate frame (the x_i-frame), all of the following equations will also be expressed in this frame. This being the case, the variable 'x' will be used for 'x_1' and 'y' will be used for 'x_2'. Similarly, X_1 and X_2 will be replaced with X and Y. The constants y_1' and y_2' will be replaced with λ_1 and λ_2, and u_1 and u_2 are labelled as u and v respectively.

The velocity decomposition from equation (3.18) is written in terms of its cartesian components:

$$u = \frac{1}{\rho}\frac{\partial \phi}{\partial x} + \frac{\partial \beta}{\partial x} + \frac{\partial X}{\partial x}A_1 + \frac{\partial Y}{\partial x}A_2 \tag{3.24}$$

$$v = \frac{1}{\rho}\frac{\partial \phi}{\partial y} + \frac{\partial \beta}{\partial y} + \frac{\partial X}{\partial y}A_1 + \frac{\partial Y}{\partial y}A_2 \tag{3.25}$$

The first variable considered for solution is the density, ρ. From conservation of mass in incompressible flow, equation (2.52), the density can simply be convected with:

$$\frac{D\rho}{Dt} = 0 \tag{3.26}$$

Equation (3.15) from the Clebsch/Weber transformation allows the β potential to be solved with:

$$\begin{aligned}\frac{D\beta}{Dt} = &\left\{\frac{M_E G}{[(\alpha_{11}(\lambda_1+x)+\alpha_{21}(\lambda_2+y)+c_1)^2+(\alpha_{12}(\lambda_1+x)+\alpha_{22}(\lambda_2+y))^2]^{\frac{1}{2}}}\right\} \\ &+\left(\frac{Q^2}{2}+\frac{q^2}{2}+Qq\right)[(x+\lambda_1)^2+(y+\lambda_2)^2]-2\psi(Q+q) \\ &-\dot{q}(xy-x\lambda_2+y\lambda_1)+xQ^2\alpha_{11}c_1+yQ^2\alpha_{21}c_1 \\ &+2xQ(-\alpha_{12}\dot{c}_1)+2yQ(-\alpha_{22}\dot{c}_1)-x(\alpha_{11}\ddot{c}_1)-y(\alpha_{21}\ddot{c}_1) \\ &+\frac{uu+vv}{2}\end{aligned} \tag{3.27}$$

where:

$$
\begin{aligned}
c_2 &= \dot{c}_2 = \ddot{c}_2 = 0 \\
c_1 &= c' + \frac{ng_0}{\omega^2}\cos(\omega t) \\
c' &= \text{Avg Earth Radius+Avg Spacecraft Altitude} = 6.85 \times 10^6 \\
\dot{c}_1 &= -\frac{ng_0}{\omega}\sin(\omega t) \\
\ddot{c}_1 &= -ng_0\cos(\omega t) \\
q_3 &= -\frac{ng_0\cos^2(\theta)\cos(\omega t)}{Qc'} \\
\dot{q} &= \frac{-ng_0[q\sin(2\theta)\cos(\omega t) - \omega\cos^2(\theta)\sin(\omega t)]}{Qc'}
\end{aligned}
$$

and also, as descibed in equation (2.41),

$$
\begin{aligned}
\alpha_{11} &= \cos(\theta) \\
\alpha_{12} &= \sin(\theta) \\
\alpha_{21} &= -\sin(\theta) \\
\alpha_{22} &= \cos(\theta)
\end{aligned}
$$

with

$$\theta = \arctan\left(\frac{ng_0}{\omega Qc'}\sin(\omega t)\right)$$

from equation (2.62). These relations are part of the model for spacecraft motion from section 2.5.1.

The description of the Coriolis term in the β potential involves the use of the stream function, ψ. To obtain this function, its relation with vorticity is used:

$$vorticity = \frac{\partial^2\psi}{\partial y^2} + \frac{\partial^2\psi}{\partial x^2} \tag{3.28}$$

and the vorticity is calculated from the previous timestep's velocity by:

$$vorticity = \frac{\partial v}{\partial x} - \frac{\partial u}{\partial y} \tag{3.29}$$

All other terms in the β potential are obtained from the model derived in section 2.5.1. In other words, if the average orbit altitude c' is known, the values for all of the source terms in the potential are found by setting an amplitude level n and a frequency ω.

The Clebsch/Weber transformation also allows the A_i terms to be solved using equation (3.16):

$$\frac{DA_1}{Dt} = \frac{2\dot{q}y}{\frac{\partial Y}{\partial y}\frac{\partial X}{\partial x} - \frac{\partial Y}{\partial x}\frac{\partial X}{\partial y}} \left(\frac{\partial Y}{\partial y}\right) \tag{3.30}$$

and

$$\frac{DA_2}{Dt} = \frac{2\dot{q}y}{\frac{\partial Y}{\partial y}\frac{\partial X}{\partial x} - \frac{\partial Y}{\partial x}\frac{\partial X}{\partial y}} \left(-\frac{\partial X}{\partial y}\right) \tag{3.31}$$

To solve the convection equation for the material coordinates, $\frac{\partial X_j}{\partial x_i}$, the definition from equation (3.9) will be required, rewritten as:

$$\frac{DX}{Dt} = 0 \tag{3.32}$$

and

$$\frac{DY}{Dt} = 0 \tag{3.33}$$

In the actual numerical code, the source terms from equation (4.5) are given the following labels:

$$S1 = \frac{M_E G}{[(\alpha_{11}(\lambda_1+x)+\alpha_{21}(\lambda_2+y) + c_1)^2 + (\alpha_{12}(\lambda_1+x)+\alpha_{22}(\lambda_2+y))^2]^{\frac{1}{2}}}$$

$$
\begin{aligned}
S2 &= \frac{Q^2}{2}[(x+\lambda_1)^2+(y+\lambda_2)^2] \\
S3 &= \frac{q^2}{2}[(x+\lambda_1)^2+(y+\lambda_2)^2] \\
S4 &= Qq[(x+\lambda_1)^2+(y+\lambda_2)^2] \\
S5 &= -2\psi(Q+q) \\
S6 &= -\dot{q}(xy+x\lambda_2+y\lambda_1) \\
S7 &= xQ^2\alpha_{11}c_1 \\
S8 &= yQ^2\alpha_{21}c_1 \\
S9 &= 2xQ(-\alpha_{12}\dot{c}_1) \\
S10 &= 2yQ(-\alpha_{22}\dot{c}_1) \\
S11 &= -x(\alpha_{11}\ddot{c}_1) \\
S12 &= -y(\alpha_{21}\ddot{c}_1)
\end{aligned}
$$

The remaining term to be solved is ϕ. Equation (3.14) could be used for this purpose, but it would be difficult to decide on what boundary conditions would be appropriate for this case. A better way is to use the continuity equation (3.7), since all other terms in the velocity decomposition will have been determined. This means that the continuity equation can be written as:

$$
\begin{aligned}
\frac{\partial u}{\partial x}+\frac{\partial v}{\partial y} &= \frac{\partial}{\partial x}\left(\frac{1}{\rho}\frac{\partial \phi}{\partial x}+\frac{\partial \beta}{\partial x}+\frac{\partial X}{\partial x}A_1+\frac{\partial Y}{\partial x}A_2\right) \\
&\quad +\frac{\partial}{\partial y}\left(\frac{1}{\rho}\frac{\partial \phi}{\partial y}+\frac{\partial \beta}{\partial y}+\frac{\partial X}{\partial y}A_1+\frac{\partial Y}{\partial y}A_2\right)=0 \qquad (3.34)
\end{aligned}
$$

By solving for ϕ in this way, the satisfaction of continuity is assured.

3.4 Dimensional analysis

The microgravity environment is characterized by extremely low accelerations. In order to obtain values for these accelerations, the model proposed by Duval and Jacqmin is employed, where translational accelerations range from $10^{-5}g_0$ to $10^{-3}g_0$ in amplitude and from 0.1 to 10 Hz in frequency[6]. If the middle values, $10^{-4}g_0$ and 1.0 Hz, are used in the model proposed in section 2.5.1, the resulting angular velocity and acceleration are of the order $10^{-5}\frac{rad}{s}$ and $10^{-7}\frac{rad}{s^2}$. These values fall within the range of what is to be expected aboard an orbiting spacecraft[38], as explained in section 2.5.2 and 2.5.3.

With such small accelerations being considered, the resulting fluid velocities will also be small, often in the order of $10^{-6}m/s$. In order to avoid excessive truncation error in the numerical calculations, all of the equations are non-dimensinalized to this velocity of $u_{ref} = 1\mu m/s$. The non-dimensional length of $x_{ref} = 10cm$ will also be used for non-dimensionalization, as this represents domain height that will be used. The remaining unit to non-dimensionalize is mass, but since the orders of magnitude will be appropriately adjusted with u_{ref}, an arbitrary ρ_{ref} is used.

The variables in equations (3.24) to (3.31) are thus non-dimensionalized as follows:

$$x^* = \frac{x}{x_{ref}}; \quad y^* = \frac{y}{x_{ref}}; \quad \lambda_1^* = \frac{\lambda_1}{x_{ref}}; \quad \lambda_2^* = \frac{\lambda_2}{x_{ref}};$$

$$c'^* = \frac{c'}{x_{ref}}; \quad X^* = \frac{X}{x_{ref}}; \quad Y^* = \frac{Y}{x_{ref}}; \quad \rho^* = \frac{\rho}{\rho_{ref}};$$
$$t^* = \frac{tu_{ref}}{x_{ref}}; \quad u^* = \frac{u}{u_{ref}}; \quad v^* = \frac{v}{u_{ref}}; \quad \dot{c}^* = \frac{\dot{c}}{u_{ref}};$$
$$g_0^* = \frac{g_0 x_{ref}}{u_{ref}^2}; \quad \ddot{c}^* = \frac{\ddot{c}x_{ref}}{u_{ref}^2}; \quad (M_E G)^* = \frac{M_E G}{x_{ref}u_{ref}^2};$$
$$Q^* = \frac{Qx_{ref}}{u_{ref}}; \quad q^* = \frac{qx_{ref}}{u_{ref}}; \quad \dot{q}^* = \frac{\dot{q}x_{ref}^2}{u_{ref}^2}; \quad \psi^* = \frac{\psi}{x_{ref}u_{ref}};$$

where * represents a non-dimensional quantity.

The equations to be solved are now re-stated in terms of non-dimensional variables:

$$u^* = \frac{1}{\rho^*}\frac{\partial \phi^*}{\partial x^*} + \frac{\partial \beta^*}{\partial x^*} + \frac{\partial X^*}{\partial x^*}A_1^* + \frac{\partial Y^*}{\partial x^*}A_2^* \tag{3.35}$$

$$v^* = \frac{1}{\rho^*}\frac{\partial \phi^*}{\partial y^*} + \frac{\partial \beta^*}{\partial y^*} + \frac{\partial X^*}{\partial y^*}A_1^* + \frac{\partial Y^*}{\partial y^*}A_2^* \tag{3.36}$$

where

$$\frac{D\beta^*}{Dt^*} = \frac{(M_E G)^*}{[(\alpha_{11}(\lambda_1^*+x^*)+\alpha_{21}(\lambda_2^*+y^*)+c_1^*)^2 + (\alpha_{12}(\lambda_1^*+x^*)+\alpha_{22}(\lambda_2^*+y^*))^2]^{\frac{1}{2}}}$$
$$+\left(\frac{Q^{*2}}{2} + \frac{q^{*2}}{2} + Q^*q^*\right)[(x^*+\lambda_1^*)^2 + (y+\lambda_2^*)^2] - 2\psi^*(Q^*+q^*)$$
$$-\dot{q}^*(x^*y^* - x^*\lambda_2^* + y^*\lambda_1^*) + x^*Q^{*2}\alpha_{11}c_1^* + y^*Q^{*2}\alpha_{21}c_1^*$$
$$+2x^*Q^*(-\alpha_{12}\dot{c}_1^*) + 2y^*Q^*(-\alpha_{22}\dot{c}_1^*) - x^*(\alpha_{11}\ddot{c}_1^*) - y^*(\alpha_{21}\ddot{c}_1^*)$$
$$+\frac{u^*u^* + v^*v^*}{2} \tag{3.37}$$

$$\frac{DA_1^*}{Dt^*} = \frac{2\dot{q}^*y^*}{\frac{\partial Y^*}{\partial y^*}\frac{\partial X^*}{\partial x^*} - \frac{\partial Y^*}{\partial x^*}\frac{\partial X^*}{\partial y^*}}\left(\frac{\partial Y^*}{\partial y^*}\right) \tag{3.38}$$

$$\frac{DA_2^*}{Dt^*} = \frac{2\dot{q}^*y^*}{\frac{\partial Y^*}{\partial y^*}\frac{\partial X^*}{\partial x^*} - \frac{\partial Y^*}{\partial x^*}\frac{\partial X^*}{\partial y^*}}\left(-\frac{\partial X^*}{\partial y^*}\right) \tag{3.39}$$

$$\frac{DX^*}{Dt^*} = 0 \tag{3.40}$$

$$\frac{DY^*}{Dt^*} = 0 \tag{3.41}$$

$$\frac{D\rho^*}{Dt^*} = 0 \tag{3.42}$$

The continuity equation is simply:

$$\frac{\partial u^*}{\partial x^*} + \frac{\partial v^*}{\partial y^*} = 0 \tag{3.43}$$

The non-dimensional total derivatives expand as:

$$\frac{\partial}{\partial t^*} + u^* \frac{\partial}{\partial x^*} + v^* \frac{\partial}{\partial y^*} \tag{3.44}$$

These non-dimensional equations do not require any non-dimensional parameters. It is assumed that all variables are non-dimensional in all proceeding explanations, and as such the superscript * will not be used.

3.5 Hyperbolic equations

One of the principal advantages to using the Clebsch/Weber velocity decomposition is that most of the variables are solved with convection equations. Solution methods to these equations are accurate and computationally inexpensive. The convection equations (3.37) through (3.42) are solved with a midpoint rule time advancement and a uniformly second-order accurate scheme (UNO2), developed by Harten and Osher [10]. A description of this method is given by Yokota [37] and is reconstructed here.

To explain this method, the sample variable W is convected. The variables $F = Wu$, $G = Wv$, and H are also defined, where H represents any source terms. The convection equation is now written as:

$$\frac{\partial W}{\partial t} + \frac{\partial F}{\partial x} + \frac{\partial G}{\partial y} = H$$

This equation is time-advanced with the midpoint rule:

$$W_{i,j}^{n+1} = W_{i,j}^{n} - \Delta t \left(\frac{F_{i+\frac{1}{2},j}^{n+\frac{1}{2}} - F_{i-\frac{1}{2},j}^{n+\frac{1}{2}}}{\Delta x} + \frac{G_{i,j+\frac{1}{2}}^{n+\frac{1}{2}} - F_{i,j-\frac{1}{2}}^{n+\frac{1}{2}}}{\Delta y} + H^{n} \right) \quad (3.45)$$

where the subscripts i and j represent the particular cell being considered, and the superscript n represents the time level. The variables at the half timelevels are calculated with the UNO2 scheme. For example, in the one-dimensional case,

$$W = W_i + S_i^x (x - x_i) \quad (3.46)$$

The variable S_i^x represents the slope over each finite volume. These slopes are found with:

$$S_i^x = \frac{\text{median}\left(0, W_{i+\frac{1}{2}}^{c} - W_i, W_i - W_{i-\frac{1}{2}}^{c}\right)}{\frac{\Delta x}{2}} \quad (3.47)$$

where $W_{i+\frac{1}{2}}^{c}$ comes from

$$W_{i+\frac{1}{2}}^{c} = 0.5(W_i + W_{i+1}) - 0.25 D_{i+\frac{1}{2}} \quad (3.48)$$

and

$$D_{i+\frac{1}{2}} = \text{minmod}(D_i, D_{i+1}) \quad (3.49)$$

$$D_i = W_{i+1} - 2W_i + W_{i-1} \quad (3.50)$$

$$\text{minmod}(a, b) = \text{sign}(a)\max[0, \text{sign}(ab)\min(|a|, |b|)] \quad (3.51)$$

And finally, to get data at the half time level,

$$W^{n+\frac{1}{2}}_{i+\frac{1}{2},j} = W^n_{i,j} + S^x_{i,j}\frac{\Delta x}{2}\left(1 - \frac{u_{i+\frac{1}{2},j}\Delta t}{\Delta x}\right) - S^y_{i,j}\frac{v_{i+\frac{1}{2},j}\Delta t}{2} \tag{3.52}$$

This assumes that the convection speeds are positive.

3.6 Elliptic equation

There are two elliptic equations that need to be solved in order to resolve the flow. The first is the equation for vorticity, equation (3.28), which yields the stream function. The second is the continuity equation, (3.34), used to obtain the ϕ potential. Both equations are solved with the same algorithm, which makes use of approximately factored LU scheme to yield the variables in question. This technique, as described by Reid[25], will be demonstrated here using the continuity equation.

The continuity equation (3.34), is restated here with the velocity decomposition expression from equations (3.24) and (3.25) used for the u and v velocities:

$$\begin{aligned}\frac{\partial u}{\partial x} + \frac{\partial v}{\partial y} &= \frac{\partial}{\partial x}\left(\frac{1}{\rho}\frac{\partial \phi}{\partial x} + \frac{\partial \beta}{\partial x} + \frac{\partial X}{\partial x}A_1 + \frac{\partial Y}{\partial x}A_2\right) \\ &\quad + \frac{\partial}{\partial y}\left(\frac{1}{\rho}\frac{\partial \phi}{\partial y} + \frac{\partial \beta}{\partial y} + \frac{\partial X}{\partial y}A_1 + \frac{\partial Y}{\partial y}A_2\right) = 0\end{aligned} \tag{3.53}$$

The ϕ potential is constructed such that the continuity equation is satisfied at each timestep.

To solve this numerically, the equation is iterated at each timestep to a steady state. A non-physical pseudotime t^* is incorporated for this iteration

process. Equation (3.53) is thus rearranged to give:

$$\begin{aligned}\frac{\partial \phi}{\partial t^*} &= \frac{\partial}{\partial x}\left(\frac{1}{\rho}\frac{\partial \phi}{\partial x}\right) + \frac{\partial}{\partial y}\left(\frac{1}{\rho}\frac{\partial \phi}{\partial y}\right) \\ &+ \frac{\partial}{\partial x}\left(\frac{\partial \beta}{\partial x} + \frac{\partial X}{\partial x}A_1 + \frac{\partial Y}{\partial x}A_2\right) \\ &+ \frac{\partial}{\partial y}\left(\frac{\partial \beta}{\partial y} + \frac{\partial X}{\partial y}A_1 + \frac{\partial Y}{\partial y}A_2\right) \end{aligned} \tag{3.54}$$

where t^* is the pseudotime.

An approximately factored LU scheme is used to solve equation (3.54). To produce this scheme, consider a Taylor series expansion of the ϕ potential:

$$\phi^{k+1} = \phi^k + \frac{\partial \phi}{\partial t^*}^k \Delta t^* + O(\Delta t^{*2}) \tag{3.55}$$

Here, the superscript 'k' refers to the pseudotime level.

The series expansion can be re-written in terms of an implicit parameter μ:

$$\phi^{k+1} = \phi^k + \Delta t^* \left[(1-\mu)\frac{\partial \phi}{\partial t^*}^k + \mu \frac{\partial \phi}{\partial t^*}^k\right] + O(\Delta t^{*2}) \tag{3.56}$$

Equation (3.55) can then be used to obtain:

$$\phi^{k+1} = \phi^k + \Delta t^* \left[(1-\mu)\frac{\partial \phi}{\partial t^*}^k + \mu \frac{\partial \phi}{\partial t^*}^{k+1}\right] + O(\Delta t^{*2}) \tag{3.57}$$

with ϕ being constant for the pseudotime.

Defining $\Delta\phi = \phi^{k+1} - \phi^k$ and rearranging gives:

$$\Delta\phi - \mu\Delta t^* \left[\frac{\partial \phi}{\partial t^*}^{k+1} - \frac{\partial \phi}{\partial t^*}^k\right] = \Delta t^* \frac{\partial \phi}{\partial t^*}^k \tag{3.58}$$

The continuity equation from (3.54) can now be used for the derivative on the right hand side of equation (3.58). The spatial partial derivatives from making up the right hand side of (3.54) are abbreviated as the residual, Res, leaving equation (3.58) as:

$$\Delta\phi - \mu\Delta t^* \left[\frac{\partial \phi}{\partial t^*}^{k+1} - \frac{\partial \phi}{\partial t^*}^{k} \right] = \Delta t^* Res^k \tag{3.59}$$

This equation can be rearranged as:

$$\left\{ 1 - \mu\Delta t^* \left[\frac{\partial}{\partial x}\left(\frac{1}{\rho}\frac{\partial}{\partial x} \right) + \frac{\partial}{\partial y}\left(\frac{1}{\rho}\frac{\partial}{\partial y} \right) \right] \right\} \Delta\phi = \Delta t^* Res^k \tag{3.60}$$

Writing the partial derivatives in delta form gives:

$$\left\{ 1 - \mu\Delta t^* \left[\delta_x \frac{1}{\rho}\delta_x + \delta_y \frac{1}{\rho}\delta_y \right] \right\} \Delta\phi = \Delta t^* Res^k \tag{3.61}$$

Equation (3.61) can be written as an approximate factorization in operator form:

$$\begin{aligned} &\left\{ 1 - \mu\Delta t^* \left[\left(\frac{1}{\rho} \right)_{i+\frac{1}{2}} \frac{\delta_y^+}{\Delta y^2} + \left(\frac{1}{\rho} \right)_{j+\frac{1}{2}} \frac{\delta_x^+}{\Delta x^2} \right] \right\} \\ &\cdot \left\{ 1 + \mu\Delta t^* \left[\left(\frac{1}{\rho} \right)_{i-\frac{1}{2}} \frac{\delta_y^-}{\Delta y^2} + \left(\frac{1}{\rho} \right)_{j-\frac{1}{2}} \frac{\delta_x^-}{\Delta x^2} \right] \right\} \Delta\phi \\ &= \zeta\Delta t^* Res^k \end{aligned} \tag{3.62}$$

where ζ is a relaxation factor. The delta operators are defined as:

$$\delta_x^+ \Delta\phi = \frac{\Delta\phi_{i+1j} - \Delta\phi_{ij}}{\Delta x} \tag{3.63}$$

$$\delta_x^- \Delta\phi = \frac{\Delta\phi_{ij} - \Delta\phi_{i-1j}}{\Delta x} \tag{3.64}$$

$$\delta_y^+ \Delta\phi = \frac{\Delta\phi_{ij+1} - \Delta\phi_{ij}}{\Delta y} \tag{3.65}$$

$$\delta_y^- \Delta\phi = \frac{\Delta\phi_{ij} - \Delta\phi_{ij-1}}{\Delta y} \tag{3.66}$$

The solution involves 2 steps:

$$\begin{aligned} (1) \quad & \left\{1 + \mu\Delta t^* \left[\left(\frac{1}{\rho}\right)_{i-\frac{1}{2}} \frac{\delta_y^-}{\Delta y^2} + \left(\frac{1}{\rho}\right)_{j-\frac{1}{2}} \frac{\delta_x^-}{\Delta x^2}\right]\right\} \Delta\phi' &= \zeta\Delta t^* Res^k \\ (2) \quad & \left\{1 - \mu\Delta t^* \left[\left(\frac{1}{\rho}\right)_{i+\frac{1}{2}} \frac{\delta_y^+}{\Delta y^2} + \left(\frac{1}{\rho}\right)_{j+\frac{1}{2}} \frac{\delta_x^+}{\Delta x^2}\right]\right\} \Delta\phi &= \Delta\phi' \end{aligned} \tag{3.67}$$

Steps (1) and (2) are solved explicitly in a step by step manner to give a steady state solution at each physical timestep.

Since this equation is being run to a steady state, the consistency of the factorization given by equation (3.62) can be verified. For example, consider the one-dimensional case with uniform density. Using this simplification and re-factoring the equation gives:

$$\begin{aligned} \left(1 - \frac{\mu\Delta t^*}{\rho}\frac{\delta_x^+}{\Delta x^2}\right)\left(1 + \frac{\mu\Delta t^*}{\rho}\frac{\delta_x^-}{\Delta x^2}\right)\Delta\phi &= \zeta\Delta t^* Res^k \\ \left(1 + \frac{\mu\Delta t^*}{\rho}\frac{\delta_x^-}{\Delta x^2} - \frac{\mu\Delta t^*}{\rho}\frac{\delta_x^+}{\Delta x^2} - \frac{\mu^2\Delta t^{*2}}{\rho}\frac{\delta_x^+}{\Delta x^2}\frac{\delta_x^-}{\Delta x^2}\right)\Delta\phi &= \\ \Delta\phi + \frac{\mu\Delta t^*}{\rho}\frac{\delta\delta\Delta\phi}{\Delta x^2} - \frac{\mu^2\Delta t^{*2}}{\rho}\frac{\delta_x^+}{\Delta x^2}\frac{\delta_x^-}{\Delta x^2}\Delta\phi &= \end{aligned} \tag{3.68}$$

If the numerical scheme converges $\Delta\phi$, as well as Res, goes to zero at each timestep and the third term on the left of equation (3.68) will not add error due to inconsistency.

3.6.1 Stability analysis

A numerical scheme is considered stable if the error remains bounded as Δt goes to zero for a fixed t, and as t goes to infinity for a fixed Δt. To get an indication of the stability of the LU scheme, a von Neumann Stability Analysis is performed on a simplified equation as described by Yokota [37]. This does not guarantee the stability of the scheme for the vorticity or continuity equations, but it does give some idea of what the stability characteristics might be.

The simplified equation to which the stability analysis is performed is:

$$\frac{\partial^2 F}{\partial x^2} = 0 \tag{3.69}$$

the approximate factorization of which is:

$$(1 - \mu C\delta_x^+) \cdot (1 + \mu C\delta_x^-)\Delta F_j = C\zeta\delta_{xx}F_j \tag{3.70}$$

where $C = \frac{\Delta t^*}{\Delta x^2}$ represents the fourier number and ζ is again the relaxation parameter.

A fourier decomposition of the solution potential is:

$$F_j^k = G^k e^{i\beta x_j} \tag{3.71}$$

where G^k represents the growth factor,

$$G^k = \frac{F_j^{k+1}}{F_j^k} \tag{3.72}$$

The operator form of the approximate factorization from equation (3.70) can be written here for the simplified elliptic equation as:

$$\begin{aligned} [1 - \mu C(e^{i\beta x} - 1)] \quad \cdot \quad & [1 + \mu C(1 - e^{-i\beta x})]\Delta F^k \\ = \quad & \zeta C(e^{i\beta x} + e^{-i\beta x})F_j \end{aligned} \tag{3.73}$$

Using $\Delta F = F^{k+1} - F^k$, this equation can be re-expressed in terms of the definition of the growth factor from equation (3.72):

$$G^k = \frac{\zeta C(e^{i\beta x} + e^{-i\beta x}) + [1 - \mu C(e^{i\beta x} - 1)] \cdot [1 + \mu C(1 - e^{-i\beta x})]}{[1 - \mu C(e^{i\beta x} - 1)] \cdot [1 + \mu C(1 - e^{-i\beta x})]}$$

Using the relations:

$$\cos(x) = \frac{1}{2}(e^{ix} + e^{-ix})$$
$$\sin^2(\frac{x}{2}) = \frac{1}{2}(1 - cos(x))$$

the growth factor can be written as:

$$G = \frac{1 - 4C[\zeta - \mu(1 + \mu C)]sin^2(\beta \Delta x/2)}{1 + 4\mu C(1 + \mu C)sin^2(\beta \Delta x/2)} \tag{3.74}$$

The growth factor is plotted in figure (3.1) for $\mu = 0.5$, $C = 5.3$ and $\zeta = 1.9$, matching the parameters suggested by Yokota to damp high frequency errors[37].

3.7 Transformation to generalized coordinates

All differencing is performed on a computational grid, where the cell sizes are $\Delta x = \Delta y = 1$. This compututional grid then only allows rectangular shapes with no variation in cell sizes. To allow for different domain shapes and cell sizes within the domain, any relation must be transformed from the physical domain of cartesian coordinates to the computational domain of generalized coordinates. These transformations are shown in this section for a standard convection equation in 2 dimensions with source terms.

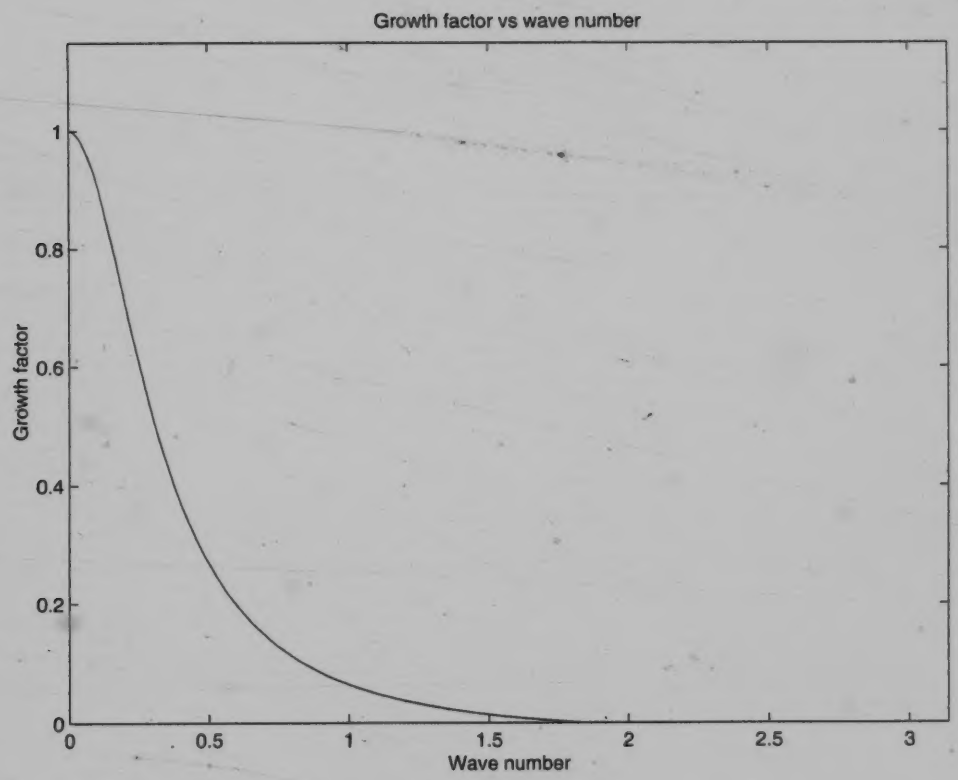

Figure 3.1: Growth factor for LU scheme

The standard equation used to represent the transformation is:

$$\frac{\partial f}{\partial t} + \frac{\partial g}{\partial x} + \frac{\partial h}{\partial y} = s \tag{3.75}$$

where $g = uf$, $h = vf$, and $\vec{s}$ represents source terms.

The generalized coordinates representing the computational domain are:

$$\xi = \xi(x, y, z) \qquad \eta = \eta(x, y, z) \tag{3.76}$$

To relate the generalized and physical coordinates, the Jacobian matrix

of the transformation is defined:

$$J = \begin{bmatrix} x_\xi & x_\eta \\ y_\xi & y_\eta \end{bmatrix} \tag{3.77}$$

with the inverse:

$$J^{-1} = \begin{bmatrix} \xi_x & \xi_y \\ \eta_x & \eta_y \end{bmatrix} = \frac{1}{D} \begin{bmatrix} y_\eta & -x_\eta \\ -y_\xi & x_\xi \end{bmatrix} \tag{3.78}$$

and D is the determinant of J.

Applying the chain rule transformation to equation (3.75) gives:

$$\begin{aligned} \frac{\partial f}{\partial t} &+ \frac{\partial g}{\partial \xi}\frac{\partial \xi}{\partial x} + \frac{\partial g}{\partial \eta}\frac{\partial \eta}{\partial x} \\ &+ \frac{\partial h}{\partial \xi}\frac{\partial \xi}{\partial y} + \frac{\partial h}{\partial \eta}\frac{\partial \eta}{\partial y} = s \end{aligned} \tag{3.79}$$

Each term in this equation is multiplied by the time-independent determinant D:

$$\begin{aligned} \frac{\partial (fD)}{\partial t} &+ \frac{\partial g}{\partial \xi}\frac{\partial \xi}{\partial x}D + \frac{\partial g}{\partial \eta}\frac{\partial \eta}{\partial x}D \\ &+ \frac{\partial h}{\partial \xi}\frac{\partial \xi}{\partial y}D + \frac{\partial h}{\partial \eta}\frac{\partial \eta}{\partial y}D = sD \end{aligned} \tag{3.80}$$

By using the definition of J^{-1} from equation (3.78), equation (3.80) can be rewritten as:

$$\frac{\partial (fD)}{\partial t} + \frac{\partial g}{\partial \xi}(y_\eta) + \frac{\partial g}{\partial \eta}(-y_\xi) + \frac{\partial h}{\partial \xi}(-x_\eta) + \frac{\partial h}{\partial \eta}(x_\xi) = sD \tag{3.81}$$

The terms (y_η), $(-y_\xi)$, $(-x_\eta)$ and (x_ξ) from the inverse Jacobian can be moved inside the partial derivatives:

$$\begin{aligned} \frac{\partial (fD)}{\partial t} &+ \frac{\partial g(y_\eta)}{\partial \xi} + \frac{\partial g(-y_\xi)}{\partial \eta} + \frac{\partial h(-x_\eta)}{\partial \xi} + \frac{\partial h(x_\xi)}{\partial \eta} \\ &- g\frac{\partial (y_\eta)}{\partial \xi} - g\frac{\partial (-y_\xi)}{\partial \eta} - h\frac{\partial (-x_\eta)}{\partial \xi} - h\frac{\partial (x_\xi)}{\partial \eta} = sD \end{aligned} \tag{3.82}$$

Since the partial derivatives are commutative,

$$\begin{aligned} y_{\eta\xi} - y_{\xi\eta} &= 0 \\ x_{\eta\xi} - x_{\xi\eta} &= 0 \end{aligned} \tag{3.83}$$

This means that equation (6) can be written as:

$$\frac{\partial F}{\partial t} + \frac{\partial G}{\partial \xi} + \frac{\partial H}{\partial \eta} = S \tag{3.84}$$

where

$$F = fD$$

$$G = g(y_\eta) + h(-x_\eta)$$

$$H = g(-y_\xi) + h(x_\xi) \tag{3.85}$$

$$S = sD \tag{3.86}$$

3.8 Grids and timestep sizes

The test cases shown in chapter 4 make use of two different physical grids. The first grid, shown in figure (3.2), is simply a rectangular mesh with uniform 48×96 grid spacing. The uniform spacing ensures higher order accuracy of the interpolations and differencing. Most trials were performed on this grid.

Another grid, shown in figure (3.3), was initially used in this work. As the figure shows, this grid makes use of varying cell sizes in an effort to improve accuracy near a central density interface and near wall boundaries. It was found, however, that the use of varying cell sizes led to accuracy problems, so the packed meshes were not used.

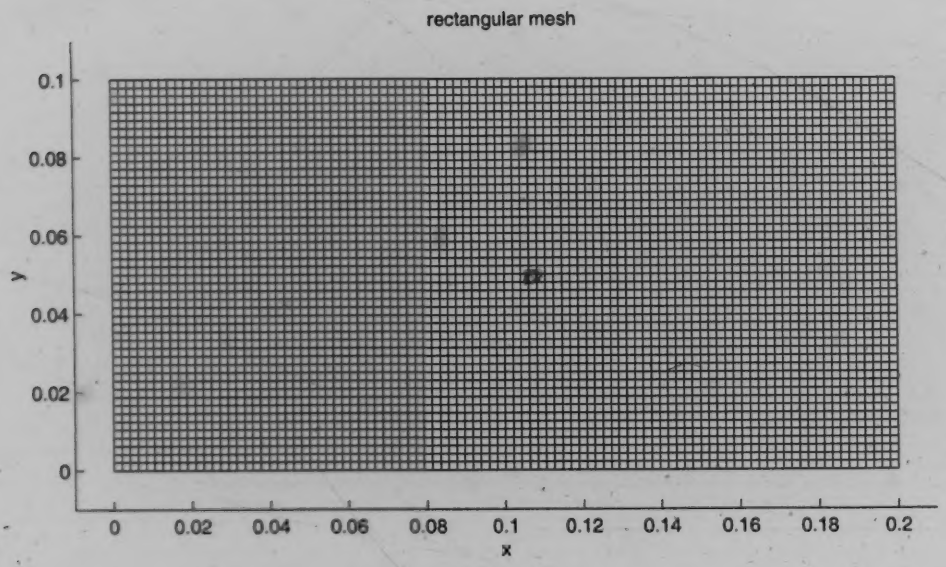

Figure 3.2: Rectangual grid with uniform cell sizes

In addition to the rectangular mesh, a circular mesh is also used. The transformation of this mesh to the computational domain is somewhat more difficult to visualize. The circular grid is shown in figure (3.4), where there are 48 equally spaced radial divisions and 48 equally spaced angular divisions. The method by which this grid is unwrapped to the rectangular-shaped computational domain is shown in figure (3.5). In this figure, the point AD at the center of the circular domain is unwrapped to create the bottom line of the rectangular computational domain. Line AB is unwrapped to form the left side, line CD becomes the right side, and the circumference BC unwraps to form the top boundary of the computational domain.

The accuracy of the code is influenced not only by the cell sizes, but of

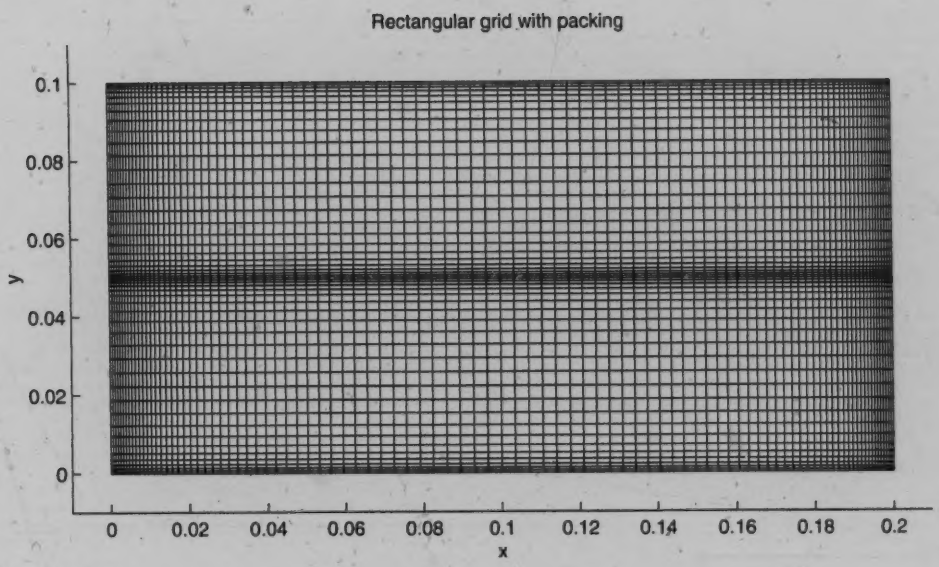

Figure 3.3: Rectangual grid with uniform cell sizes

course the timestep size. In order to determine a suitable timestep, the code is tested at different timesteps for the case periodic motion resulting from a uniform density flow. As will be shown in chapter 4, this case is when non-conservative source terms are applied in the absence of a density gradient.

To test the effect of timestep size, the motion in the fluid is compared at the same physical time for runs of differing timesteps. To quantify the motion in the fluid, changes in the material coordinates are used. A value for total displacement is found by subtracting the current material value from the initial value for every cell in the domain. The X and Y differences are squared, and the root of their sum is added for all cells to get a single value for any particular point in time. This value is then used as a measure by

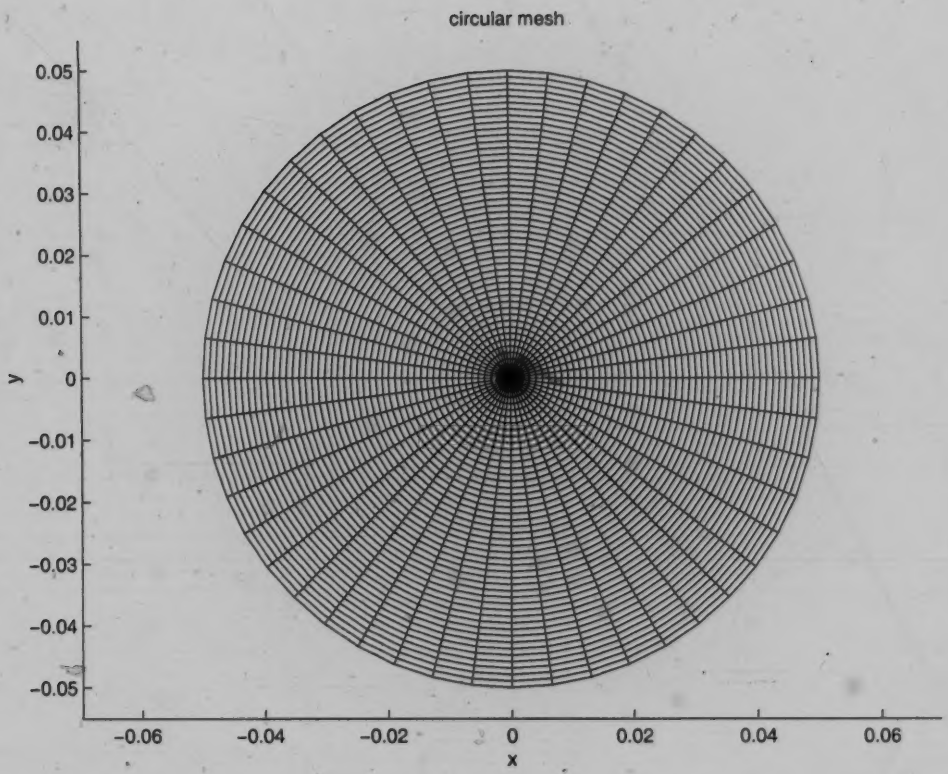

Figure 3.4: Circular grid

which to gauge the sensitivity of timestep. It is checked after 1 complete cycle for timestep values of 0.1×10^{-1}, 0.1×10^{-2}, and 0.1×10^{-3}. The results, summarized in table (3.8), show that there is only a $10^{-4}\%$ difference in total displacement values between the 0.1×10^{-2} and 0.1×10^{-3} timestep values. A timestep of 0.1×10^{-2} is used to maximize time advancement with an acceptable level of error.

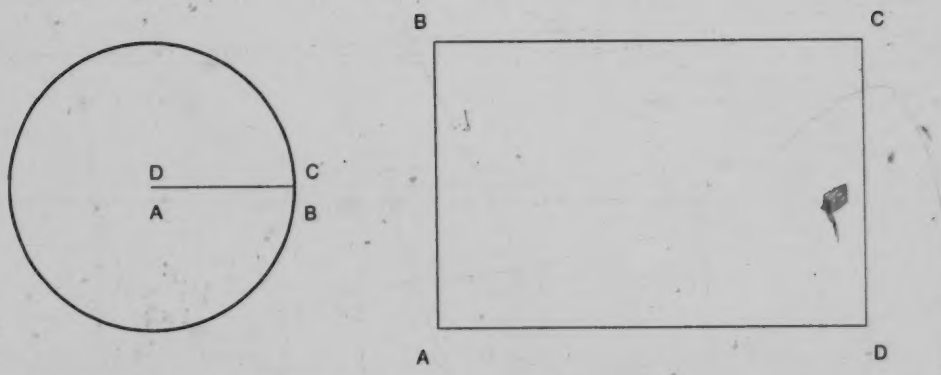

Figure 3.5: Unwrapping of circular domain to form the computational domain

3.9 Differencing techniques

In order to calculate partial spatial derivatives, some form of differencing must be used. For example, the residual given by equation (3.54) requires x and y spatial derivatives of both cell centered quantities such as ρ, A_1 and A_2, and fluxes. How these derivatives are found is explained with a model equation:

$$(res) = \frac{\partial f}{\partial x} + \frac{\partial g}{\partial y} \tag{3.87}$$

where f and g are the values inside the derivatives.

timestep size	total displacement	% change
0.1×10^{-1}	2.1956051×10^{-3}	—
0.1×10^{-2}	2.1963205×10^{-3}	0.03
0.1×10^{-3}	2.1963276×10^{-3}	0.0003

Table 3.1: Effect of timestep size

To begin, this equation must be transformed into the computational domain as per section 3.7. The resulting equation is:

$$D * (res) = \frac{\partial F}{\partial \xi} + \frac{\partial G}{\partial \eta} \tag{3.88}$$

where

$$F = f(y_\eta) + g(-x_\eta) \qquad \text{and} \qquad G = f(-y_\xi) + g(x_\xi) \tag{3.89}$$

To calculate the residual, the quantities F and G are calculated at the cell faces. The ξ differential is then found by subtracting the F value on the left face from the right face, then dividing by $\Delta\xi = 1$. Similarly, the η differentials are found by subtracting the G value on the bottom face from the top face value then dividing by $\Delta\eta = 1$. In the code, residual values are reduced to 0.5×10^{-9} in both the continuity and stream function calculations.

What remains is how to find f and g in order to get F and G at the cell faces. In the case where a component of f is simply a cell centered value (such as is ρ in equation 3.54), the value is simply linearly interpolated to the cell face. If the component is a flux created from cell centered values, the value from one cell center is subtracted from an adjacent cell to produce the

flux at the appropriate face.

One case of interest to the differencing was found with the calculation of the source term in the convection equation, represented as H in equation (3.45). Some parts of the source term required achieving a cell-centered solution of a single spatial derivative of cell centered values. In particular, the spatial derivatives of the material variables as defined by equations (3.30) and (3.31). To accomplish this, it was found necessary to perform an interpolation from 6 cells to obtain a face centered value before apply the differencing. For example, the cell-centered value of $\frac{\partial Y}{\partial y}$ is found as follows:

$$\begin{aligned} Y_{i,j-1/2} &= 0.125(Y_{i-1,j} + Y_{i-1,j-1} + 2Y_{i,j} + 2Y_{i,j-1} \\ &\quad + Y_{i+1,j} + Y_{i+1,j-1}) \end{aligned} \tag{3.90}$$

and

$$\begin{aligned} Y_{i-1/2,j} &= 0.125(Y_{i-1,j-1} + Y_{i,j-1} + 2Y_{i,j} + 2Y_{i-1,j} \\ &\quad + Y_{i,j+1} + Y_{i-1,j+1}) \end{aligned} \tag{3.91}$$

The differencing scheme is then applied as:

$$\begin{aligned} \frac{\partial Y}{\partial y} &= \frac{1}{D}\Big[Y_{i,j+1/2}(x_\xi)_{j+1/2} - Y_{i,j-1/2}(x_\xi)_{j-1/2} \\ &\quad + Y_{i+1/2,j}(-x_\eta)_{i+1/2} - Y_{i-1/2,j}(-x_\eta)_{i-1/2}\Big] \end{aligned} \tag{3.92}$$

It was found that this way of differencing the terms in the cell-centered sources eliminated errors in these sources in non-uniform meshes.

3.10 Initial conditions

The last things required to be able to solve the convection and elliptic equations are the initial and boundary conditions. The model of the spacecraft motion from section 2.5.1 was constructed such that the initial fluid velocities are zero. The parameters in the Clebsch/Weber decomposition, equation (3.24) and (3.25), are set initially set to satisfy this state.

The initial conditions on the solution variables are thus set as:

$$\phi = 0 \tag{3.93}$$

$$\beta = 0 \tag{3.94}$$

$$A_1 = 0 \tag{3.95}$$

$$A_2 = 0 \tag{3.96}$$

$$X = x \tag{3.97}$$

$$Y = y \tag{3.98}$$

$$\rho = \text{initial density distribution} \tag{3.99}$$

The material coordinates values are set to their corresponding grid locations. The density is initially set to a non-dimensinal value of 1.0 for all cell locations in the case of uniform density. In the case where a density interface is used, the top half of the domain uses a density of 1.0, and the bottom half is set to 0.9, resulting in a 10% density difference.

With ϕ and β set to any constant value, the first two terms in the velocity decompositions are assuredly zero. The non-conservative terms A_1 and

A_2 are set to zero since the model of spacecraft motion predicts zero initial angular velocity, ($\dot{q}$). This was done by design, using a function of a cosine in the translational term in equation (2.58) to yield sine functions of time in the angular acceleration (2.64), creating the initial zero value.

3.11 Boundary conditions

The boundary conditions reflect the solid walls of the cavity in which the fluid experiment is held. A no-flux condition is satisfied at these boundaries especially through the use of the ϕ potential and the continuity equation. Two sets of boundary conditions are used, depending on the shape of the domain.

A boundary condition common to both domain shapes is used in the steady state solver for the elliptic equations, described in section 3.6. The 2-step approximate factorization of equation (3.67) uses a non-physical intermediate value $\Delta\phi'$ in the first of two sweeps used to solve the equation. The first sweep is to the right and up in the computational domain, and so only the bottom and left boundaries for $\Delta\phi'$ need to be specified. The second sweep is down and to the left, so $\Delta\phi$ boundaries are specified for the top and right sides.

Since this equation is being iterated to a steady-state, the final solution for $\Delta\phi'$ is known to be zero. For this reason, the boundary condition is set

as:

$$\Delta\phi' = 0 \tag{3.100}$$

to be certain of an acceptable boundary condition.

3.11.1 Rectangular domain

All variables aside from ϕ are set along the boundaries to reflect continuous functions. To that effect, the first derivatives of β and ρ are set to zero at the boundary with:

$$\frac{\partial\beta}{\partial\vec{n}} = 0 \tag{3.101}$$

$$\frac{\partial\rho}{\partial\vec{n}} = 0 \tag{3.102}$$

where $\vec{n}$ represents the normal direction to the boundary in the spatial derivative.

When similar boundary conditions were used for the material coordinates X and Y, as well as the A_1 and A_2 variables, it was found that discontinuities near the boundaries appeared in these variables and eventually in the flow field description. To avoid these discontinuities, it was found to be necessary to set the 3rd derivatives in the normal direction to the boundary to zero. This is shown here for the left hand side solid boundary condition, but is similar for all four walls.

$$X_{1,j} = \frac{(x_{3,j} - x_{1,j})X_{2,j} - (x_{2,j} - x_{1,j})X_{3,j}}{x_{3,j} - x_{2,j}} \tag{3.103}$$

$$Y_{1,j} = \frac{(x_{3,j} - x_{1,j})Y_{2,j} - (x_{2,j} - x_{1,j})Y_{3,j}}{x_{3,j} - x_{2,j}} \tag{3.104}$$

$$A1_{1,j} = \frac{(x_{3,j} - x_{1,j})A1_{2,j} - (x_{2,j} - x_{1,j})A1_{3,j}}{x_{3,j} - x_{2,j}} \quad (3.105)$$

$$A2_{1,j} = \frac{(x_{3,j} - x_{1,j})A2_{2,j} - (x_{2,j} - x_{1,j})A2_{3,j}}{x_{3,j} - x_{2,j}} \quad (3.106)$$

Here, the second derivatives have been found at two locations and are set equal to each other. This relation is then written in terms of the phantom cell.

To ensure the no-flux condition on the boundaries, all normal velocities are set to zero. To accomplish this, special use is made of the ϕ variable in the velocity decomposition. A value for ϕ is chosen in the phantom cells such that the normal component of the velocity is equal to zero:

$$u_n = 0 = \frac{1}{\rho}\frac{\partial \phi}{\partial n} + \frac{\partial X}{\partial \vec{n}}A_1 + \frac{\partial Y}{\partial \vec{n}}A_2 \quad (3.107)$$

where $\vec{n}$ represents the normal direction to the boundary. Note that this takes into account the fact that the first derivative of β normal to the boundaries was set to 0. To this end, the boundary conditions for ϕ are:

$$\phi_{1,j} = \phi_{2,j} + \rho_{i+1/2,j}[A1_{i+1/2,j}(X_{2,j} - X_{1,j}) + A2_{i+1/2,j}(Y_{2,j} - Y_{1,j})] \quad (3.108)$$

where (i+1/2) values are created with simple averaging. This is shown once again at the left face, but the method is used for all walls. With the continuity equation used to get ϕ, the no-flux boundary condition is satisfied.

3.11.2 Circular domain

The no-flux condition on the solid boundary of the circular domain is satisfied in exactly the same way as the solid walls of the rectangular cavity, as

shown in the previous section. The solid boundary, given as line BC in figure (3.4), once again uses zero first derivatives for ρ and β, zero third derivatives for A_1, A_2, X and Y, and the velocity decomposition for ϕ.

The differences from the rectangular domain arise when the periodic boundaries of lines AB and CD are considered, as well as the central boundary for line AD. The periodic boundaries are quite simple, since the phantom cell correspond to real cell locations, and are set to the value from the real cell for every variable. The material variable X is used as an example to describe this:

$$X_{m,j} = X_{2,j} \tag{3.109}$$

and

$$X_{1,j} = X_{m-1,j} \tag{3.110}$$

where 'm' represents the cell number corresponding to the phantom cell at the end of the domain.

The phantom cell values across the center point are set in much the same way since these phantom cells also correspond to real cell locations. The relation to the real cell locations is a bit more complex, however, and is once again shown for the material variable X to represent all variables:

$$X_{i,1} = X_{i+(m/2-1),2} \tag{3.111}$$

for i=2 to m/2 and

$$X_{i,1} = X_{i-(m/2-1),2} \tag{3.112}$$

for i=m/2+1 to m.

3.12 Code validation

In order to evaluate the validity of any results from the numerical code, a test case was performed to compare with results from an existing publication. In a 1998 paper, Yuferev et al. performed an analysis of fluid motion due to spacecraft rotation[38]. Although much of the work involved a density gradient induced by a thermal gradient, a baseline trial was done considering a uniform density. The applied source terms were due to angular acceleration and viscosity. As shown in section 2.6.2, the source term due to angular acceleration is similar to that produced by the model of motion employed by the code. With such a reduction made to the relative frames model in the code, a comparison was easily made between corresponding uniform density flow results.

The mesh used for these calculations, shown in figure (3.6), is a square 48×48 grid with uniform cell sizes. This is used to better reflect the cubical cavity used by Yuferev. Trials at domain sizes of 3.6, 6.3, 11.5, and 20cm were performed as was done in the paper, and maximum fluid velocities are then compared. The results from this comparison are shown in table 3.12.

These results show similar orders of magnitude. The differences are believed to be due to the fact that the paper's model performs 3-dimensional calculations with viscosity, where the model presented is only 2-dimensional

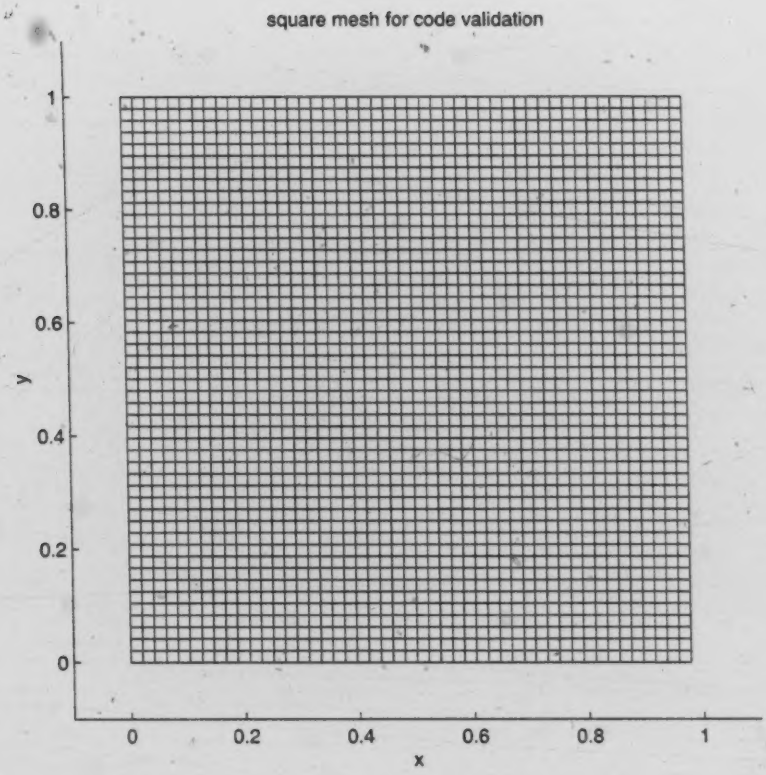

Figure 3.6: Square grid used for code validation

without viscosity. The results are closest when the domain size is about $10cm$; all subsequent test cases are run with this domain height.

domain size in cm	max velocity (Yuferev et al.[38]) in $\mu m/sec$	max velocity from code in $\mu m/sec$
3.6	0.54	2.9
6.3	2.8	5.0
11.5	13.8	9.3
20	40	16.1

Table 3.2: Maximum velocity comparison

Chapter 4

Results from Numerical Analysis

A numerical code is now used to evaluate the effects of the source terms created by the relative reference frames model. The test cases focus on highlighting the differences between the conventional sinusoidal g-jitter model and the relative frames model. The model predicts that the motion of the experimental frame will create motion where density gradients exist as well as where the fluid is of uniform density.

The test cases involve flows inside cavities, where all fluid flow is constrained by the solid boundaries. The first set of results describes flow inside a rectangular cavity containing a density interface. In this case, all sources generated by the relative frames model as well as the sinusoidal g-jitter model predict vorticity generation with the density interface, but the relative frames model also predicts vorticity generation independent of the interface due to the angular acceleration terms. The characteristics of the fluid motion with rotating terms is compared to the sinusoidal translation model.

The second set of results involves the identical parameters to the first case with the exception of the density interface. For these trials, the fluid will be set at a uniform density everywhere inside the cavity. For ease of comparison, the exact same set of parameters used for the first case is shown for the second case. In this case of uniform density, it is shown that only the angular acceleration terms can generate any motion. The velocities generated are compared to values meaningful to bacterial growth experiments.

A hypothesis was set forth in section (2.3.4), suggesting that the angular acceleration terms would result in rigid body motion of the fluid if it were not for the no-flux boundary conditions. This hypothesis is investigate more fully with the third test case, where a circular cavity containing a fluid of uniform density is studied. The resulting flow is compared to the second test case which involves a rectangular cavity with uniform density, thus demonstrating the effects of the boundary shape on non-conservative fluid flow.

4.1 Results from flows with a density gradient

In this first test case, a rectangular cavity containing two fluids of differing densities is studied. Where there is a density gradient, all terms predicted by the relative frames model can generate vorticity, or in other words all sources terms are non-conservative. The sinusoidally-varying g-jitter model also predicts motion due to the density interface, and is modeled to highlight the effects of rotating source terms.

The following parameters are used for all trials involving a density gradi-

ent:

- domain size of 10cm in y and 20cm in x
- density interface at y=0.5cm
- 10% difference in non-dimensional densities
- source term amplitude $n = 10^{-4}$
- source term frequency $\omega = 1.0Hz$
- timestep size of $\Delta t = 0.1 \times 10^{-2}$
- total run time of 5 seconds representing 5000 timesteps and 5 cylces of the source terms

As stated above, trials are run with a source amplitude of $n = 10^{-4}g_0$, and a frequency of $1.0Hz$. These values represent the midpoint in both amplitude and frequency used by Duval and Jacqmin[6]. It is also convenient that at a frequency of $1.0Hz$, the value of time equals the number of cycles.

The dimensional domain shape and grid are presented (in metres) in figure (4.1). A uniform mesh is used with 48 by 96 cells. To create the density difference, a non-dimensional value of 1.0 is set as the initial value to the fluid density in the top half of the domain, while a value of 0.90 is applied to the fluid in the bottom half.

To get an overall sense of the motion, time histories of enstrophy and kinetic energy for 5 cycles of the source terms will be shown for each trial. The enstrophy is calculated by taking the dot product of the vorticity, while kinetic energy is the total of the local kinetic energies from each cell, weighted

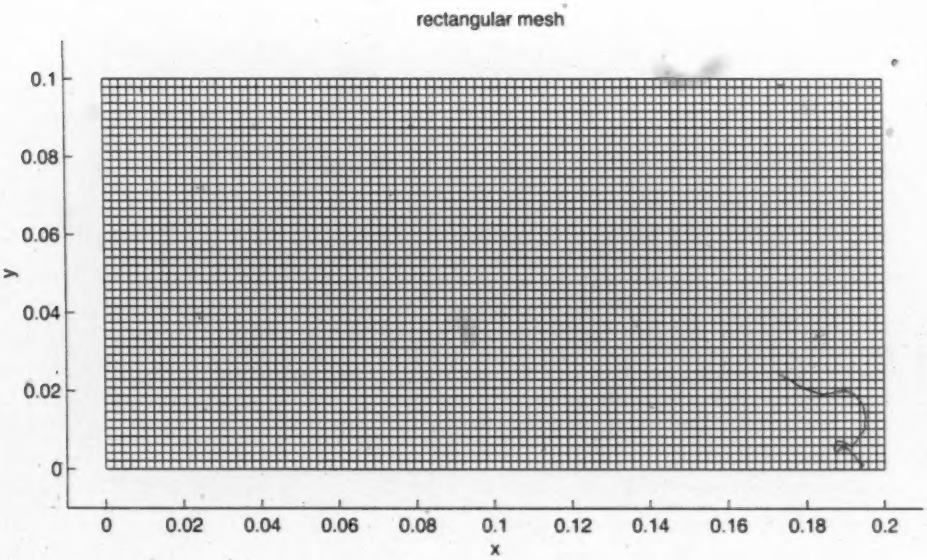

Figure 4.1: Rectangular mesh with uniform cell sizes

by the area.

The variables to be solved are ϕ, β, ρ, X, Y, A_1 and A_2, which come from the velocity decomposition. Except for the material coordinates X and Y and the density ρ, these values are all initially set to 0. The initial states of the material coordinates are given in figures (4.2) and (4.3), while the initial density interface is shown in figure (4.4).

The velocity and vorticity distributions are also calculated for each trial. These results will be useful in understanding how the flow is moving.

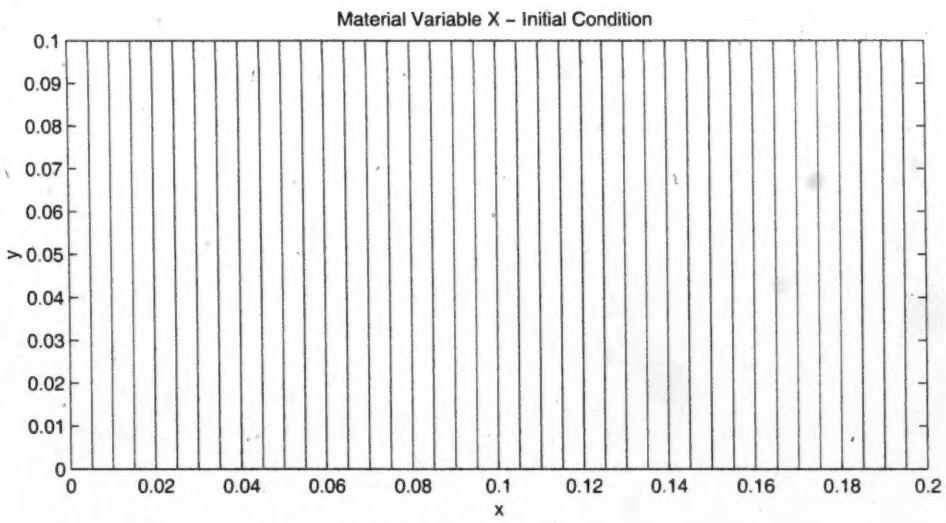

Figure 4.2: Material variable X, initial condition

4.1.1 Sinusoidal g-jitter

This first case shows the fluid motion that results from the sinusoidal 'g-jitter' source term only. As shown in section 2.6.1, this model is obtained by elimating all rotations and omitting gravity. The resulting velocity decomposition is written here in terms of cartesian components:

$$\begin{aligned} u &= \frac{1}{\rho}\frac{\partial \phi}{\partial x} + \frac{\partial \beta}{\partial x} \\ v &= \frac{1}{\rho}\frac{\partial \phi}{\partial y} + \frac{\partial \beta}{\partial y} \end{aligned} \tag{4.1}$$

where

$$\frac{D\beta}{Dt} = xng_0 \cos \omega t + \left(\frac{uu + vv}{2}\right) \tag{4.2}$$

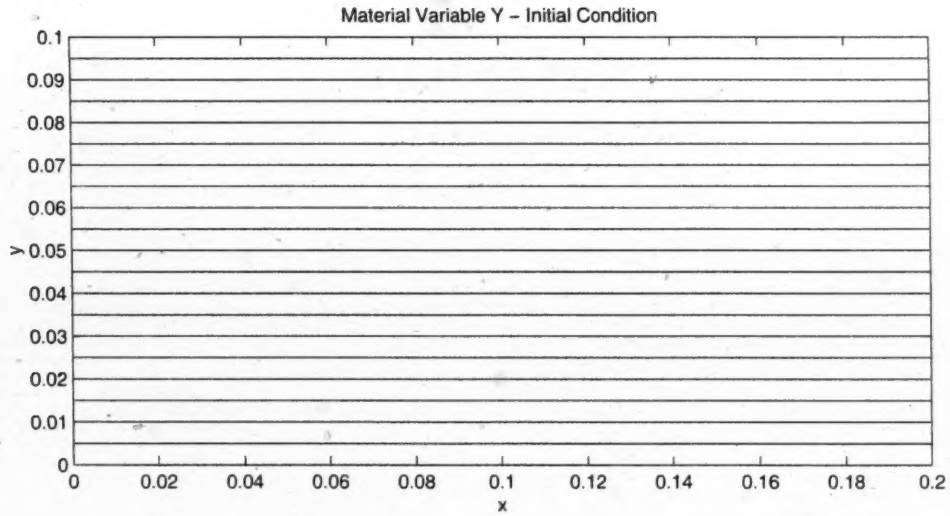

Figure 4.3: Material variable Y, initial condition

Note that the g-jitter term in the β potential is multiplied by x, indicating that this term acts parallel to the initial density interface.

The sinusoidal g-jitter term is run to 5 cycles, with the plot of enstrophy vs cycles given by figure 4.5. This plot shows a similar trend to the plot of kinetic energy vs cycles, given by figure 4.6. Both show periodic movement with local maximums at the 1/4 and 3/4 points in each cycles. Note that the orders of magnitude of the non-dimensionalized enstrophy and kinetic energy reach 10^4 and 10^5 respectively.

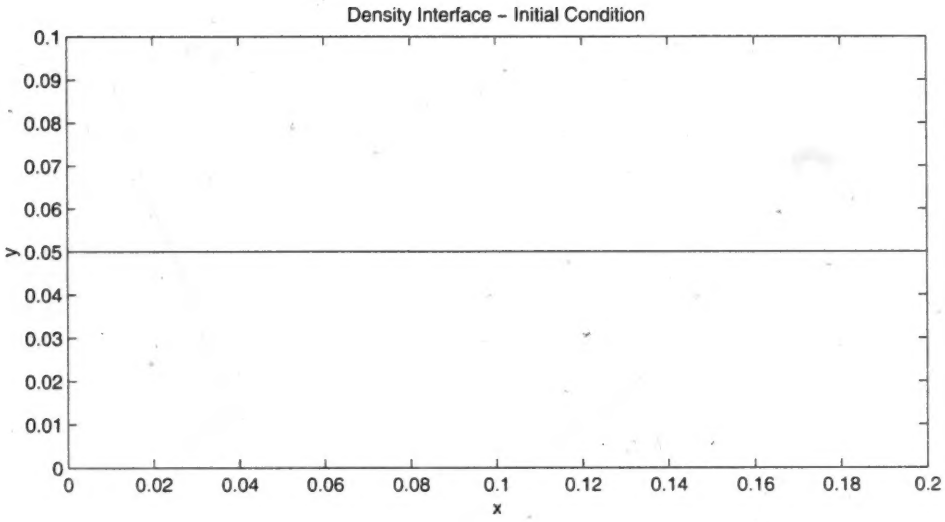

Figure 4.4: Density interface, initial condition

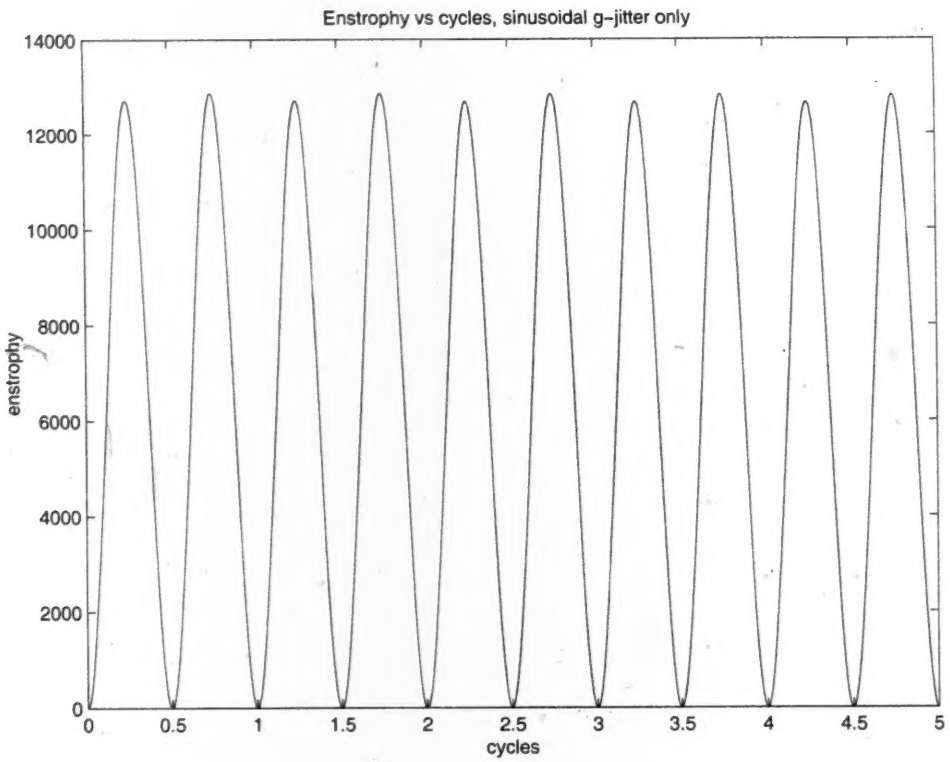

Figure 4.5: Enstrophy with sinusoidal g-jitter only

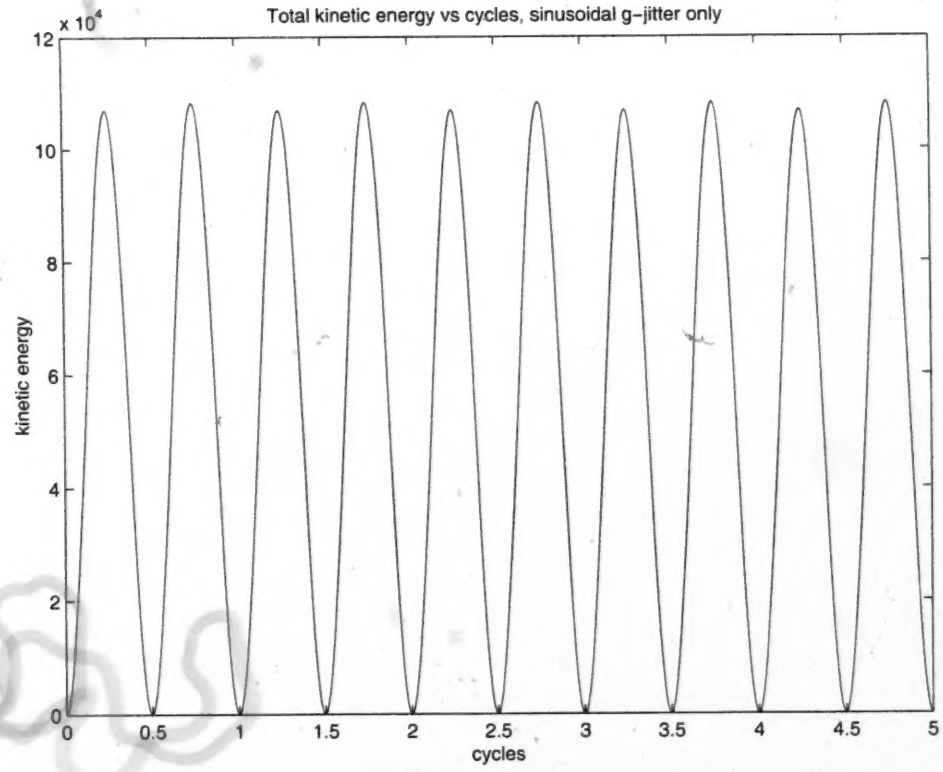

Figure 4.6: Kinetic Energy with sinusoidal g-jitter only

The plots of enstrophy and kinetic energy give insight into the overall motion. Now, some specific aspects of the motion are investigated. Some of the variables from the velocity decomposition, given by equation (4.1), are particularly suited for flow visualization and are contoured in the domain at a particular point in time. These variables are the density ρ, which can show the motion of the density interface, and the material variables X and Y, which show motion throughout the domain. The time chosen to display these variables represents a local maximum at 4.25 seconds, where the source

terms are one quarter of the way through the 5th and final cycle.

The density interface, displayed in figure (4.7), shows that there is no noticeable motion from the initial condition. This is supported by plots of the Lagrangian, or material coordinates in figures (4.8) and (4.9) which also appear to be at or near their initial positions.

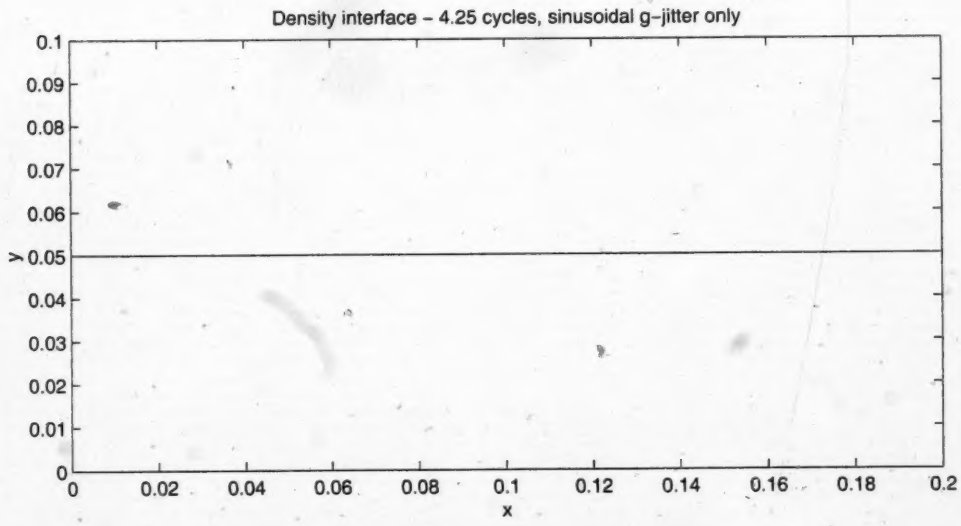

Figure 4.7: Density interface with sinusoidal g-jitter at 4 1/4 cycle

It is made clear, however, with the plots of the fluid speed, velocity vectors, and vorticity that there is motion in the fluid. Figure (4.10) shows fluid speeds reaching non-dimensionalized values in the order of tens, corresponding to tens of $\mu m/sec$. The highest values occur along the location of the density interface, and expecially at the ends of the interface. This is confirmed with the velocity vector plot, figure (4.12), which gives a better

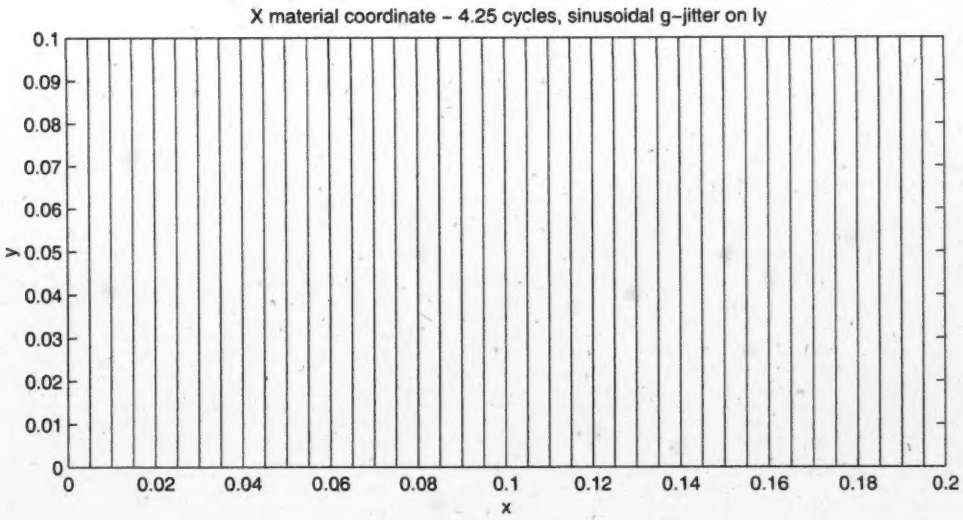

Figure 4.8: X material coordinate with sinusoidal g-jitter at 4 1/4 cycle

idea of the directions and relative magnitudes of the flows suggested by the speed plot.

The periodic nature of the flow is demonstrated in figures (4.11) and (4.13), where the flow is plotted a half cycle later at 4.75 cycles. The speed contours show similar magnitudes and patterns to the flow, but velocity vectors here show that the direction has reversed.

The vorticity plot in figure (4.14) supports the idea that the time varying body force source term can only generate vorticity where there is a density interface. The figure shows a relatively constant vorticity being generated all along the interface.

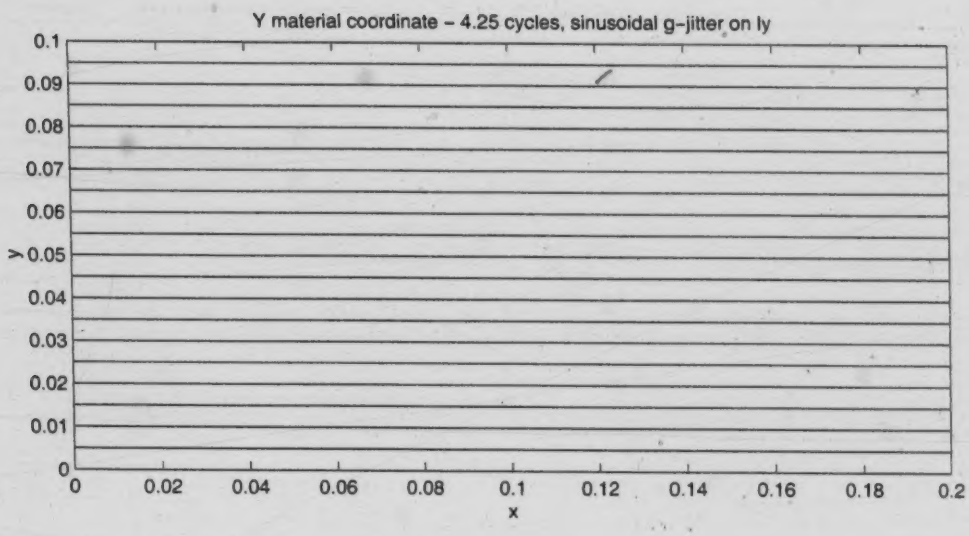

Figure 4.9: Y material coordinate with sinusoidal g-jitter at 4 1/4 cycle

The results of this trial display the simple g-jitter model that involves unidirectional accelerations varying sinusoidally with time. Although the fluid motion is quite small, it is clearly related to the density interface, where the otherwise conservative source term of the model can generate vorticity.

4.1.2 Complete relative frames model

The next trial uses the complete relative frames model, as developed in chapter 2. With all source terms considered, the velocity decomposition being solved is rewritten here from section 3.3:

$$u = \frac{1}{\rho}\frac{\partial \phi}{\partial x} + \frac{\partial \beta}{\partial x} + \frac{\partial X}{\partial x}A_1 + \frac{\partial Y}{\partial x}A_2 \tag{4.3}$$

$$v = \frac{1}{\rho}\frac{\partial \phi}{\partial y} + \frac{\partial \beta}{\partial y} + \frac{\partial X}{\partial y}A_1 + \frac{\partial Y}{\partial y}A_2 \tag{4.4}$$

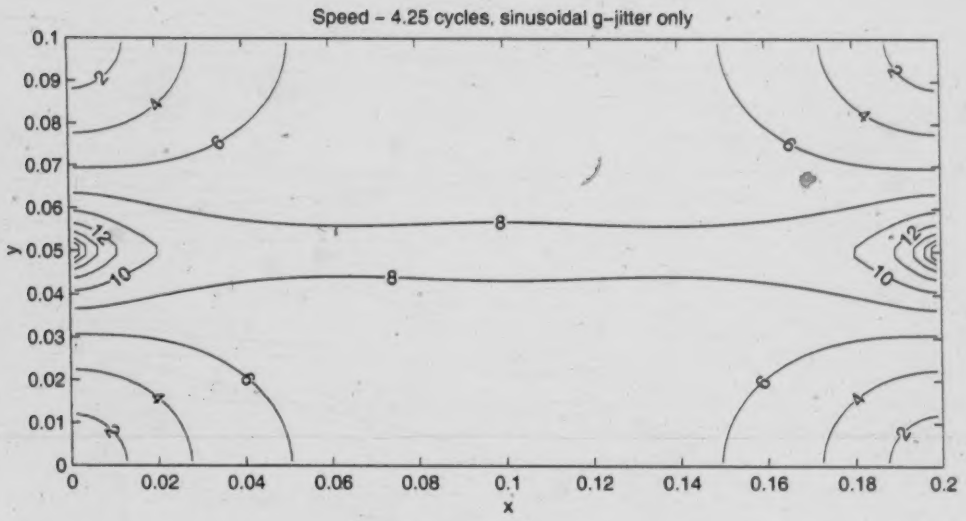

Figure 4.10: Fluid speed with sinusoidal g-jitter at 4 1/4 cycle

with

$$\begin{aligned}\frac{D\beta}{Dt} = & \left\{\frac{M_E G}{[(\alpha_{11}(\lambda_1+x)+\alpha_{21}(\lambda_2+y)+c_1)^2+(\alpha_{12}(\lambda_1+x)+\alpha_{22}(\lambda_2+y))^2]^{\frac{1}{2}}}\right\} \\ & +\left(\frac{Q^2}{2}+\frac{q^2}{2}+Qq\right)[(x+\lambda_1)^2+(y+\lambda_2)^2]-2\psi(Q+q) \\ & -\dot{q}(xy-x\lambda_2+y\lambda_1)+xQ^2\alpha_{11}c_1+yQ^2\alpha_{21}c_1 \\ & +2xQ(-\alpha_{12}\dot{c}_1)+2yQ(-\alpha_{22}\dot{c}_1)-x(\alpha_{11}\ddot{c}_1)-y(\alpha_{21}\ddot{c}_1) \\ & +\frac{uu+vv}{2} \end{aligned} \tag{4.5}$$

$$\frac{DA_1}{Dt} = \frac{2\dot{q}y}{\frac{\partial Y}{\partial y}\frac{\partial X}{\partial x}-\frac{\partial Y}{\partial x}\frac{\partial X}{\partial y}}\left(\frac{\partial Y}{\partial y}\right) \tag{4.6}$$

and

$$\frac{DA_2}{Dt} = \frac{2\dot{q}y}{\frac{\partial Y}{\partial y}\frac{\partial X}{\partial x}-\frac{\partial Y}{\partial x}\frac{\partial X}{\partial y}}\left(-\frac{\partial X}{\partial y}\right) \tag{4.7}$$

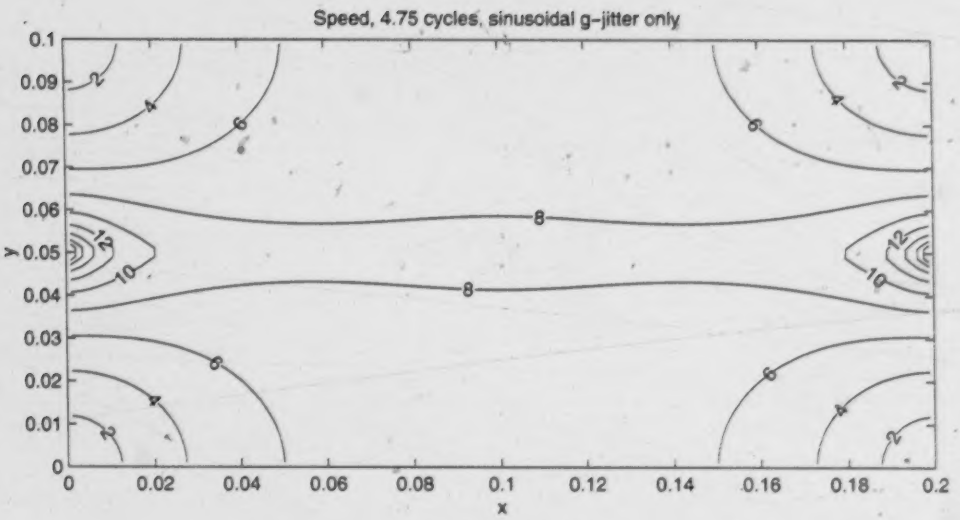

Figure 4.11: Fluid speed with sinusoidal g-jitter at 4 3/4 cycle

Just as was done in section 4.1.1, the amplitude used is $n = 10^{-4} g_0$ with a a frequency of $1.0Hz$. Though these values were selected for their appropriateness for the sinusoidal g-jitter model, they also produce acceptable values for the rotational sources terms predicted by the relative frames model. By the model from section 2.5.1, the maximum spacecraft angular velocity and accelerations that arise from using these values is $1.3 \times 10^{-7} \frac{rad}{sec}$ and $8.0 \times 10^{-7} \frac{rad}{sec^2}$, which falls below the maximum expected for angular velocity and matches the maximum angular acceleration predicted by Yuferev et al. [38]. A more detailed analysis of the validity of the model parameters is given in the order of magnitude discussion from section 2.5.2.

Although the identical source term amplitude and frequency are used, the difference in results is immediately apparent with the addition of the

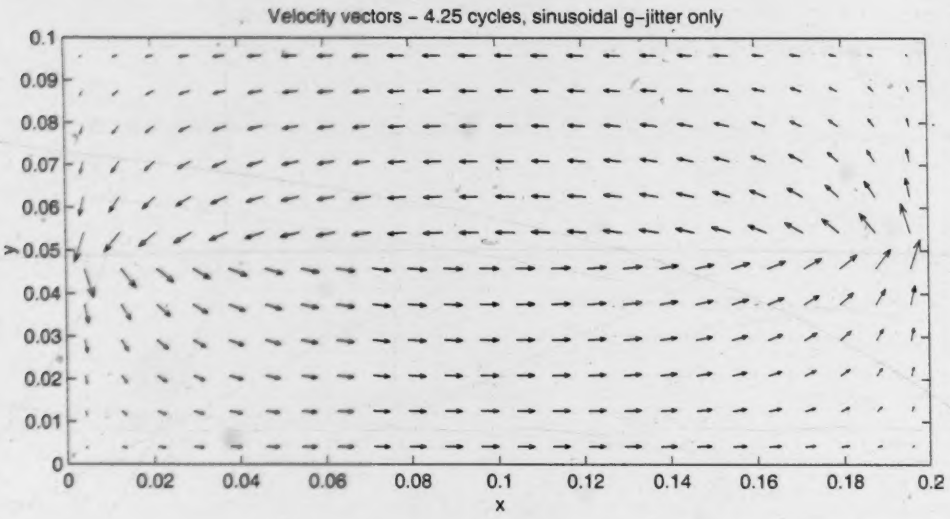

Figure 4.12: Velocity with sinusoidal g-jitter, 4 1/4 cycles (max velocity is 19.7 $\mu m/s$)

rotations. The time history of enstrophy and kinetic energy, figures 4.15 and 4.16, no longer demonstrate a clear periodic motion over the 5 cycles. Instead, there is significant growth in the motion as time progresses. This is not a completely unexpected result since the multiple source terms are not all in phase. The orders of magnitude of these plots are also much greater at 10^7 for enstrophy and kinetic energy.

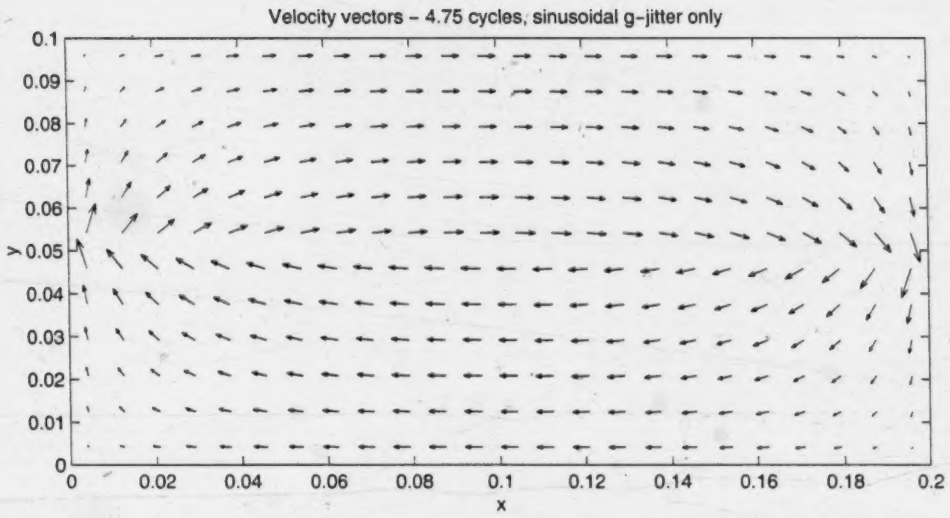

Figure 4.13: Velocity with sinusoidal g-jitter, 4 3/4 cycles (max velocity is 19.7 $\mu m/s$)

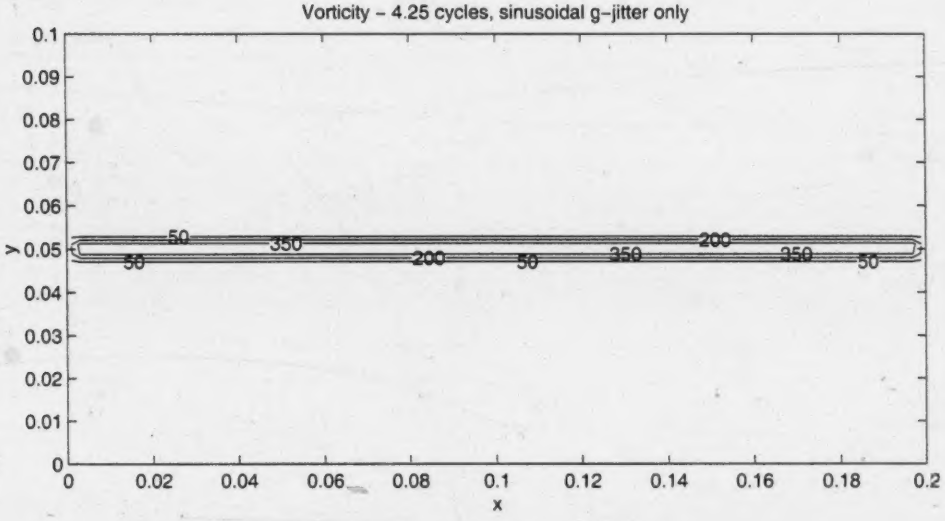

Figure 4.14: Vorticity with sinusoidal g-jitter at 4 1/4 cycle

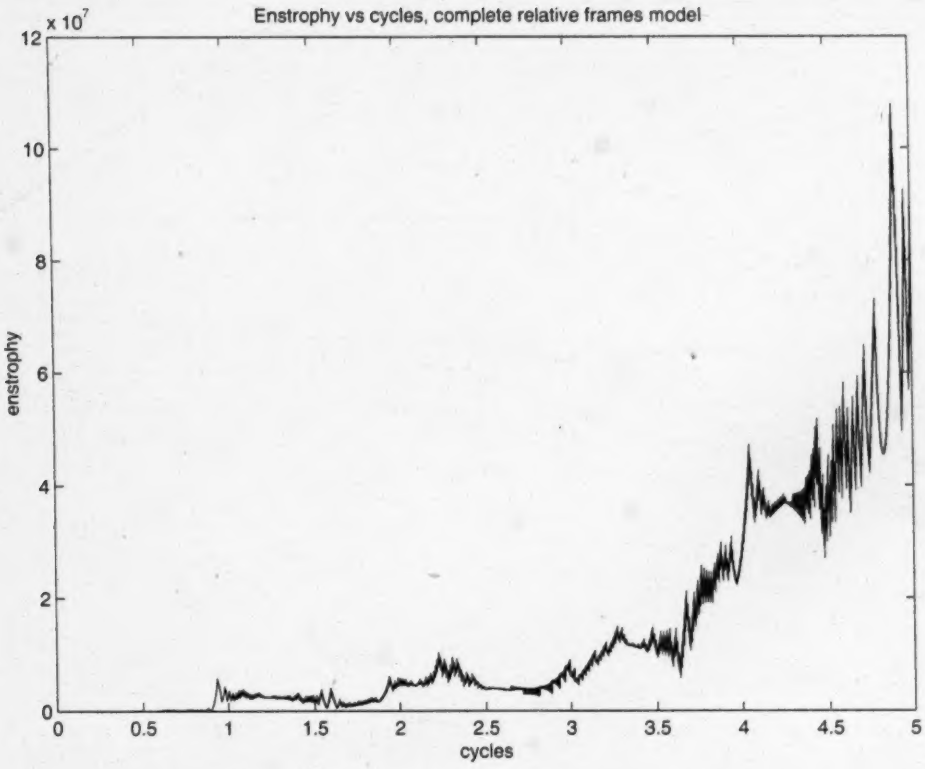

Figure 4.15: Enstrophy with complete relative reference frame model

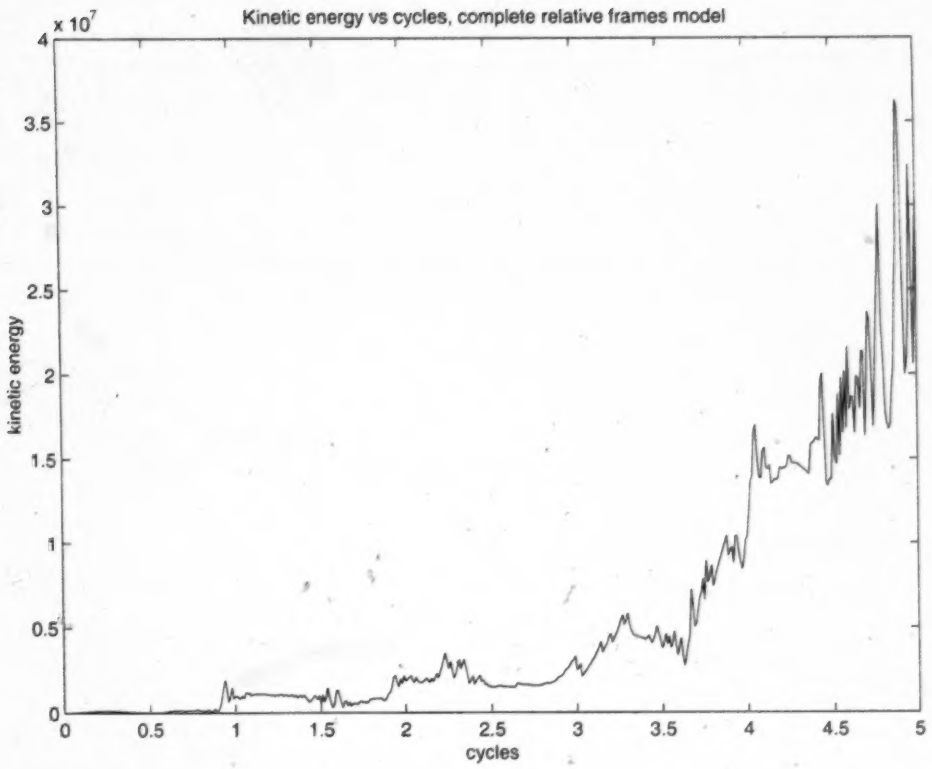

Figure 4.16: Kinetic Energy with complete relative reference frame model

The time selected to display the flow is at 4.25 seconds, which corresponds to the time considered with the sinusoidal g-jitter model. The same three flow visualization variables are plotted again, and the flows resulting from the relative reference frame model are compared to the simpler model.

The density interface is shown in figure (4.17) to have undergone some significant movement. Instead of the motion being concentrated near the edges of the interface, the relative frames model is predicting more motion

in the middle. The interface is less stable in this configuration as the density gradient occurs in multiple directions. This is reflected in the strong growth of enstrophy and kinetic energy with time.

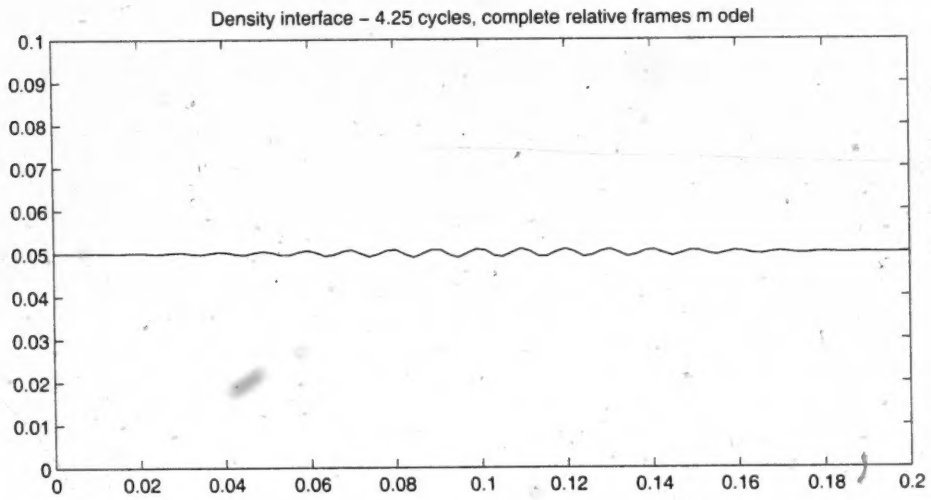

Figure 4.17: Density interface with complete relative reference frame model at 4 1/4 cycle

The material coordinate plots reinforce the notion that the motion is concentrated near the center of the density interface. Both the X and Y coordinates show this result, but the X coordinates in figure (4.18) show less motion than the Y coordinates in (4.23), indicating that the motion is mostly perpendicular to the interface at this point in time. In order to visualize the development of the flow over the 5 cycles, the Y coordinates are shown for every cycle at the 1/4 point of the cycle. This series of plots including figures (4.19) to (4.23) demonstrates that at each cycle, the motion in the fluid is

growing, especially near the interface.

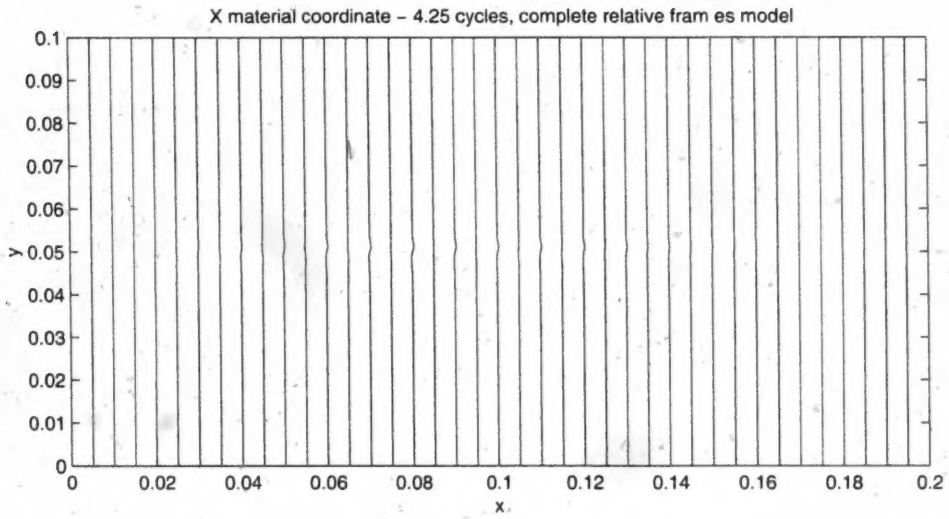

Figure 4.18: X material coordinate with complete relative reference frame model at 4 1/4 cycle

The plots of fluid speed and velocity vectors offer a definitive comparison between the sinusoidal g-jitter model and the complete relative frames analysis. The fluid speed, figure (4.24), is concentrated mostly in the middle section along the density interface. The equivalent plot from the g-jitter model, figure (4.10), shows the highest speeds at the edges of the interface. Further, the relative frames sources have generated speeds that an order of magnitude higher. The velocity vector plot of figure (4.25) shows the chaotic nature of the motion near the interface.

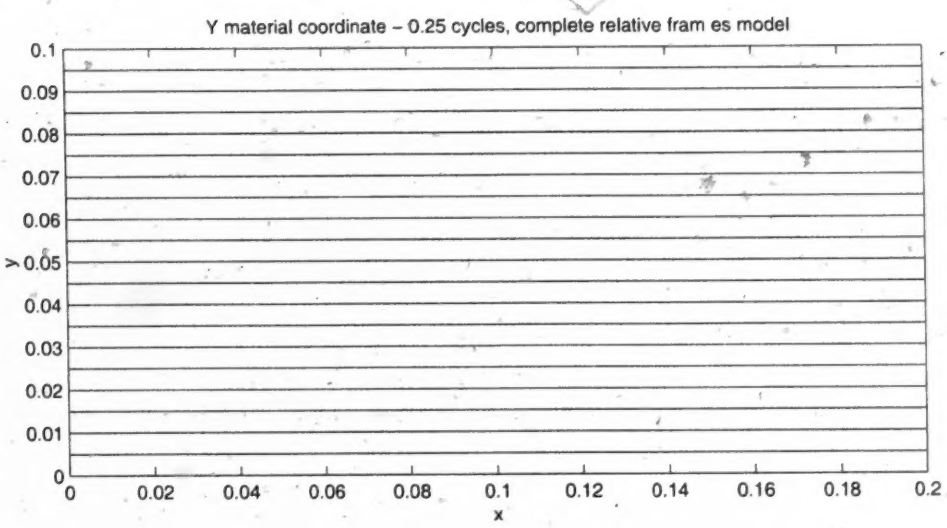

Figure 4.19: Y material coordinate with complete relative reference frame model at 1/4 cycle

The vorticity plot from the sinusoidal g-jitter model appeared as a constant gradient along the entire interface. Now, as figure (4.26) shows, there are a row of small vorticies along the interface, with the most intense vorticies located at the center of the domain. As is the case with fluid speeds, there is also an order of magnitude increase, this time of 2 orders from the simpler model to the relative frames model.

4.2 Results from uniform density flows

In the absence of a density gradient, some of the source terms predicted in the model from section 2.5.1 remain non-conservative and as such are able to generate vorticity. In a 2-dimensional flow, these sources are the A_1 and A_2

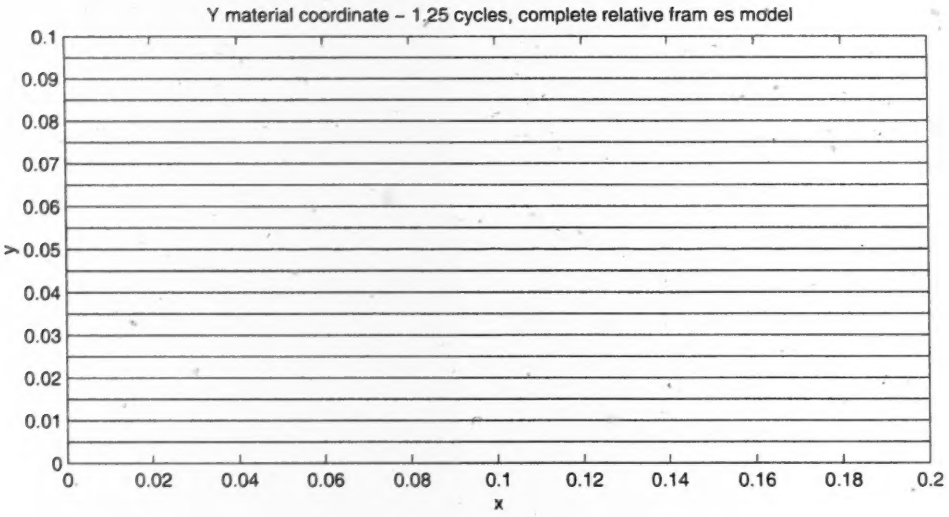

Figure 4.20: Y material coordinate with complete relative reference frame model at 1 1/4 cycle

terms in the velocity decomposition (3.18). In order to investigate the effects of these terms, computational experiments are performed where a cavity is completely filled with a fluid of uniform density.

The model parameters are similar to those used in section 4.1, except that there is of course no density difference applied. Once again, these parameters are:

- source term amplitude $n = 10^{-4}$
- source term frequency $\omega = 1.0Hz$
- timestep size of $\Delta t = 0.1 \times 10^{-2}$
- total run time of 5 seconds representing 5 cycles.

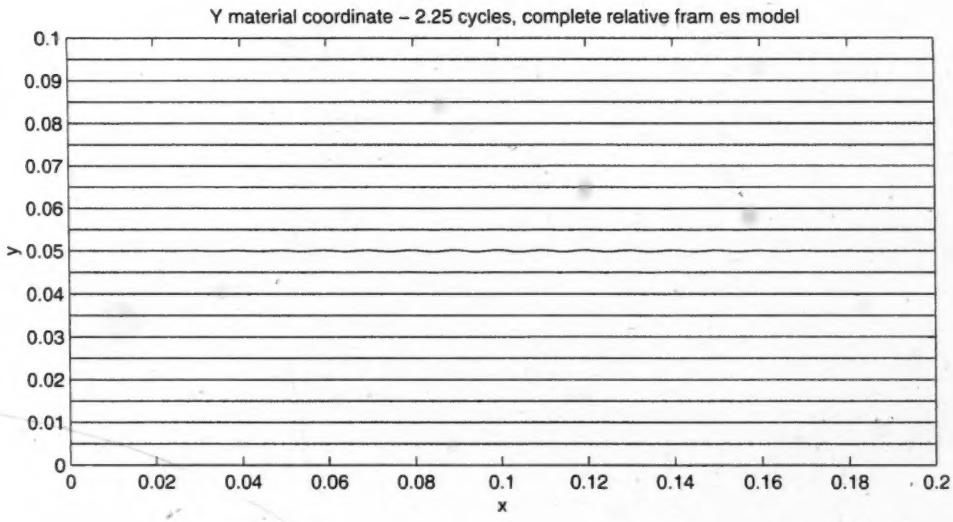

Figure 4.21: Y material coordinate with complete relative reference frame model at 2 1/4 cycle

As in the previous trials involving a density gradient, the first two trials of this section make use of the grid shown in figure (4.1). This not only allows a more direct comparison to be made between flows with and without a density gradient, but it also shows how the non-conservative motion responds to a rectangular cavity. This motion will be compared to the same motion in a circular cavity in section 4.2.3.

4.2.1 Sinusoidal g-jitter

To begin, the theoretical conclusion that a potential or conservative source cannot cause flow in a fluid of uniform density is verified numerically. This is done by performing the the identical trial to section (4.1.1) involving the sinusoidal g-jitter model. This model uses a potential body force to approx-

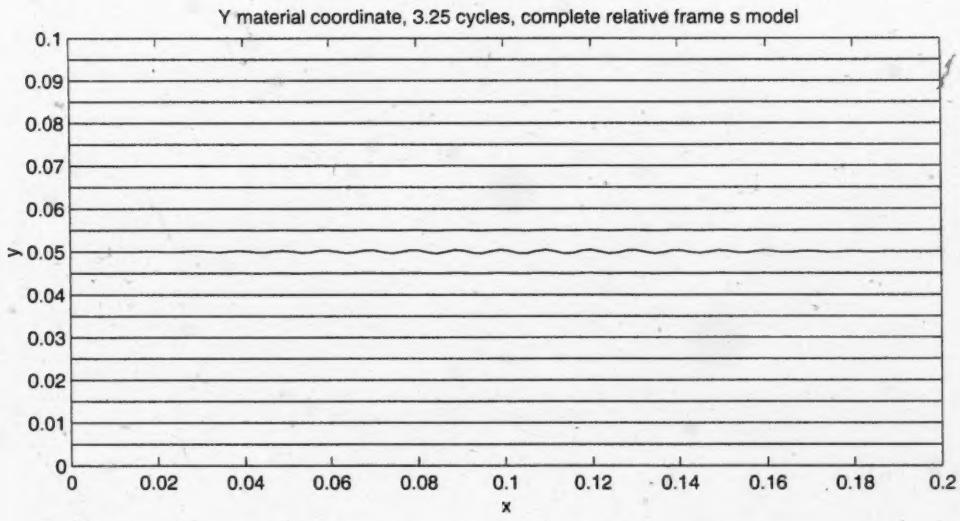

Figure 4.22: Y material coordinate with complete relative reference frame model at 3 1/4 cycle

imate the microgravity environment. The velocity decomposition for this model is described by equations (4.1) and (4.2), and once again all trials are performed with a source term amplitude of $10^{-4}g_0$ and a frequency of $1.0Hz$.

The resulting time histories of enstrophy and kinetic energy over 5 cycles showed maximum non-dimensional values of 7.4^{-19} and 1.4^{-14} respectively. These histories are shown in figures (4.27) and (4.28) for completeness, but the maximum values are below the set tolerance of the code as described in section 3.9 and as such are considered to be zero.

The no-flow results are further reinforced with plots of the material variables X in figure (4.29) and Y in figure (4.30). These material values show

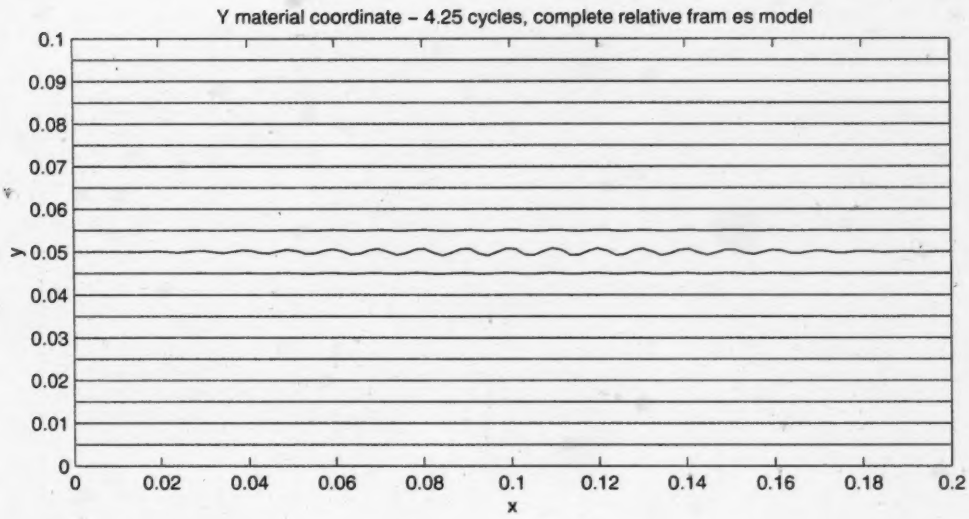

Figure 4.23: Y material coordinate with complete relative reference frame model at 4 1/4 cycle

no motion, as they appear identical to the initial conditions given by the corresponding figures (4.2) and (4.3).

No results are shown here for fluid speed or vorticity since the maximum values for these indicators were again too small for the code to resolve. Specifically, the maximum orders of magnitude of vorticity and speed over the 5 cycles were found to be of the same order as the specified tolerance at 10^{-9}.

The results from this trial confirm that no motion results in a uniform density flow if the microgravity model is limited to potential sources of motion, as is the case with a sinusoidally varying g-jitter model.

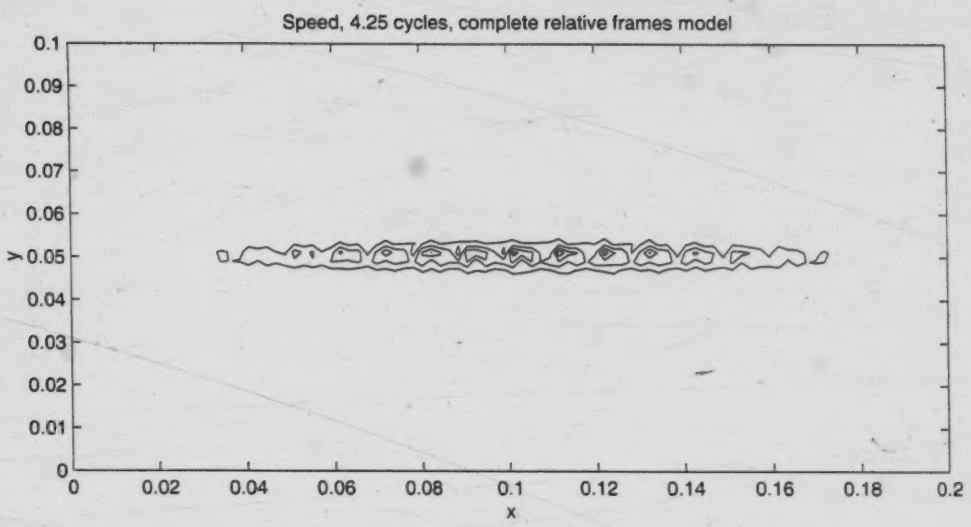

Figure 4.24: Fluid speed with complete relative reference frame model, 4 1/4 cycle (contours at 200, maximum value $O(10^3)$)

4.2.2 Complete relative frames model

A fluid of constant density is now investigated using the relative frames model for the microgravity model. The key element in this case is that this model predicts non-conservative source terms through angular acceleration. Although all source terms from the relative frames analysis are applied, only the non-conservative sources create any flow.

The velocity decomposition for the relative frames model is again given by equations (4.3) through (4.7). The only non-conservative sources arise from angular acceleration, $\dot{q}$, the value for which is obtained once again with the model from section 2.5.1. The same amplitude of $10^{-4}g_0$ and frequency

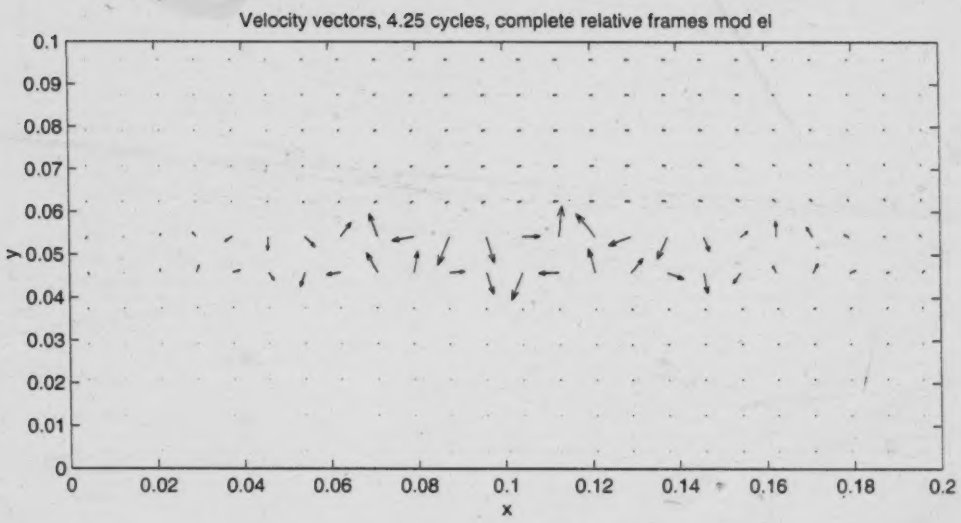

Figure 4.25: Velocity with relative frames model, 4 1/4 cycles (max velocity is 949 $\mu m/s$)

of $1.0Hz$, used in all previous trials, is again used. The resulting maximum angular accelerations are of the order of $10^{-7}\frac{rad}{sec^2}$, matching the prediction of Yuferev et al[38].

In section 2.3.4, it is proposed that the motion predicted by the angular acceleration term, $\rho\dot{q}_p\epsilon_{ipk}x_k$, would be rigid body if not for the cavity boundaries. This results is of considerable interest because of the way it relates to Tryggvason's belief that the deficiency of current microgravity models can be addressed through a boundary issue. This phenomenon will be studied here with special attention to fluid speed plots, velocity vectors, and vorticity contour distributions. These results will later be compared to similar results in a circular cavity, where the effects of the change in boundary shape can

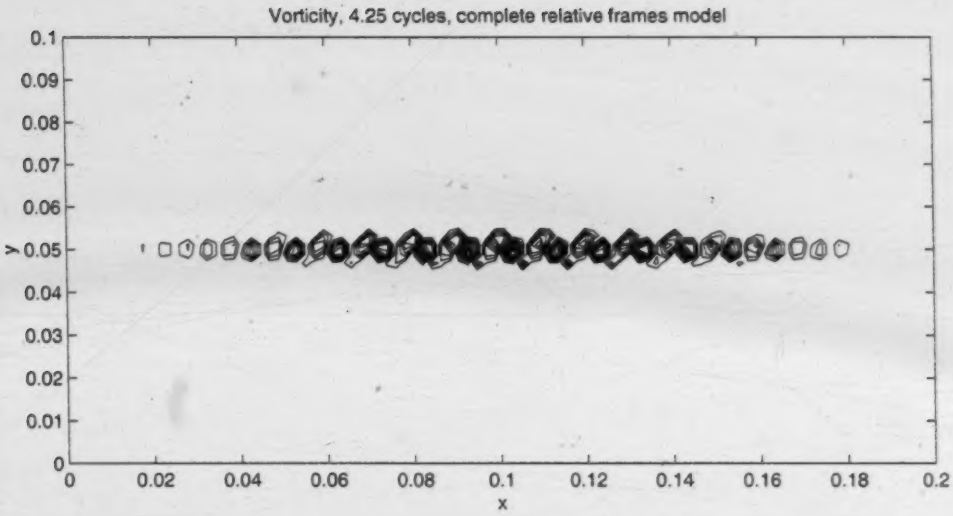

Figure 4.26: Vorticity with complete relative reference frame model at 4 1/4 cycle (contours at 5000, maximum value $O(10^4)$)

be observed.

Figures 4.31 and 4.32 describe the resulting motion due to the non-conservative sources in the fluid of uniform density. The enstrophy and kinetic energy only reach magnitudes of 10^{-3} and 10^{-1} respectively, but it is clear that fluid motion does exist. The maximum velocity obtained for this case is $0.023 \mu m$ sec, obtained at the 1/2 cycles. The motion appears periodic in nature over the 5.0 cycles considered.

Since the motion being considered here is quite small, the plots of the material variables would be expected to have changed little from the initial conditions. Figures (4.33) and (4.34) showing plots of material X and Y

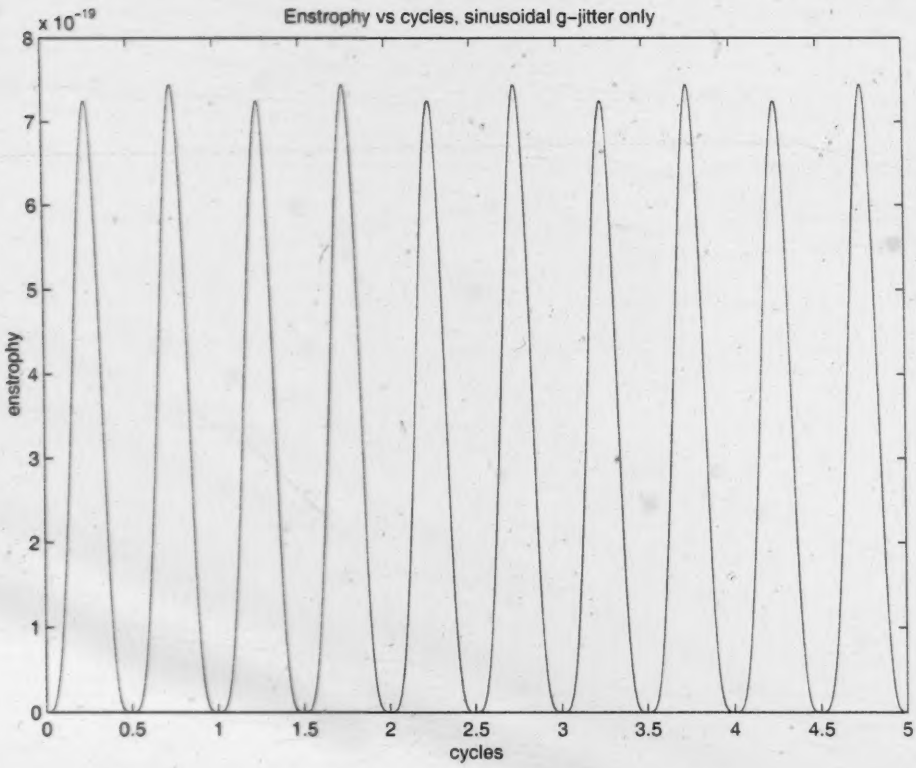

Figure 4.27: Enstrophy with sinusoidal g-jitter model in a fluid of uniform density

confirm this expectation, shown here at 4.5 cycles.

Although the fluid motion is quite small, it can be studied by looking at the fluid speed contours and the velocity vector plot (again at 4.5 cycles). Figure (4.35) shows values in the order of 10^{-2} near the middle of the walls, confirming that fluid motion does exist. The maximum speed in the fluid was found to be 0.023 $\mu m/sec$.

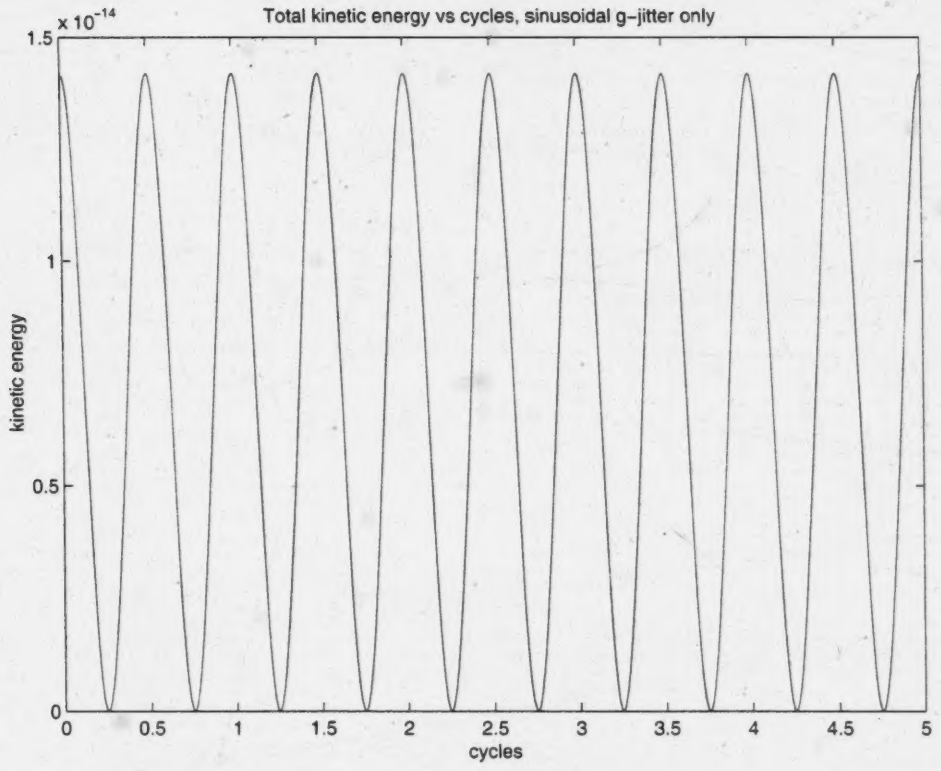

Figure 4.28: Kinetic energy with sinusoidal g-jitter model in a fluid of uniform density

The motion is attributed entirely to the angular velocity – the only non-conservative terms predicted by the 2 dimensional model. The velocity vector plot, figure (4.36), shows how these terms create flow inside a cavity. In the discussion from section 2.3.4, the angular velocity terms of $\rho \dot{q}_p \epsilon_{ipk} x_k$ from the momentum equation appear to predict rigid body motion of the fluid. However, the solid boundaries of the rectangular cavity modify this

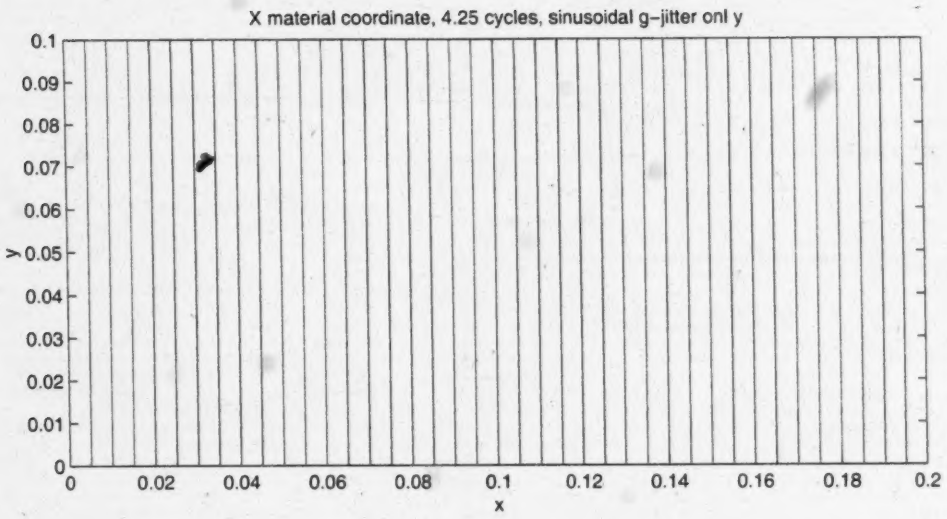

Figure 4.29: X material coordinate with sinusoidal g-jitter model in a fluid of uniform density

prediction, as shown in figure (4.36). Here, the would-be rigid rotational flow adjusts for the boundaries and turns corners, thus creating non-rigid flow. This result will be compared in section 4.2.3 to a similar case in a circular cavity.

4.2.3 Uniform density flows in a circular cavity

It has been shown that the simple sinusoidally varying body force does not create motion in a fluid of uniform density. In such fluids, only non-conservative sources, such as those predicted by the relative frames model, can create motion. The only non-conservative sources in this 2-dimensional model result from the angular acceleration, which suggests rigid body motion of the fluid in the absence of solid boundaries.

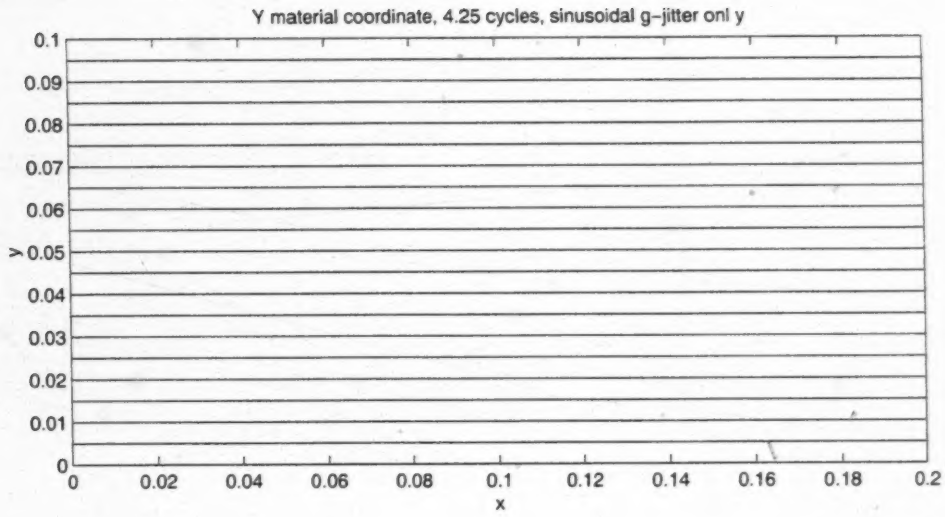

Figure 4.30: Y material coordinate with sinusoidal g-jitter model in a fluid of uniform density

In section 4.2.2, it was shown that in a rectangular cavity, the fluid flow resulting from the angular acceleration terms adjusts to the boundaries, creating non-rigid body motion. In this section, the nature of the non-conservative motion is studied by considering flow in a circular cavity. Here, rigid body rotation is possible since the fluid is inviscid.

The grid and domain to be used for this trial are shown in figure (4.37). The diameter of this circular cavity is set to 10cm to match the height of the rectangular cavity. The boundary conditions have been adjusted according to section (3.11.2) to account for this new grid shape, but the motion parameters being used are the same as from previous cases. In other words, the

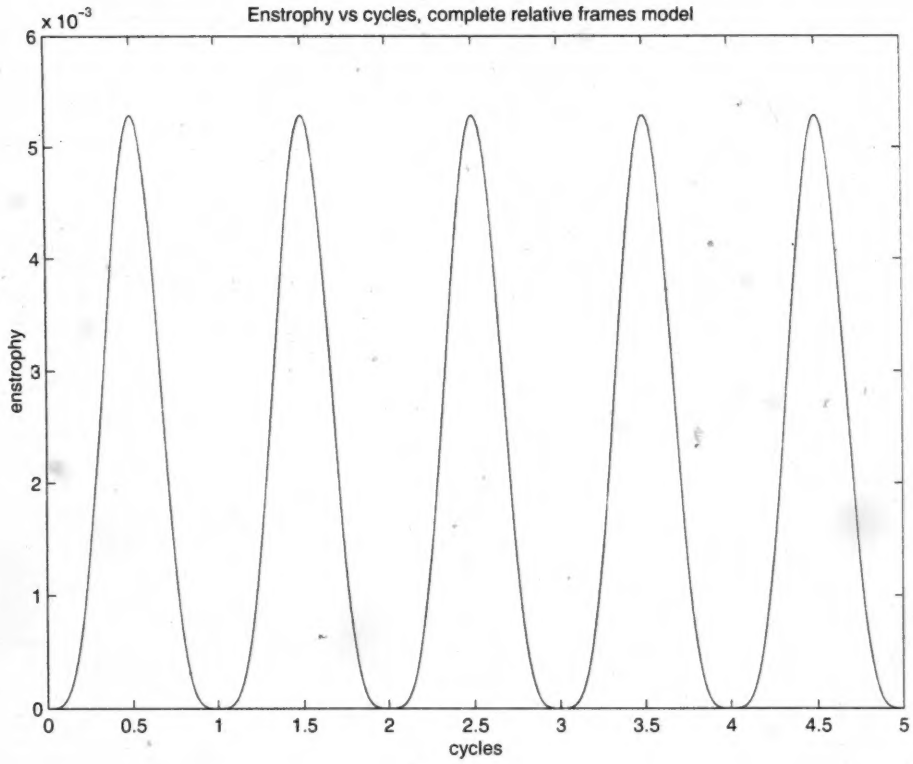

Figure 4.31: Enstrophy with relative frames model in a fluid of uniform density

source term amplitude is once again set to $n = 10^{-4}$, and the source term frequency is $\omega = 1.0Hz$. The timestep size is again $\Delta t = 0.1 \times 10^{-2}$, run to 5.0 seconds or 5000 steps.

The initial conditions for the material coordinates that result from this grid shape are contoured in figures (4.38) and (4.39).

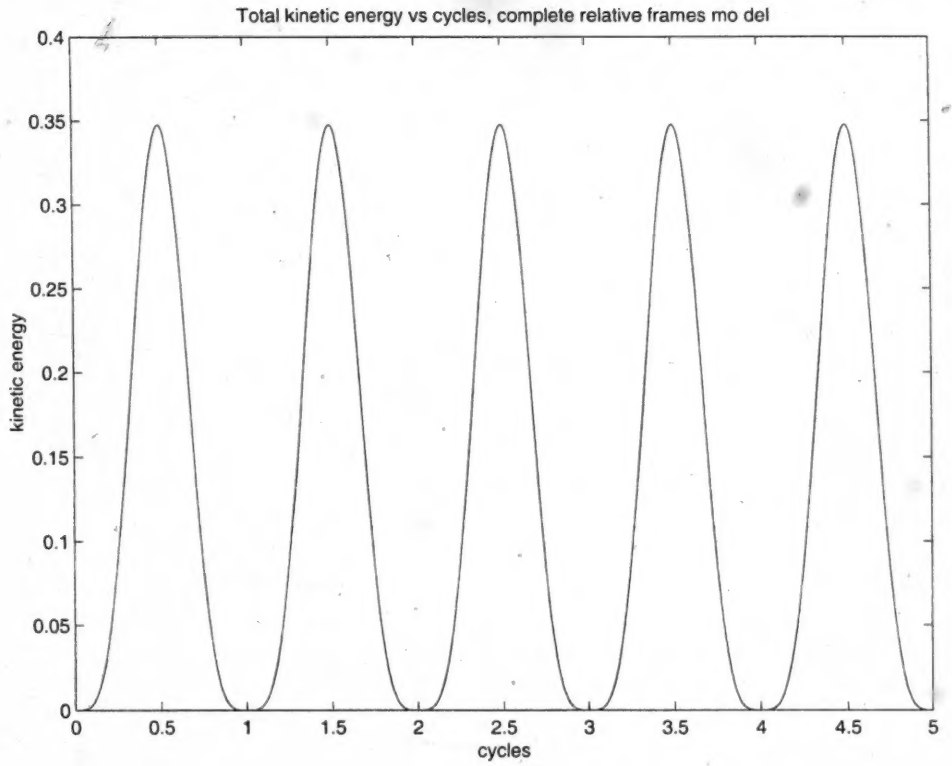

Figure 4.32: Kinetic Energy with relative frames model in a fluid of uniform density

As was done in the previous cases, the time histories of enstrophy and kinetic energies are shown, here in figures (4.40) and (4.41). The magnitude for the kinetic energy history is similar to that found in the rectangular cavity shape at 10^{-2}, but the enstrophy is a bit smaller at 10^{-3}. This may be due to the slightly smaller cavity size, where the circle has a diameter of 10cm and the rectangle is 10 by 20cm. The periodic patterns are also similar to those found in section 4.2.2, where local maxima occur at the half cycles.

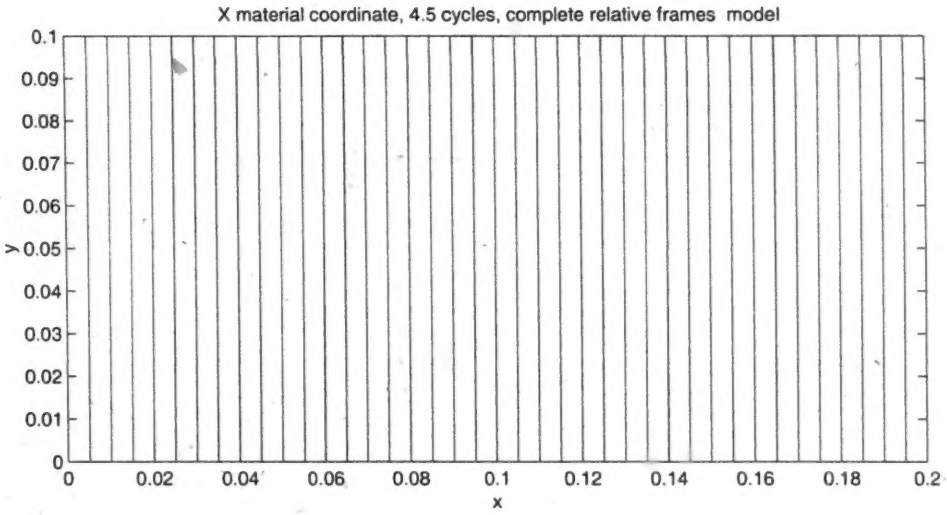

Figure 4.33: X material coordinate with relative frames model in a fluid of uniform density

To view the flow, the material coordinates are plotted at the time t=4.5 seconds, corresponding to the local maximum in enstrophy and kinetic energy. Figures (4.42) and (4.43) show little change from the initial conditions.

A better representation of the fluid motion is found in the speed contours and velocity vectors, shown in figures (4.44) and (4.45). As anticipated, these plots appear to reflect rigid body rotation of the fluid, where the velocity is linearly proportional to the radius at in the same for way every location in the fluid[2].

The velocity in the circular cavity from figure (4.45) and the velocity

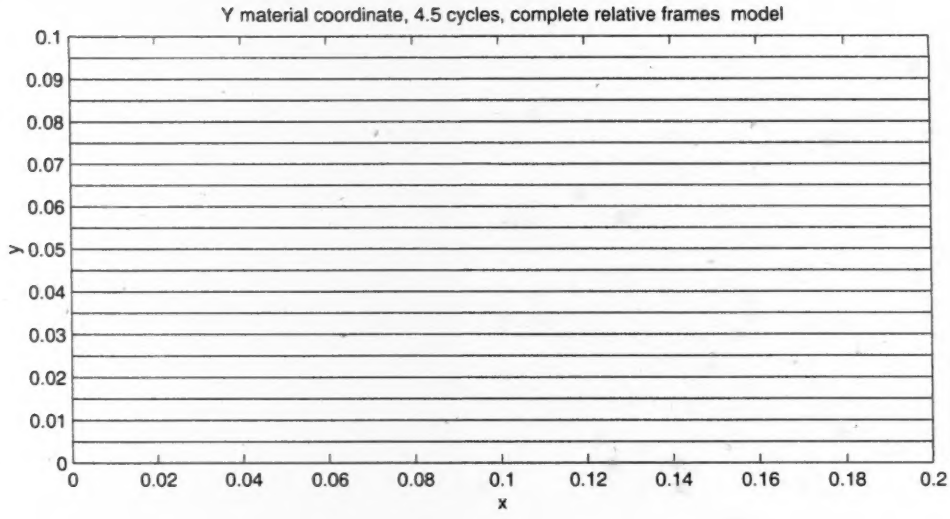

Figure 4.34: Y material coordinate with relative frames model in a fluid of uniform density

in the rectangular cavity from figure (4.36) describe the nature of the non-conservative flow due to angular acceleration. This term, which appears as $\rho\dot{q}_p\epsilon_{ipk}x_k$ in the momentum equation, leads to rigid body rotation of the fluid. This fluid motion changes from rigid body when the solid boundaries of the cavity get in the way, as in the case of a rectangular domain.

4.3 Summary

The results of the numerical analysis provide insight into three important ideas. The first is that even where a density gradient exists, the effect of source terms derived from multiple reference frames in the equations of motion can be important. It is clear from the analysis of the density interface

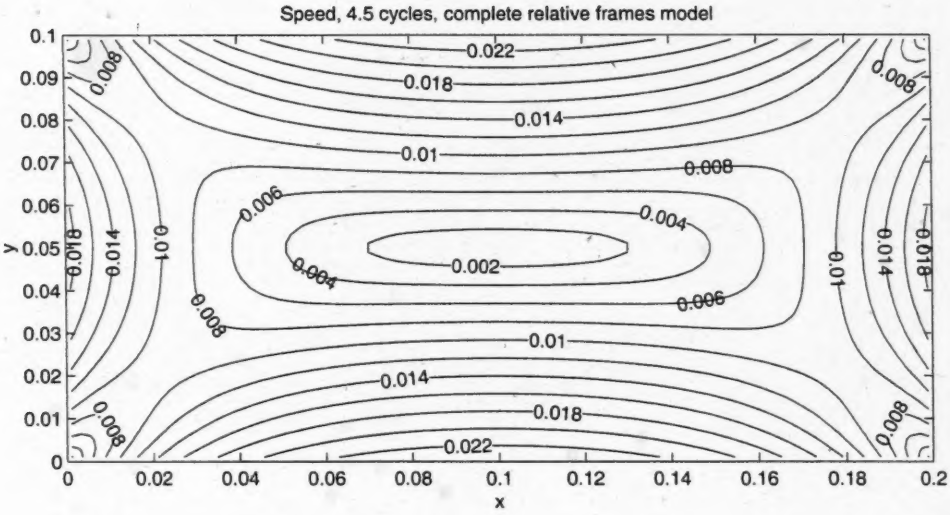

Figure 4.35: Fluid speed with relative frames model in a fluid of uniform density

flows that the rotating sources can encourage the breakdown of the interface.

The second idea that is suggested by the results is that with a fluid of uniform density in a microgravity environment, there is certainly flow due to spacecraft rotations. This result is significant to any such experiment. In the case of increased bacterial growth described in section 1.1, the mechanisms proffered by Klaus et al.[17] would certainly have to include non-conservative fluid motion. For example, the maximum fluid velocity obtained from the test case of section 4.2.2 was $0.023\mu m/sec$, which is one third the terrestrial cell sedimentation rate of $0.06\mu m/sec$ considered to be significant in the bacterial metabolism[17].

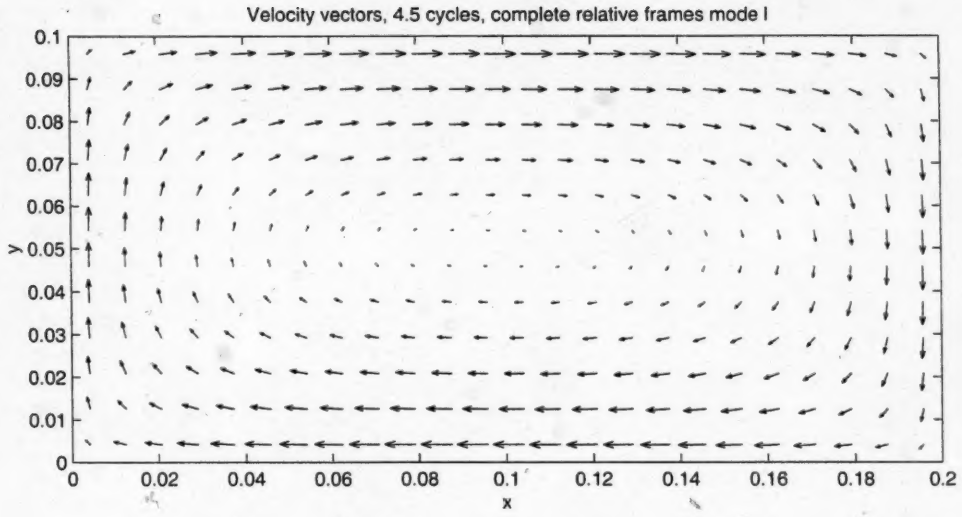

Figure 4.36: Velocity with relative frames model in a fluid of uniform density (max velocity is 0.023 $\mu m/s$)

The last important idea presented by the numerical results is the confirmation of the idea that the container shape is important in non-conservative motion. If a circular container is used, the motion predicted by the inviscid relative frames model is rigid body rotation. Deviating from the circular cavity produces non-rigid body motion of the fluid. This result may be important to researchers trying to eliminate sources of mixing. In other words, the influence on mixing of the non-conservative angular acceleratation term can be reduced by using a spherical container, in which case only the viscosity at the walls and the Coriolis accelerations would cause relative motion in the fluid.

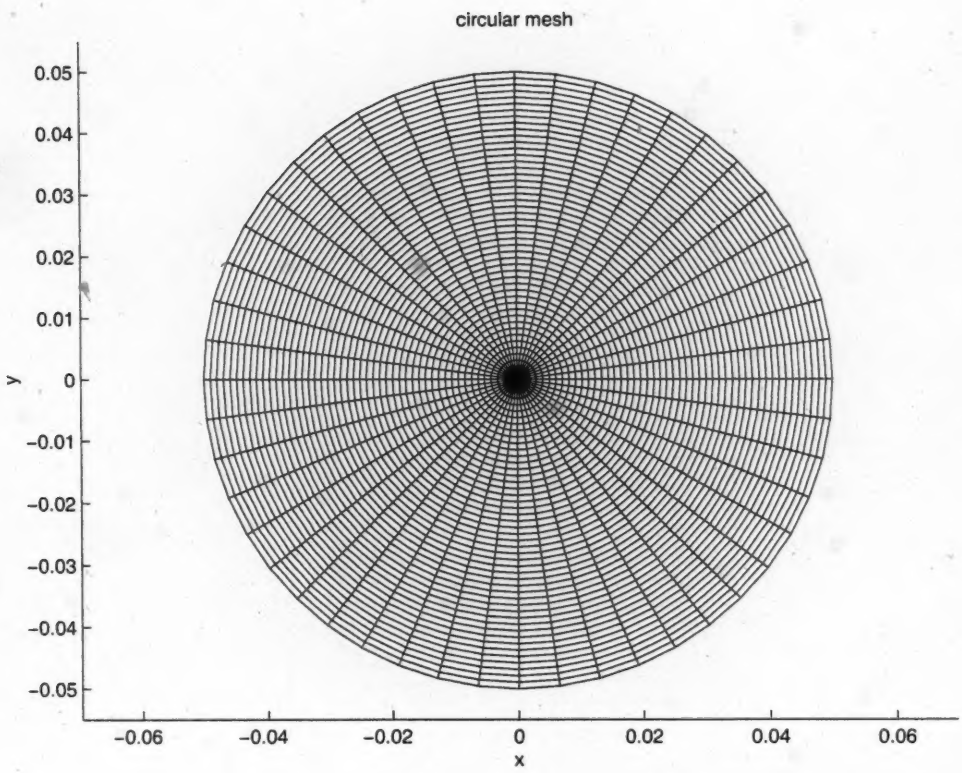

Figure 4.37: Circular grid

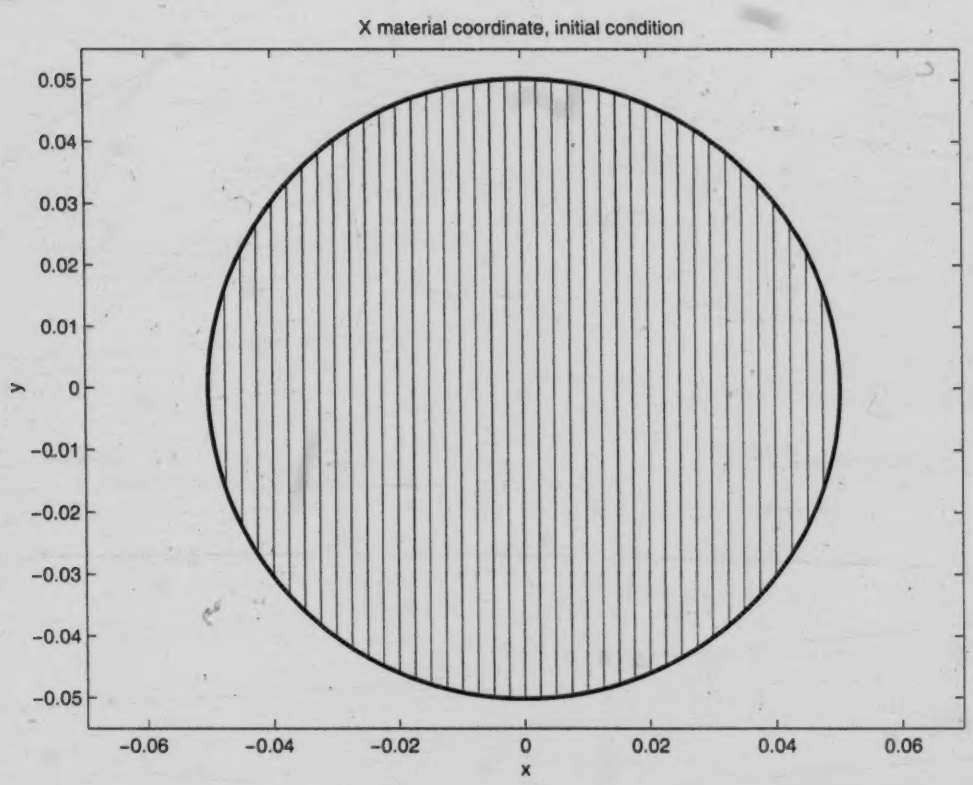

Figure 4.38: X material coordinates at initial condition

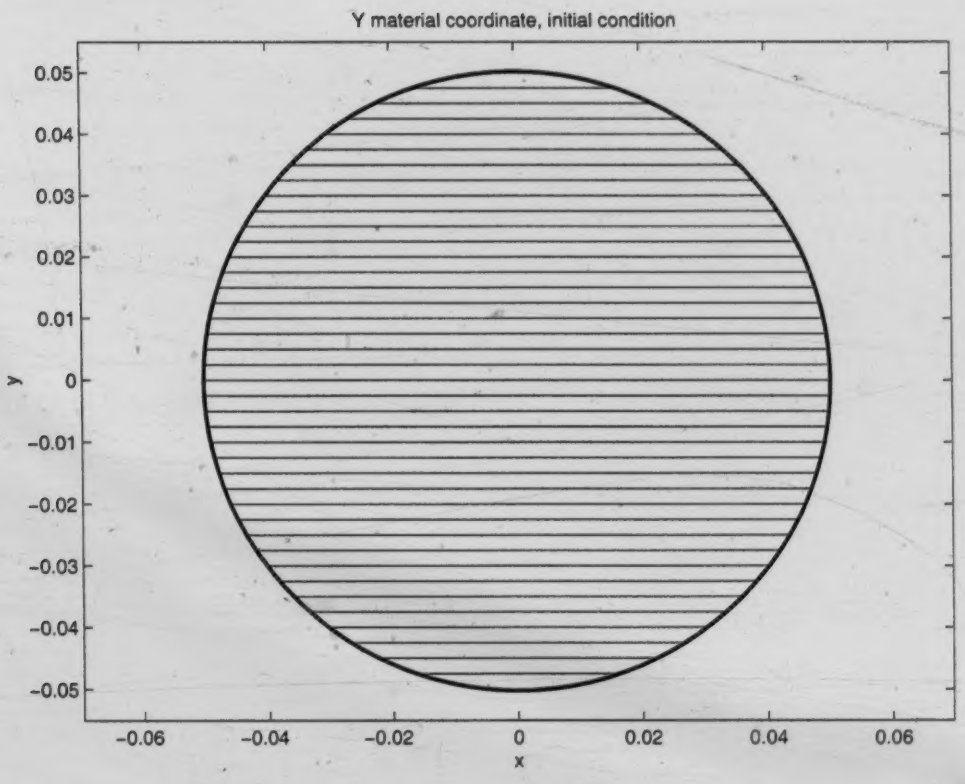

Figure 4.39: Y material coordinates at initial condition

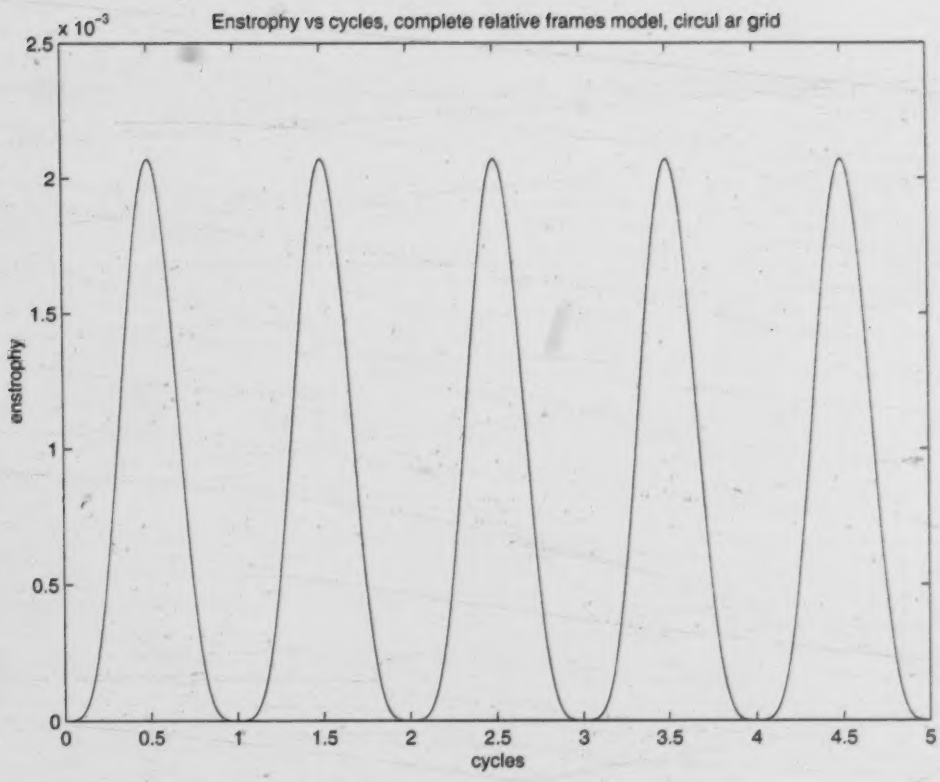

Figure 4.40: Enstrophy time history

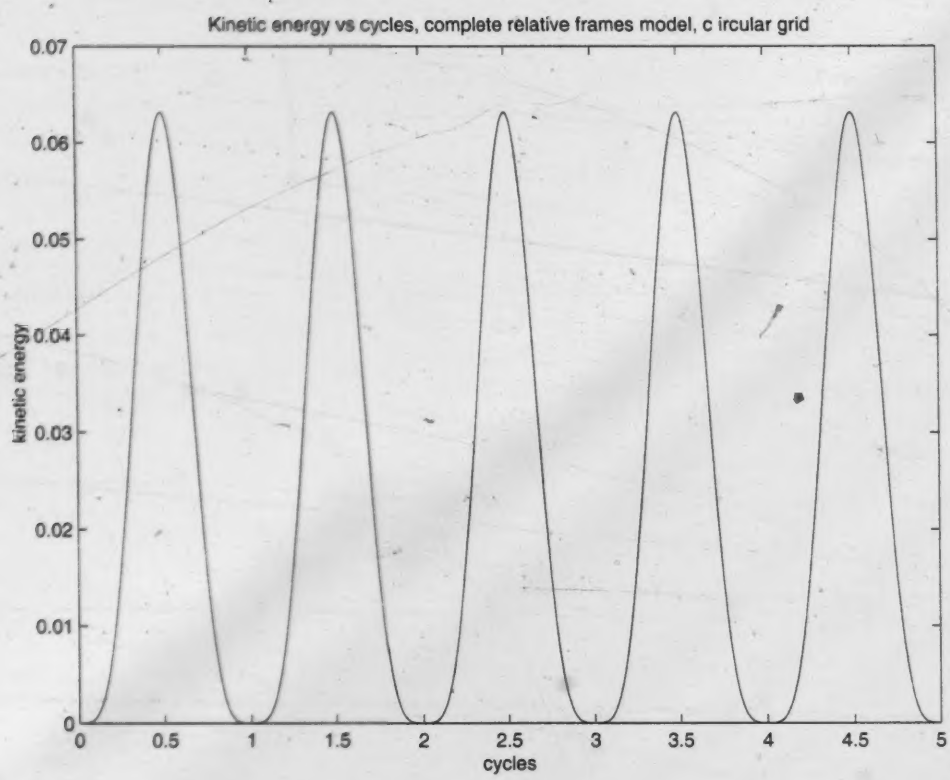

Figure 4.41: Kinetic energy time history

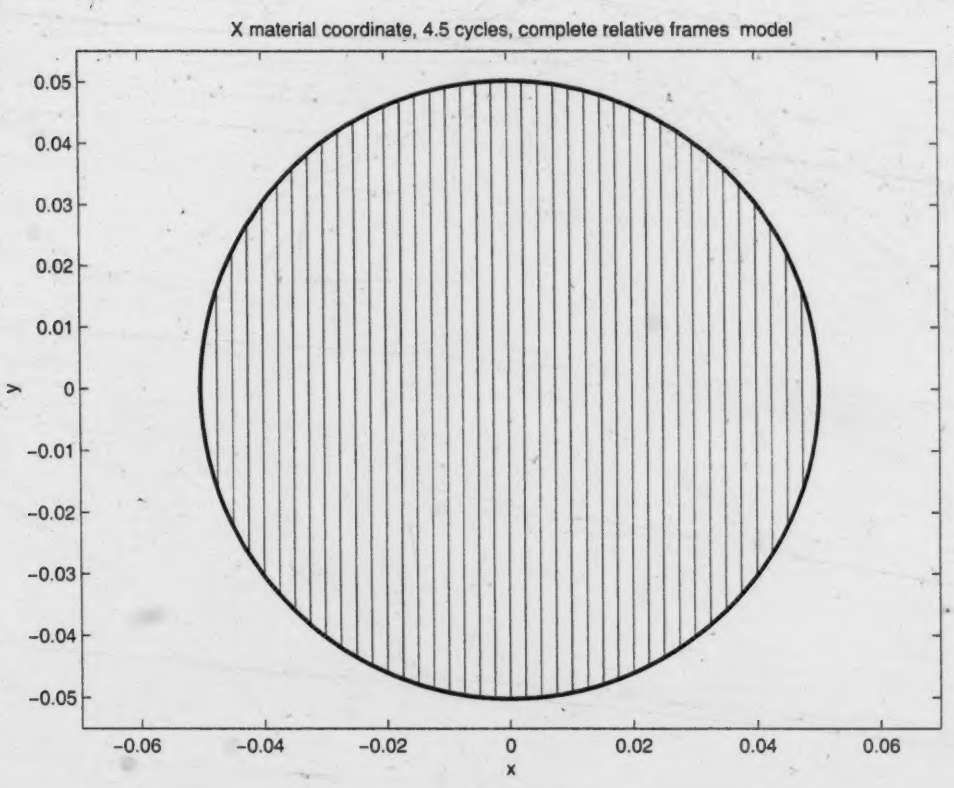

Figure 4.42: X material coordinates at 4 1/2 cycles

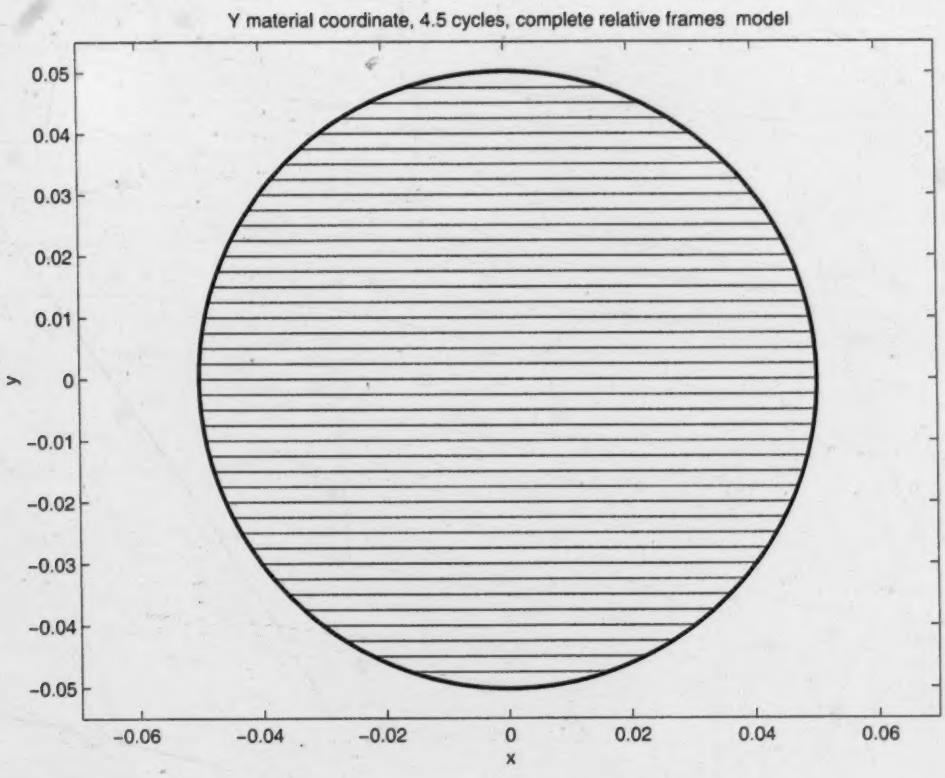

Figure 4.43: Y material coordinates at 4 1/2 cycles

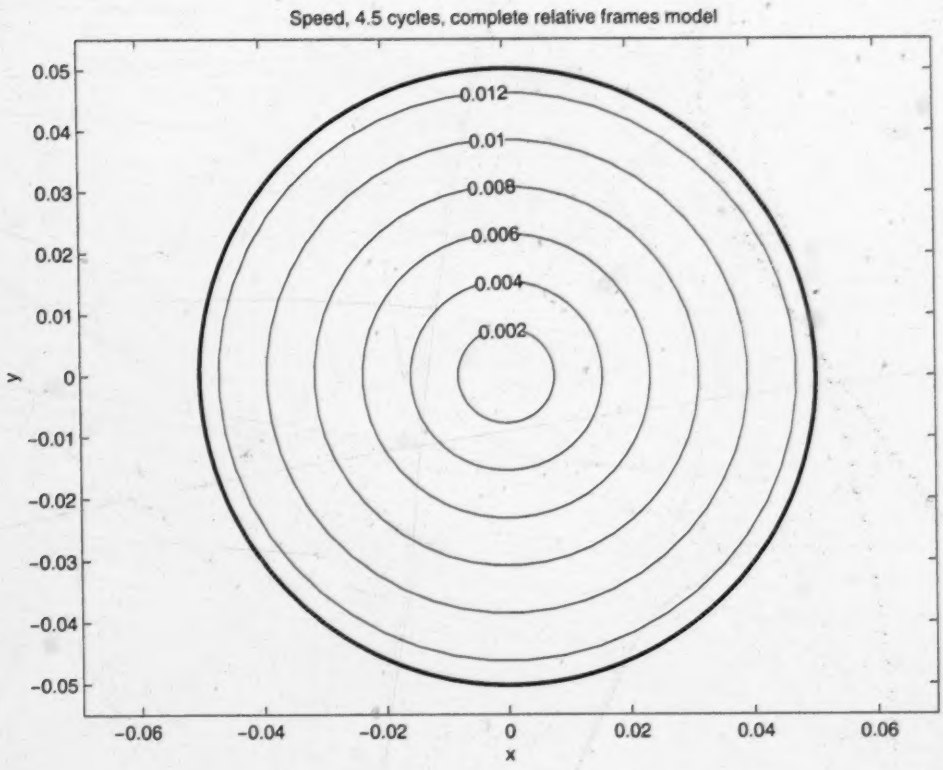

Figure 4.44: Fluid speed at 4 1/2 cycles

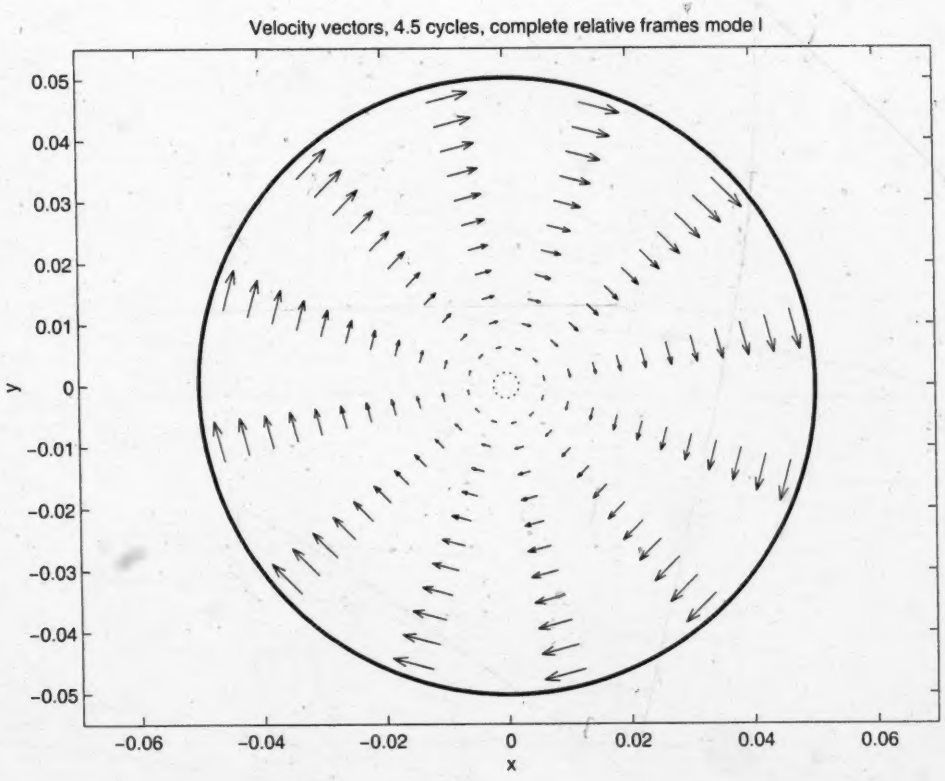

Figure 4.45: Velocity vectors at 4 1/2 cycles (maximum value is 0.0128 $\mu m/s$)

Chapter 5

Conclusions

An investigator in the microgravity fluid sciences proposed that current microgravity models are not capturing all characteristics of the flow. These models make use of time-varying body forces to simulate the accelerations experienced on board an orbiting platform. The existence of a deficiency in the microgravity models is reinforced by results obtained from orbiting bacterial growth cultures. Both suggest that a source of fluid flow is not being characterized.

To address this deficiency and better characterize the microgravity environment, the equations of motion for a fluid in microgravity were derived from 1^{st} principles using a relative frames analysis. Multiple moving frames were used to describe the motion of the fluid in an experimental platform orbiting the earth. The resulting analysis predicts non-conservative sources of motion as well as a number of conservative source terms. The non-conservative sources are a result of angular acceleration and Coriolis acceleration, the latter being conservative when only 2 dimensional flow is considered.

In order to evaluate the predictions of the relative frames analysis, a model of spacecraft motion was developed using standard microgravity models as a foundation. In particular, a standard model that uses a unidirectional body force varying sinusoidally with time was employed. Spacecraft translational accelerations were equated to these sinusoidal accelerations, but the pitch of the spacecraft was assumed to follow the path of the orbit. In this way, values for the rotational and translational source terms, derived from the relative frames analysis, can be obtained. The magnitudes of these values were found to fall in the expected range of actual microgravity levels experienced aboard orbiting spacecraft. The model of spacecraft motion combined with the relative frames analysis provides a complete system by which flows in microgravity can be characterized.

The relative frames analysis with the model of spacecraft motion were then evaluated numerically. Only the non-conservative sources were found to generate motion in flows of uniform density. The non-conservative sources are unique by this property, and as such they are believed to be the missing part to current microgravity models. Further, this result was shown to be significant in offering a possible mechanism for the increased bacterial growth found in space-based experiments.

When an experiment with a density interface was considered, the sources derived from the relative frames model were shown to cause the breakdown of the interface after only a few cycles. When the sinusoidally-varying source

term alone was applied for the same number of cycles, no such breakdown was evidenced. The relative frames analysis combined with the model of spacecraft motion thus shows that the extra source terms may be important even in a flow with a density gradient.

The non-conservative angular acceleration term,

$$\dot{q}_p \epsilon_{ipk} x_k$$

suggests that in the absence of cavity walls, rigid body motion of the fluid would result. The shape of the experimental cavity must then play a role in the resulting rotational motion. Numerical simulations of circular and rectangular cavities containing fluids of uniform density confirmed this expectation, where the circular cavity flow was in rigid body rotation.

The system of a relative frames analysis combined with the model of spacecraft motion offers a unique tool with which microgravity experiments can be designed. One of the most important driving forces for performing scientific investigations on orbiting platforms is to take advantage of the reduced gravity environment. If an experiment has the potential to be sensitive to the small accelerations of the platform, it is important to be able to design the setup in such a way as to minimize these sources of motion as much as possible. This is exactly the capability offered by this work. With the relative frames description, the location and orientation of the experiment on board the spacecraft can be optimized to reduce the effects of sources of motion. Values for these magnitudes are readily approximated with the model of spacecraft motion.

When considering designing parameters to eliminate non-conservative motion, the problem is a bit different. The non-conservative motion generated by angular acceleration was found to be independent of experiment location and orientation, but was found to be dependent on container shape. As such, different container shapes can be investigated with the relative frames and spacecraft motion models to minimize the effect of the non-conservative motion generated by angular acceleration.

Appendix A

Rotation Tensor Properties

The rotation tensor, A_{ij}, α_{ij}, or a_{ij}, describes the difference in angles between two coordinate frames, and is dependent on time only. The rotation tensor has the following property:

$$A_{ij}A_{kj} = \delta_{ik} \tag{A.1}$$

Taking the time derivative of equation (A.1) gives

$$\frac{dA_{ij}}{dt}A_{kj} + A_{ij}\frac{dA_{kj}}{dt} = 0 \tag{A.2}$$

Ω_{ik} is now defined as

$$\Omega_{ik} = A_{ij}\frac{dA_{kj}}{dt} \tag{A.3}$$

So by equation (A.2),

$$\Omega_{ij} = -\Omega_{ji} \tag{A.4}$$

and

$$\Omega_{kk} = 0 \tag{A.5}$$

This means that Ω_{ij} is skew-symmetric, and in particular, it has the form:

$$\Omega_{ij} = \begin{bmatrix} 0 & Q_3 & -Q_2 \\ -Q_3 & 0 & Q_1 \\ Q_2 & -Q_1 & 0 \end{bmatrix} \tag{A.6}$$

and in 2D it only has one non-zero component, $Q_3 = Q$:

$$\Omega_{ij} = \begin{bmatrix} 0 & Q \\ -Q & 0 \end{bmatrix} \tag{A.7}$$

By equation (A.6), it can be seen that:

$$\Omega_{jk} = \epsilon_{ijk} Q_i \tag{A.8}$$

In order to express the time derivatives of A_{ij} in terms of Ω_{ij}, multiply equation (A.3) by A_{im}, giving

$$\begin{aligned} A_{im}\Omega_{ik} &= A_{im}A_{ij}\frac{dA_{kj}}{dt} \\ &= \delta_{mj}\frac{dA_{kj}}{dt} \qquad \text{(by equation A.1)} \\ &= \frac{dA_{km}}{dt} \end{aligned} \tag{A.9}$$

To get the second derivative, take the time derivative of equation (A.9):

$$\frac{dA_{im}}{dt}\Omega_{ik} + A_{im}\frac{d\Omega_{ik}}{dt} = \frac{d^2A_{km}}{dt^2} \tag{A.10}$$

and use equation (A.9) in equation (A.10) to get

$$A_{pm}\Omega_{pi}\Omega_{ik} + A_{im}\frac{d\Omega_{ik}}{dt} = \frac{d^2A_{km}}{dt^2} \tag{A.11}$$

In two dimensions, the rotation tensor is:

$$\begin{aligned} A_{ji} \Rightarrow A_{11} &= \cos\theta \\ A_{12} &= \sin\theta \\ A_{21} &= -\sin\theta \\ A_{22} &= \cos\theta \end{aligned} \tag{A.12}$$

where θ is the rotation between the two coordinate frames considered.

Appendix B

Tensor to Vector Transformation

To show how to transform tensor terms into vector form, consider three tensors, A_i, B_i, and C_{ij}. The vector form of A_i and B_i are simply $\vec{A}$ and $\vec{B}$, and the matrix form of C_{ij} is represented with $\tilde{C}$.

In summation notation, a dot product is given as:

$$A_i B_i = A_1 B_1 + A_2 B_2 + A_3 B_3 = \vec{A} \cdot \vec{B} \tag{B.1}$$

and the cross product is:

$$\begin{aligned} \epsilon_{ijk} A_j B_k &= [A_2 B_3]_1 + [A_3 B_1]_2 + [A_1 B_2]_3 \\ &\quad -[A_3 B_2]_1 - [A_1 B_3]_2 - [A_2 B_1]_3 \\ &= \vec{A} \times \vec{B} \end{aligned} \tag{B.2}$$

The divergence of A_i in the X coordinate frame is:

$$\frac{\partial A_i}{\partial X_i} = \frac{\partial A_1}{\partial X_1} + \frac{\partial A_2}{\partial X_2} + \frac{\partial A_3}{\partial X_3} = \nabla \cdot \vec{A} \tag{B.3}$$

and the curl is simply the cross product of ∇ and A_i:

$$\epsilon_{ijk} \frac{\partial}{\partial X_j} A_k = \epsilon_{ijk} \nabla_j A_k = \nabla \times \vec{A} \tag{B.4}$$

Multiplication with a second order tensor is described:

$$\begin{aligned} C_{ij}A_i &= [C_{11}A_1 + C_{21}A_2]_1 + [C_{12}A_1 + C_{22}A_2]_2 \\ &= \tilde{C}\vec{A} \end{aligned} \tag{B.5}$$

where

$$\tilde{C} = \begin{bmatrix} C_{11} & C_{21} \\ C_{12} & C_{22} \end{bmatrix} \tag{B.6}$$

APPENDIX C

SIMPLIFICATION OF TERMS

The 2-dimensional momentum equation with rotation tensors can be simplified by breaking down each rotation tensor into its components. The initial equation is:

$$\begin{aligned}
&\frac{\partial \rho u_i}{\partial t} + \frac{\partial \rho u_i u_s}{\partial x_s} + \frac{\partial P}{\partial x_i} = \rho a_{ir}\alpha_{rt} g_t \\
&\quad -\rho a_{ir}\alpha_{rt}\Omega_{th}\Omega_{hj}(\alpha_{kj}(a_{nk}x_n + y'_k) + c_j) - \rho a_{ir}\Omega'_{rh}\Omega'_{hk}(a_{nk}x_n + y'_k) \\
&\qquad -2\rho a_{ir}\alpha_{rt}\alpha_{sj}\Omega_{tj}\Omega'_{sk}(a_{nk}x_n + y'_k) \\
&\quad -2\rho a_{ir}\alpha_{rt}\Omega_{tj}\left(\alpha_{kj}a_{nk}u_n + \frac{Dc_j}{Dt}\right) - 2\rho a_{ir}\Omega'_{rk}a_{nk}u_n \\
&\quad -\rho a_{ir}\alpha_{rt}\frac{D\Omega_{tj}}{Dt}(\alpha_{kj}(a_{nk}x_n + y'_k) + c_j) - \rho a_{ir}\frac{D\Omega'_{rk}}{Dt}(a_{nk}x_n + y'_k) \\
&\quad -\rho a_{ir}\alpha_{rt}\frac{D^2 c_t}{Dt^2}
\end{aligned} \tag{C.1}$$

Using the identity

$$\epsilon_{pqi}\epsilon_{ijk}K_q L_j M_k = K_k L_p M_k - K_j L_j M_p \tag{C.2}$$

the second term on the right hand side of equation (C.1) is reduced as follows:

$$-\rho a_{ir}\alpha_{rt}\Omega_{th}\Omega_{hj}(\alpha_{kj}(a_{nk}x_n + y'_k) + c_j)$$

$$
\begin{aligned}
&= -\rho a_{ir}\alpha_{rt}\epsilon_{pth}Q_p\epsilon_{vhj}Q_v(\alpha_{kj}a_{nk}x_n + \alpha_{kj}y'_k + c_j) \\
&= -\rho a_{ir}\alpha_{rt}\epsilon_{pth}\epsilon_{vhj}Q_pQ_v(\alpha_{kj}a_{nk}x_n + \alpha_{kj}y'_k + c_j) \\
&= -\rho a_{ir}\alpha_{rt}\epsilon_{tph}\epsilon_{hvj}Q_pQ_v(\alpha_{kj}a_{nk}x_n + \alpha_{kj}y'_k + c_j) \\
&= -\rho a_{ir}\alpha_{rt}[Q_jQ_t(\alpha_{kj}a_{nk}x_n + \alpha_{kj}y'_k + c_j) \\
&\qquad -Q_vQ_v(\alpha_{kt}a_{nk}x_n + \alpha_{kt}y'_k + c_t)]
\end{aligned}
\tag{C.3}
$$

and, using $Q_i = Q_1 + Q_2 + Q_3 = 0 + 0 + Q_3$, the term in square brackets becomes

$$
\begin{aligned}
t = 1 \;\Rightarrow\; & [Q_jQ_1(\alpha_{kj}a_{nk}x_n + \alpha_{kj}y'_k + c_j) \\
& \qquad -Q_vQ_v(\alpha_{k1}a_{nk}x_n + \alpha_{k1}y'_k + c_1)] \\
& = [0 - Q_3Q_3(\alpha_{k1}a_{nk}x_n + \alpha_{k1}y'_k + c_1)] \\
t = 2 \;\Rightarrow\; & [Q_jQ_2(\alpha_{kj}a_{nk}x_n + \alpha_{kj}y'_k + c_j) \\
& \qquad -Q_vQ_v(\alpha_{k2}a_{nk}x_n + \alpha_{k2}y'_k + c_2)] \\
& = [0 - Q_3Q_3(\alpha_{k2}a_{nk}x_n + \alpha_{k2}y'_k + c_2)] \\
t = 3 \;\Rightarrow\; & [Q_jQ_3(\alpha_{kj}a_{nk}x_n + \alpha_{kj}y'_k + c_j) \\
& \qquad -Q_vQ_v(\alpha_{k3}a_{nk}x_n + \alpha_{k3}y'_k + c_3)] \\
& = [0 - Q_3Q_3(\alpha_{k3}a_{nk}x_n + \alpha_{k3}y'_k + c_3)]
\end{aligned}
\tag{C.4}
$$

In two dimensions where $t = 1$ and 2 only and $\alpha_{k3} = 0$,

$$
\begin{aligned}
-Q_3Q_3[\alpha_{k1}a_{nk}x_n + \alpha_{k1}y'_k + c_1]_{t=1} - Q_3Q_3[\alpha_{k2}a_{nk}x_n + \alpha_{k2}y'_k + c_2]_{t=2} \\
= -Q_3^2(\alpha_{kt}a_{nk}x_n + \alpha_{kt}y'_k + c_t)
\end{aligned}
\tag{C.5}
$$

so equation (C.3) becomes:

$$\begin{aligned}
- \quad & \rho a_{ir}\alpha_{rt}[Q_jQ_t(\alpha_{kj}a_{nk}x_n + \alpha_{kj}y'_k + c_j) \\
& \qquad -Q_vQ_v(\alpha_{kt}a_{nk}x_n + \alpha_{kt}y'_k + c_t)] \\
= \quad & -\rho a_{ir}\alpha_{rt}[-Q_3^2(\alpha_{kt}a_{nk}x_n + \alpha_{kt}y'_k + c_t)] \\
= \quad & \rho a_{ir}\alpha_{rt}Q_3^2(\alpha_{kt}a_{nk}x_n + \alpha_{kt}y'_k + c_t) \\
= \quad & \rho Q_3^2(a_{ir}\alpha_{rt}\alpha_{kt}a_{nk}x_n + a_{ir}\alpha_{rt}\alpha_{kt}y'_k + a_{ir}\alpha_{rt}c_t) \\
= \quad & \rho Q_3^2(a_{ir}\delta_{rk}a_{nk}x_n + a_{ir}\delta_{rk}y'_k + a_{ir}\alpha_{rt}c_t) \\
= \quad & \rho Q_3^2(a_{ir}a_{nr}x_n + a_{ir}y'_r + a_{ir}\alpha_{rt}c_t) \\
= \quad & \rho Q_3^2(\delta_{in}x_n + a_{ir}y'_r + a_{ir}\alpha_{rt}c_t) \\
= \quad & \rho Q_3^2(x_i + a_{ir}y'_r + a_{ir}\alpha_{rt}c_t) \qquad \text{(C.6)}
\end{aligned}$$

Similarly, the third term on the right hand side of equation (C.1) simplifies:

$$\begin{aligned}
-\rho a_{ir}\Omega'_{rh}\Omega'_{hk}(a_{nk}x_n + y'_k) &= -\rho a_{ir}\epsilon_{prh}q_p\epsilon_{vhk}q_v(a_{nk}x_n + y'_k) \\
&= -\rho a_{ir}\epsilon_{rph}\epsilon_{hvk}q_pq_v(a_{nk}x_n + y'_k) \\
&= -\rho a_{ir}[q_kq_r(a_{nk}x_n + y'_k) \\
&\qquad -q_vq_v(a_{nr}x_n + y'_r)] \\
&= -\rho a_{ir}[-q_3^2(a_{nr}x_n + y'_r)] \\
&= \rho[q_3^2a_{ir}(a_{nr}x_n + y'_r)] \\
&= \rho q_3^2(\delta_{in}x_n + a_{ir}y'_r) \\
&= \rho q_3^2(x_i + a_{ir}y'_r)
\end{aligned}$$

The fourth term on the right of equation (C.1) makes use of the definition of the components of the rotation tensor from (2.41) as well as, once again,

$Q_i = Q_3$, giving:

$$
\begin{aligned}
&-2\rho a_{ir}\alpha_{rt}\alpha_{sj}\Omega_{tj}\Omega'_{sk}(a_{nk}x_n + y'_k) \\
&\quad = -2\rho a_{ir}\alpha_{rt}\alpha_{sj}\epsilon_{ptj}Q_p\epsilon_{vsk}q_v(a_{nk}x_n + y'_k) \\
&\quad = -2\rho a_{ir}\alpha_{rt}\alpha_{sj}\epsilon_{3tj}Q_3\epsilon_{3sk}q_3(a_{nk}x_n + y'_k) \\
&\quad = -2\rho a_{ir}[\alpha_{r1}\alpha_{12}\epsilon_{312}Q_3\epsilon_{312}q_3(a_{n2}x_n + y'_2) \\
&\qquad +\alpha_{r1}\alpha_{22}\epsilon_{312}Q_3\epsilon_{321}q_3(a_{n1}x_n + y'_1) \\
&\qquad +\alpha_{r2}\alpha_{11}\epsilon_{321}Q_3\epsilon_{312}q_3(a_{n2}x_n + y'_2) \\
&\qquad +\alpha_{r2}\alpha_{21}\epsilon_{321}Q_3\epsilon_{321}q_3(a_{n1}x_n + y'_1)] \\
&\quad = -2\rho a_{ir}Q_3q_3[\alpha_{r1}\alpha_{12}(a_{n2}x_n + y'_2) - \alpha_{r1}\alpha_{22}(a_{n1}x_n + y'_1) \\
&\qquad -\alpha_{r2}\alpha_{11}(a_{n2}x_n + y'_2) + \alpha_{r2}\alpha_{21}(a_{n1}x_n + y'_1)] \\
r = 1 \;\Rightarrow\; &-2\rho a_{i1}Q_3q_3[\alpha_{11}\alpha_{12}(a_{n2}x_n + y'_2) - \alpha_{11}\alpha_{22}(a_{n1}x_n + y'_1) \\
&\qquad -\alpha_{12}\alpha_{11}(a_{n2}x_n + y'_2) + \alpha_{12}\alpha_{21}(a_{n1}x_n + y'_1)] \\
&= -2\rho a_{i1}Q_3q_3[\cos\theta\sin\theta(a_{n2}x_n + y'_2) - \cos^2\theta(a_{n1}x_n + y'_1) \\
&\qquad -\sin\theta\cos\theta(a_{n2}x_n + y'_2) - \sin^2\theta(a_{n1}x_n + y'_1)] \\
&= -2\rho a_{i1}Q_3q_3[-(\cos^2\theta + \sin^2\theta)(a_{n1}x_n + y'_1)] \\
&= 2\rho a_{i1}Q_3q_3(a_{n1}x_n + y'_1) \\
r = 2 \;\Rightarrow\; &-2\rho a_{i2}Q_3q_3[\alpha_{21}\alpha_{12}(a_{n2}x_n + y'_2) - \alpha_{21}\alpha_{22}(a_{n1}x_n + y'_1) \\
&\qquad -\alpha_{22}\alpha_{11}(a_{n2}x_n + y'_2) + \alpha_{22}\alpha_{21}(a_{n1}x_n + y'_1)] \\
&= -2\rho a_{i2}Q_3q_3[-(\sin^2\theta + \cos^2\theta)(a_{n2}x_n + y'_2)] \\
&= 2\rho a_{i2}Q_3q_3(a_{n2}x_n + y'_2) \qquad \text{(C.7)}
\end{aligned}
$$

Since r=3 gives $a_{i3} = 0$, the result is:

$$\begin{aligned} -2\rho a_{ir}\alpha_{rt}\alpha_{sj}\Omega_{tj}\Omega'_{sk}(a_{nk}x_n + y'_k) &= 2\rho a_{ir}Q_3q_3(a_{nr}x_n + y'_r) \\ &= 2\rho Q_3q_3(a_{ir}a_{nr}x_n + a_{ir}y'_r) \\ &= 2\rho Q_3q_3(\delta_{in}x_n + a_{ir}y'_r) \\ &= 2\rho Q_3q_3(x_i + a_{ir}y'_r) \end{aligned} \tag{C.8}$$

Similarly, using the rotation tensor properties from (2.42), term five also simplifies, with the bracketed portions $\alpha_{kj}a_{nk}u_n$ and $\frac{Dc_1}{Dt}$ considered separately:

$$\begin{aligned} &-2\rho a_{ir}\alpha_{rt}\Omega_{tj}(\alpha_{kj}a_{nk}u_n) \\ &\quad= 2\rho a_{ir}\alpha_{rt}\epsilon_{ptj}Q_p(\alpha_{kj}a_{nk}u_n) \\ &\quad= 2\rho a_{ir}\alpha_{rt}\epsilon_{3tj}Q_3(\alpha_{kj}a_{nk}u_n) \\ &\quad= 2\rho a_{ir}\left[\alpha_{r1}\epsilon_{312}Q_3(\alpha_{k2}a_{nk}u_n) + \alpha_{r2}\epsilon_{321}Q_3(\alpha_{k1}a_{nk}u_n)\right] \\ &\quad= 2\rho a_{ir}Q_3\left[\alpha_{r1}(\alpha_{k2}a_{nk}u_n) - \alpha_{r2}(\alpha_{k1}a_{nk}u_n)\right] \\ &\quad= 2\rho a_{ir}Q_3\left\{\alpha_{r1}\alpha_{12}(a_{11}u_1 + a_{21}u_2) - \alpha_{r2}\alpha_{11}(a_{11}u_1 + a_{21}u_2)\right. \\ &\qquad\left.+\alpha_{r1}\alpha_{22}(a_{12}u_1 + a_{22}u_2) - \alpha_{r2}\,\alpha_{21}(a_{12}u_1 + a_{22}u_2)\right\} \\ &\quad= 2\rho a_{i1}Q_3\left\{\alpha_{11}\alpha_{12}(a_{11}u_1 + a_{21}u_2) - \alpha_{12}\alpha_{11}(a_{11}u_1 + a_{21}u_2)\right. \\ &\qquad\left.+ \alpha_{11}\alpha_{22}(a_{12}u_1 + a_{22}u_2) - \alpha_{12}\alpha_{21}(a_{12}u_1 + a_{22}u_2)\right\} \\ &\qquad 2\rho a_{i2}Q_3\left\{\alpha_{21}\alpha_{12}(a_{11}u_1 + a_{21}u_2) - \alpha_{22}\alpha_{11}(a_{11}u_1 + a_{21}u_2)\right. \\ &\qquad\left.+ \alpha_{21}\alpha_{22}(a_{12}u_1 + a_{22}u_2) - \alpha_{22}\alpha_{21}(a_{12}u_1 + a_{22}u_2)\right\} \\ &\quad= 2\rho a_{i1}Q_3\left\{\cos\theta\sin\theta(a_{11}u_1 + a_{21}u_2) - \sin\theta\cos\theta(a_{11}u_1 + a_{21}u_2)\right. \\ &\qquad\left.+ \cos^2\theta(a_{12}u_1 + a_{22}u_2) + \sin^2\theta(a_{12}u_1 + a_{22}u_2)\right\} \\ &\qquad 2\rho a_{i2}Q_3\left\{-\sin^2\theta(a_{11}u_1 + a_{21}u_2) - \cos^2\theta(a_{11}u_1 + a_{21}u_2)\right. \end{aligned}$$

$$
\begin{aligned}
& \quad - \sin\theta\cos\theta(a_{12}u_1 + a_{22}u_2) + \cos\theta\sin\theta(a_{12}u_1 + a_{22}u_2)\} \\
& = 2\rho Q_3[a_{i1}(a_{12}u_1 + a_{22}u_2) - a_{i2}(a_{11}u_1 + a_{21}u_2)] \\
i = 1 \;\Rightarrow\; & 2\rho Q_3[a_{11}(a_{12}u_1 + a_{22}u_2) - a_{12}(a_{11}u_1 + a_{21}u_2)] \\
& = 2\rho Q_3[\cos\Theta(\sin\Theta u_1 + \cos\Theta u_2) \\
& \qquad - \sin\Theta(\cos\Theta u_1 - \sin\Theta u_2)] \\
& = 2\rho Q_3 u_2 \\
i = 2 \;\Rightarrow\; & 2\rho Q_3[a_{21}(a_{12}u_1 + a_{22}u_2) - a_{22}(a_{11}u_1 + a_{21}u_2)] \\
& = 2\rho Q_3[-\sin\Theta(\sin\Theta u_1 + \cos\Theta u_2) \\
& \qquad - \cos\Theta(\cos\Theta u_1 - \sin\Theta u_2)] \\
& = -2\rho Q_3 u_1
\end{aligned}
$$

therefore

$$
2\rho a_{ir}\alpha_{rt}\epsilon_{ptj}Q_p(\alpha_{kj}a_{nk}u_n) \;=\; -2\rho\epsilon_{ijk}Q_j u_k \tag{C.9}
$$

where $Q_j = Q_3$ only.

Now consider the fifth term with $\frac{Dc_j}{Dt}$:

$$
\begin{aligned}
2\rho a_{ir}\alpha_{rt}\epsilon_{ptj}Q_p\left(\frac{Dc_j}{Dt}\right) &= 2\rho a_{ir}\alpha_{rt}\epsilon_{3tj}Q_3\left(\frac{Dc_j}{Dt}\right) \\
&= 2\rho a_{ir}\left[\alpha_{r1}\epsilon_{312}Q_3\left(\frac{Dc_2}{Dt}\right) + \alpha_{r2}\epsilon_{321}Q_3\left(\frac{Dc_1}{Dt}\right)\right] \\
&= 2\rho a_{ir}\left[\alpha_{r1}Q_3\left(\frac{Dc_2}{Dt}\right) - \alpha_{r2}Q_3\left(\frac{Dc_1}{Dt}\right)\right]
\end{aligned}
$$

So this part of the term is already in its simplest form. The fifth term on the right hand side of equation (C.1) can be expressed as follows:

$$
-2\rho a_{ir}\alpha_{rt}\Omega_{tj}(\alpha_{kj}a_{nk}u_n + \frac{Dc_j}{Dt}) \;=\; -2\rho\epsilon_{ijk}Q_j u_k - 2\rho a_{ir}\alpha_{rt}\epsilon_{tpj}Q_p\frac{Dc_j}{Dt}
$$

$$= -2\rho Q_p[\epsilon_{ipk}u_k + a_{ir}\alpha_{rt}\epsilon_{tpj}\frac{Dc_j}{Dt}] \tag{C.10}$$

Now the sixth term on the right hand side of equation (C.1) is considered:

$$\begin{aligned}
-2\rho a_{ir}\Omega'_{rk}a_{nk}u_n &= 2\rho a_{ir}\epsilon_{prk}q_p a_{nk}u_n \\
&= 2\rho a_{ir}\epsilon_{3rk}q_3(a_{1k}u_1 + a_{2k}u_2) \\
&= 2\rho[a_{i1}\epsilon_{312}q_3(a_{12}u_1 + a_{22}u_2) \\
&\qquad + a_{i2}\epsilon_{321}q_3(a_{11}u_1 + a_{21}u_2)] \\
&= 2\rho[a_{i1}q_3(a_{12}u_1 + a_{22}u_2) - a_{i2}q_3(a_{11}u_1 + a_{21}u_2)] \\
i = 1 \;\Rightarrow\; & 2\rho[a_{11}q_3(a_{12}u_1 + a_{22}u_2) - a_{12}q_3(a_{11}u_1 + a_{21}u_2)] \\
& = 2\rho q_3[\cos\Theta(\sin\Theta u_1 + \cos\Theta u_2) \\
& \qquad - \sin\Theta(\cos\Theta u_1 - \sin\Theta u_2)] \\
& = 2\rho q_3 u_2 \\
i = 2 \;\Rightarrow\; & 2\rho[a_{21}q_3(a_{12}u_1 + a_{22}u_2) - a_{22}q_3(a_{11}u_1 + a_{21}u_2)] \\
& = 2\rho q_3[-\sin\Theta(\sin\Theta u_1 + \cos\Theta u_2) \\
& \qquad - \cos\Theta(\cos\Theta u_1 - \sin\Theta u_2)] \\
& = -2\rho q_3 u_1
\end{aligned}$$

therefore

$$-2\rho a_{ir}\Omega'_{rk}a_{nk}u_n = -2\rho\epsilon_{ijk}q_j u_k \tag{C.11}$$

Now the seventh term is considered, and here again with each bracketed part considered separately. First is

$$-\rho a_{ir}\alpha_{rt}\frac{D\Omega_{tj}}{Dt}(\alpha_{kj}a_{nk}x_n)$$

$$
\begin{aligned}
&= \rho a_{ir}\alpha_{rt}\frac{D\epsilon_{ptj}Q_p}{Dt}(\alpha_{kj}a_{nk}x_n) \\
&= \rho a_{ir}\alpha_{rt}\epsilon_{3tj}\frac{DQ_3}{Dt}(\alpha_{1j}a_{11}x_1 + \alpha_{1j}a_{21}x_2 \\
&\quad +\alpha_{2j}a_{12}x_1 + \alpha_{2j}a_{22}x_2) \\
&= \rho a_{ir}\frac{DQ_3}{Dt}[\alpha_{r1}\epsilon_{312}(\alpha_{12}a_{11}x_1 + \alpha_{12}a_{21}x_2 \\
&\quad +\alpha_{22}a_{12}x_1 + \alpha_{22}a_{22}x_2) \\
&\quad +\alpha_{r2}\epsilon_{321}(\alpha_{11}a_{11}x_1 + \alpha_{11}a_{21}x_2 \\
&\quad +\alpha_{21}a_{12}x_1 + \alpha_{21}a_{22}x_2)] \\
&= \rho a_{i1}\frac{DQ_3}{Dt}[\alpha_{11}(\alpha_{12}a_{11}x_1 + \alpha_{12}a_{21}x_2 \\
&\quad +\alpha_{22}a_{12}x_1 + \alpha_{22}a_{22}x_2) \\
&\quad -\alpha_{12}(\alpha_{11}a_{11}x_1 + \alpha_{11}a_{21}x_2 \\
&\quad +\alpha_{21}a_{12}x_1 + \alpha_{21}a_{22}x_2)] \\
&\quad +\rho a_{i2}\frac{DQ_3}{Dt}[\alpha_{21}(\alpha_{12}a_{11}x_1 + \alpha_{12}a_{21}x_2 \\
&\quad +\alpha_{22}a_{12}x_1 + \alpha_{22}a_{22}x_2) \\
&\quad -\alpha_{22}(\alpha_{11}a_{11}x_1 + \alpha_{11}a_{21}x_2 \\
&\quad +\alpha_{21}a_{12}x_1 + \alpha_{21}a_{22}x_2)] \\
&= \rho a_{i1}\frac{DQ_3}{Dt}[\alpha_{11}\alpha_{12}a_{11}x_1 + \alpha_{11}\alpha_{12}a_{21}x_2 \\
&\quad +\alpha_{11}\alpha_{22}a_{12}x_1 + \alpha_{11}\alpha_{22}a_{22}x_2 \\
&\quad -\alpha_{12}\alpha_{11}a_{11}x_1 - \alpha_{12}\alpha_{11}a_{21}x_2 \\
&\quad -\alpha_{12}\alpha_{21}a_{12}x_1 - \alpha_{12}\alpha_{21}a_{22}x_2] \\
&\quad +\rho a_{i2}\frac{DQ_3}{Dt}[\alpha_{21}\alpha_{12}a_{11}x_1 + \alpha_{21}\alpha_{12}a_{21}x_2 \\
&\quad +\alpha_{21}\alpha_{22}a_{12}x_1 + \alpha_{21}\alpha_{22}a_{22}x_2 \\
&\quad -\alpha_{22}\alpha_{11}a_{11}x_1 - \alpha_{22}\alpha_{11}a_{21}x_2
\end{aligned}
$$

$$
\begin{aligned}
& -\alpha_{22}\alpha_{21}a_{12}x_1 - \alpha_{22}\alpha_{21}a_{22}x_2] \\
= \;& \rho a_{i1}\frac{DQ_3}{Dt}[\cos^2\theta a_{12}x_1 + \cos^2\theta a_{22}x_2 \\
& + \sin^2\theta a_{12}x_1 + \sin^2\theta a_{22}x_2] \\
& + \rho a_{i2}\frac{DQ_3}{Dt}[-\sin^2\theta a_{11}x_1 - \sin^2\theta a_{21}x_2 \\
& - \cos^2\theta a_{11}x_1 - \cos^2\theta a_{21}x_2] \\
= \;& \rho a_{i1}\frac{DQ_3}{Dt}(a_{12}x_1 + a_{22}x_2) + \rho a_{i2}\frac{DQ_3}{Dt}(-a_{11}x_1 - a_{21}x_2) \\
i = 1 \;\Rightarrow\; & \rho a_{11}\frac{DQ_3}{Dt}(a_{12}x_1 + a_{22}x_2) + \rho a_{12}\frac{DQ_3}{Dt}(-a_{11}x_1 - a_{21}x_2) \\
& = \rho\frac{DQ_3}{Dt}(a_{11}a_{12}x_1 + a_{11}a_{22}x_2 - a_{12}a_{11}x_1 - a_{12}a_{21}x_2) \\
& = \rho\frac{DQ_3}{Dt}x_2 \\
i = 2 \;\Rightarrow\; & \rho a_{21}\frac{DQ_3}{Dt}(a_{12}x_1 + a_{22}x_2) + \rho a_{22}\frac{DQ_3}{Dt}(-a_{11}x_1 - a_{21}x_2) \\
& = \rho\frac{DQ_3}{Dt}(a_{21}a_{12}x_1 + a_{21}a_{22}x_2 - a_{22}a_{11}x_1 - a_{22}a_{21}x_2) \\
& = -\rho\frac{DQ_3}{Dt}x_1 \qquad \text{(C.12)}
\end{aligned}
$$

so

$$
-\rho a_{ir}\alpha_{rt}\frac{D\Omega_{tj}}{Dt}(\alpha_{kj}a_{nk}x_n) = -\rho\epsilon_{ijk}\frac{DQ_j}{Dt}x_k \qquad \text{(C.13)}
$$

Now look at the second part in brackets of the seventh term:

$$
\begin{aligned}
& -\rho a_{ir}\alpha_{rt}\frac{D\Omega_{tj}}{Dt}(\alpha_{kj}y'_k) \\
= \;& \rho a_{ir}\alpha_{rt}\frac{D\epsilon_{ptj}Q_p}{Dt}(\alpha_{1j}y'_1 + \alpha_{2j}y'_2) \qquad \text{(C.14)} \\
= \;& \rho a_{ir}\alpha_{rt}\epsilon_{3tj}\frac{DQ_3}{Dt}(\alpha_{1j}y'_1 + \alpha_{2j}y'_2) \\
= \;& \rho a_{ir}\frac{DQ_3}{Dt}[\alpha_{r1}\epsilon_{312}(\alpha_{12}y'_1 + \alpha_{22}y'_2) + \alpha_{r2}\epsilon_{321}(\alpha_{11}y'_1 + \alpha_{21}y'_2)] \\
= \;& \rho a_{ir}\frac{DQ_3}{Dt}[\alpha_{r1}\alpha_{12}y'_1 + \alpha_{r1}\alpha_{22}y'_2 - \alpha_{r2}\alpha_{11}y'_1 - \alpha_{r2}\alpha_{21}y'_2]
\end{aligned}
$$

$$
\begin{aligned}
&= \rho a_{i1}\frac{DQ_3}{Dt}[\alpha_{11}\alpha_{12}y_1' + \alpha_{11}\alpha_{22}y_2' - \alpha_{12}\alpha_{11}y_1' - \alpha_{12}\alpha_{21}y_2'] \\
&\quad \rho a_{i2}\frac{DQ_3}{Dt}[\alpha_{21}\alpha_{12}y_1' + \alpha_{21}\alpha_{22}y_2' - \alpha_{22}\alpha_{11}y_1' - \alpha_{22}\alpha_{21}y_2'] \\
&= \rho\frac{DQ_3}{Dt}[a_{i1}(\alpha_{11}\alpha_{22}y_2' - \alpha_{12}\alpha_{21}y_2') + a_{i2}(\alpha_{21}\alpha_{12}y_1' - \alpha_{22}\alpha_{11}y_1')] \\
&= \rho\frac{DQ_3}{Dt}[a_{i1}(\cos^2\theta y_2' + \sin^2\theta y_2') + a_{i2}(-\sin^2\theta y_1' - \cos^2\theta y_1')] \\
&= \rho\frac{DQ_3}{Dt}[a_{i1}y_2' - a_{i2}y_1'] \\
&= \rho\frac{DQ_p}{Dt}\epsilon_{pjk}a_{ij}y_k' \qquad \text{(C.15)}
\end{aligned}
$$

The third bracketed part of term seven does not reduce, so the whole term can be re-written as follows:

$$
\begin{aligned}
&-\rho a_{ir}\alpha_{rt}\frac{D\Omega_{tj}}{Dt}(\alpha_{kj}(a_{nk}x_n + y_k') + c_j) \\
&= \rho\epsilon_{pik}\frac{DQ_p}{Dt}x_k + \rho\frac{DQ_p}{Dt}\epsilon_{pjk}a_{ij}y_k' + \rho a_{ir}\alpha_{rt}\epsilon_{ptj}\frac{DQ_p}{Dt}c_j \\
&= \rho\frac{DQ_p}{Dt}[\epsilon_{pik}x_k + \epsilon_{pjk}a_{ij}y_k' + a_{ir}\alpha_{rt}\epsilon_{ptj}c_j] \qquad \text{(C.16)}
\end{aligned}
$$

The eighth term in equation (C.1) is the last term that may be simplified, and is also considered in separate parts. First considered is:

$$
\begin{aligned}
-\rho a_{ir}\frac{D\Omega_{rk}'}{Dt}(a_{nk}x_n) &= \rho a_{ir}\epsilon_{prk}\frac{Dq_p}{Dt}(a_{nk}x_n) \\
&= \rho a_{ir}\epsilon_{3rk}\frac{Dq_3}{Dt}(a_{1k}x_1 + a_{2k}x_2) \\
&= \rho\frac{Dq_3}{Dt}[a_{i1}\epsilon_{312}(a_{12}x_1 + a_{22}x_2) \\
&\quad + a_{i2}\epsilon_{321}(a_{11}x_1 + a_{21}x_2)] \\
&= \rho\frac{Dq_3}{Dt}[a_{i1}(a_{12}x_1 + a_{22}x_2) - a_{i2}(a_{11}x_1 + a_{21}x_2)]
\end{aligned}
$$

$$
i = 1 \;\Rightarrow\; \rho\frac{Dq_3}{Dt}[a_{11}(a_{12}x_1 + a_{22}x_2) - a_{12}(a_{11}x_1 + a_{21}x_2)]
$$

$$
\begin{aligned}
&= \rho\frac{Dq_3}{Dt}\left[\cos\Theta(\sin\Theta x_1 + \cos\Theta x_2) - \sin\Theta(\cos\Theta x_1 - \sin\Theta x_2)\right] \\
&= \rho\frac{Dq_3}{Dt}x_2 \\
i=2 \;\Rightarrow\; &\rho\frac{Dq_3}{Dt}\left[a_{21}(a_{12}x_1 + a_{22}x_2) - a_{22}(a_{11}x_1 + a_{21}x_2)\right] \\
&= \rho\frac{Dq_3}{Dt}\left[-\sin\Theta(\sin\Theta x_1 + \cos\Theta x_2)\right. \\
&\qquad \left. - \cos\Theta(\cos\Theta x_1 - \sin\Theta x_2)\right] \\
&= -\rho\frac{Dq_3}{Dt}x_1
\end{aligned}
$$

Now considering the y'_k part:

$$
\begin{aligned}
-\rho a_{ir}\frac{D\Omega'_{rk}}{Dt}(y'_k) &= \rho a_{ir}\epsilon_{prk}\frac{Dq_p}{Dt}(y'_k) \\
&= \rho a_{ir}\epsilon_{3rk}\frac{Dq_3}{Dt}y'_k \\
&= \rho\left[a_{i1}\epsilon_{312}\frac{Dq_3}{Dt}y'_2 + a_{i2}\epsilon_{321}\frac{Dq_3}{Dt}y'_1\right] \\
&= \rho\left[a_{i1}\frac{Dq_3}{Dt}y'_2 - a_{i2}\frac{Dq_3}{Dt}y'_1\right] \qquad \text{(C.17)}
\end{aligned}
$$

This shows that the y'_k portion of the term was already in its simplest form. The eighth term is therefore written as:

$$
\begin{aligned}
-\rho a_{ir}\frac{D\Omega'_{rk}}{Dt}(a_{nk}x_n + y'_k) &= \rho a_{ir}\epsilon_{prk}\frac{Dq_p}{Dt}(a_{nk}x_n + y'_k) \\
&= -\rho\epsilon_{ijk}\frac{Dq_j}{Dt}x_k - \rho a_{ir}\epsilon_{rpk}\frac{Dq_p}{Dt}y'_k \\
&= -\rho\frac{Dq_p}{Dt}[\epsilon_{ipk}x_k + a_{ir}\epsilon_{rpk}y'_k] \qquad \text{(C.18)}
\end{aligned}
$$

So the final form of equation (C.1) is:

$$\begin{aligned}
&\frac{\partial \rho u_i}{\partial t} + \frac{\partial \rho u_i u_s}{\partial x_s} + \frac{\partial P}{\partial x_i} = \rho a_{ir}\alpha_{rt} g_t \\
&\quad + \rho Q_3^2 (x_i + a_{ir}y'_r + a_{ir}\alpha_{rt}c_t) + \rho q_3^2 (x_i + a_{ir}y'_r) + 2\rho Q_3 q_3 (x_i + a_{ir}y'_r) \\
&\quad - 2\rho Q_p [\epsilon_{ipk} u_k + a_{ir}\alpha_{rt}\epsilon_{tpj}\frac{Dc_j}{Dt}] - 2\rho \epsilon_{ijk} q_j u_k \\
&\quad - \rho \frac{DQ_p}{Dt}[\epsilon_{ipk} x_k + \epsilon_{jpk} a_{ij} y'_k + a_{ir}\alpha_{rt}\epsilon_{tpj} c_j] - \rho \frac{Dq_p}{Dt}[\epsilon_{ipk} x_k + a_{ir}\epsilon_{rpk} y'_k] \\
&\quad - \rho a_{ir}\alpha_{rt}\frac{D^2 c_t}{Dt^2}
\end{aligned} \tag{C.19}$$

BIBLIOGRAPHY.

[1] J. Iwan D. Alexander and Charles A. Lundquist, "Residual Motions Caused by Micro-Gravitational Accelerations," The Journal of Astronautical Sciences, Vol. 35, No. 2, April-June 1987, pp. 193-211.

[2] Aris, Rutherford "Vectors, Tensors, and the Basic Equations of Fluid Mechanics," Dover, New York, 1962.

[3] Pan, Bo, D-Y Shang, B.Q. Li, and H.C de Groh, "Magnetic field effects on g-jitter induced flow and solute transport," International Journal of Heat and Mass Transfer, Vol. 45, 2002, pp. 125-144.

[4] Del Basso, Stephen D., "Microgravity Research in a Space Station Environment," Space 94 Proceedings – Engineering, Construction, and Operations in Space IV, ASCE, New York, 1994.

[5] Drolet F. and J. Vinals, "Fluid Flow Induced by a Random Accelerating Field," Microgravity Science and Technology, Vol. 11, No. 2, 1998, pp. 64-68

[6] Duval, W.M.B., and David A. Jacqmin, "Interfacial Dynamics of Two Liquids Under an Oscillating Gravitational Field," AIAA Journal, Vol. 28, No. 11, November 1990, pp.1933-1941.

[7] Fichtl George H. and Robert L. Holland "Simplified Model of Statistically Stationary Spacecraft Rotation and Associated Induced Gravity Environments," NASA TM-78164, 1978.

[8] Fujii, Terushige, Junichi Ohta, Takeshi Nakazawa, and Osamu Morimoto, "The Behavior of an Immiscible Equal-Density Liquid-Liquid Two-Phase Flow in a Horizontal Tube," JSME, Series B, Vol. 37, No. 1, 1994.

[9] Hampton, David R., Mark S. Whorton, "Frequency-Weighting Filter Selection for H_2 Control of Microgravity Isolation Systems: A Consideration of the 'Implicit Frequency Weighting' Problem," IEEE Transactions on Instrumentation and Measurement, Vol. 49, No. 2, April 2000, pp. 265-269.

[10] Harten Ami, and Stanley Osher, "Uniformly High-Order Accurate Nonoscillatory Schemes," SIAM Journal on Numerical Analysis, Vol. 24, Issue 2, April 1987, pp. 279-309.

[11] Hrovat, Kenneth, and Richard DeLombard, "Review of Shuttle Microgravity Acceleration Data (Vibratory and Transient)," 17th International Microgravity Measurements Group Meeting, Ohio, March 24-26, 1998.

[12] Hung, R.L., C.C. Lee, and F.W. Leslie, "Effect of the baffle on the asymmetric gravity jitter excited slosh wave and spacecraft moment and angular momentum fluctuations," Journal of Aerospace Engineering, Vol. 207, 1993, pp. 105-120.

[13] Hung, R.L., and H.L. Pan "Sloshing-Modulated Liquid-Vapor Interface Fluctuations Activated by Orbital Accelerations Associated with Spinning and/or Slew Motions," Journal of Colloid and Interface Science, Vol. 170, 1995, pp. 538-549.

[14] Kacena, M.A., G.A. Merrell, B. Manfredi, E.E. Smith, D.M. Klaus, and P. Todd, "Bacterial growth in space flight: logistic growth curve parameters for Escherichia coli and Bacillus subtilis.

[15] Kamotani, Y., A. Prasad, S. Ostrach, "Thermal Convection in an Enclosure Due to Vibrations Aboard Spacecraft," AIAA Journal Vol. 19, No. 4, April 1981, pp. 511-516.

[16] Kassemi, Siavash A., Simon Ostrach, "Nature of Buoyancy-Driven Flows in a Reduced-Gravity Environment," AIAA Journal, Vol. 30, No. 7, July 1992.

[17] Klaus, David, Steven Simske, Paul Todd, and Louis Stodieck, "Investigation of space flight effects on Escherichia coli and a proposed model of underlying physical mechanisms," Microbiology, No. 143, 1997, pp. 449-455.

[18] Knabe, Walter and Dirk Eilers, "Low-Gravity Environment in Spacelab," Acta Astronautica, Vol. 9, No. 4, 1982, pp. 187-198.

[19] Kondos P.A. and R.S. Subramanian, "Buoyant Flow in a Two-dimensional Cavity Due to a Sinusoidal Gravitational Field," Microgravity Science and Technology, Vol. 9, No. 6, 1996, pp. 143-151

[20] Le Cunff, Cedric, Abdelfattah Zebib, "Thermocapillary-Coriolis instabilities in liquid bridges," Physics of Fluids, Vol. 11, No. 9, September 1999.

[21] Malvern, Lawrence E., "Introduction to the Mechanics of a Continuous Medium," Prentice-Hall, New Jersey, 1969.

[22] Meyer, Richard E. "Introduction to Mathematical Fluid Dynamics," Dover, New York, 1971.

[23] Naumann, Robert J. "An analytical model for transport from quasi-steady and periodic accelerations on spacecraft," International Journal of Heat and Mass Transfer, Vol. 43, 2000, pp. 2917-2930.

[24] Ramachandran, N., Ch.R. Baugher, and R.J. Naumann, "Modeling Flows and Transport in Protein Crystal Growth," Microgravity Science and Technology, Vol. 8, No. 3, 1995.

[25] Reid, Kevin, "A computational Model of Vortex Breakdown in Density Stratified Flows,"M.Sc. Thesis, University of Alberta, 2000, Edmonton, Alberta, Canada.

[26] Savino, R., and R. Monti, "Improving diffusion-controlled microgravity experiments by facility orientation," Proc Instn Mech Engrs, Vol. 212, Part G, 1998, pp. 415-426.

[27] Schneider, Stefan and Johannes Straub, "Influence of the Prandtl Number on Laminar Natural Convection in a Cylinder Caused by g-Jitter," Journal of Crystal Growth, No. 97, 1989, pp. 235-242.

[28] Serrin, James, "Mathematical Principles of Classical Fluid Mechanics," Encyclopedia of Physics, ed. Flugge S., Vol. 8, No. 1, Springer-Verlag, Berlin, 1959, pp. 125-263

[29] Serway, Raymond, "Physics for Scientists and Engineers," 3rd Edition, Saunders College Publishing, Toronto, 1990.

[30] Thevenet, Danielle, Richard D'Ari, and Philippe Bouloc, "The SIGNAL experiment in BIORACK: Escherichia coli in microgravity," Journal of Biotechnology, Vol. 47, 1996, pp 89-97

[31] Thomson, J. Ross, Jaume Casademunt, Jorge Vinals, "Cavity flow induced by a fluctuating accleration field," Physics of Fluids, Vol. 7, No. 2, February 1995.

[32] Tryggvason B.V., private correspondence, March 29, 2001.

[33] Tryggvason B.V., R.F. Redden, R.A. Herring, W.M.B. Duval, R.W. Smith, K.S. Rezkallah, S. Varma, "The vibration environment on the International Space Station: Its significance to fluid-based experiments," ACTA ASTRONAUTICA Vol. 48 No.(2-3) Jan-Feb 2001, pp. 59-70.

[34] Wetzel, J., "Space Station Microgravity Analysis and Assessment," Space 94 Proceedings - Engineering, Construction, and Operations in Space IV, ASCE, New York, 1994.

[35] Wrede, Robert, "Introduction to Vector and Tensor Analysis," John Wiley & Sons, New York, 1963.

[36] Matsumoto, Satoshi and Shinichi Yoda, "Numerical study of diffusion coefficient measurements with sinusoidal varying accelerations," Journal of Applied Physics, Vol. 85, No. 12, June 1999, pp. 8131-8136.

[37] Yokota, J.W., "Vorticity Dynamics of Inviscid Shear Layers," AIAA Journal, Vol. 31, No. 8, August 1993, pp. 1430-1439.

[38] Yuferev V.S., Yu. A. Polovko, and V.V. Sazonov, "Three-dimensional thermal convection caused by spacecraft rotation in a rectangular enclosure with rigid walls," Physics of Fluids, Vol. 10, No. 10, October 1998, pp.2517-2524.

[39] Zebib, Abdelfattah, "Thermocapillary instabilities with system rotation," Physics of Fluids, Vol. 8, No. 12, December 1996.